ANALYSES OF HYDRODYNAMIC FORCES ON CENTRIFUGAL PUMP IMPELLERS

Thesis by

Douglas Ray Adkins

In Partial Fulfillment

of the Requirements for the Degree of

Doctor of Philosophy

Division of Engineering and Applied Science

California Institute of Technology

Pasadena, California 91125

1986

(Submitted December 20, 1985)

ACKNOWLEDGEMENTS

I would like to express my deepest appreciation to professor Christopher Brennen for his advice and encouragement in developing the theoretical portions of this thesis. I also want to thank professors Allan Acosta and Thomas Caughey for their support in the lab and professor Dara Childs at Texas A&M for suggesting that I pursue a doctorate at Caltech in the first place.

For their help in preparing the thesis, I give my eternal gratitude to Susan Berkley and Carol Leslie Jones. I would like to further thank Carol Jones for the moral support she has given me for the past few years.

Most of the technical expertise in the lab was provided by Ronald Franz and Norbert Ardnt, and to them I am grateful. I also appreciated the help of John Lee in keeping the system running and Elmer Sombathy for teaching me how to use the shop equipment. My predecessors, Belgacem Jery and Dimitri Chamieh deserve recognition too for their many contributions to the test facilities.

Finally, I would like to thank my mother and grandmother for being so understanding while I have spent the last twenty two years in school. I also want to thank the Shell Companies Foundation for the healthy financial support it provided.

This thesis is dedicated to NASA research contract NAS 8-33108 for supplying the money that has kept this project going.

ABSTRACT

It has been experimentally determined by previous investigators that hydrodynamic forces can cause a centrifugal pump impeller to whirl in a volute. The present work was undertaken to develop a theoretical model of the interactions that occur between an impeller and a volute, and to identify the source of the hydrodynamic forces. Experiments were then conducted to test the predictions of the model. The theoretical analysis presents a quasi-one dimensional treatment of the flow in the volute and accounts for the disturbance at the impeller discharge that is caused by the volute. The model also considers the lack of perfect guidance through the blade passages. Extending this model allowed for the calculation of hydrodynamic force perturbations that result when the impeller whirls eccentrically in the volute. These force perturbations were shown to encourage, rather than dissipate the whirling motion. The predictions of the model gave reasonable comparisons with the experimental data obtained in this study. Further, it was experimentally observed that pressure forces acting on the front shroud of the impeller could have a major influence on the hydrodynamic force perturbations acting on an eccentrically positioned impeller.

TABLE OF CONTENTS

LIST OF FIGURES

LIST OF TABLES

LIST OF SYMBOLS:

$\underset{\sim}{a}$	absolute acceleration of fluid element in impeller
a_s	acceleration in streamwise direction
a,c	dummy variables defined where used
b	discharge width of impeller blade passage
$\underset{\sim}{e}$	unit vector
h	total head $(h^* = 2h/\rho\Omega^2 R_2^2)$
j	$\sqrt{-1}$
$\underset{\sim}{k}$	impeller phase coefficient = $\cos(\tan\gamma \ln(R)) + j \sin(\tan\gamma \ln(R))$
$\overline{\ln rA}$	log moment of volute cross sectional area
q	perturbation in flow rate due to whirl
r,θ	polar coordinate system
$\overline{rA}$	first moment of volute cross sectional area
$\overline{rrA}$	second moment of volute cross sectional area
$\overline{r\ln rA}$	radial log moment of volute cross sectional area
s,η	direction tangnetial and normal to flow path
t	time

u absolute velocity of impeller flow

v relative velocity of impeller flow

w width in volute

x,y,z rectangular coordinate system

$\bar{A}$ volute cross sectional area

A_{ij} ($i = x,y$, $j = x,y$) components of generalized hydrodynamic force matrix [A] $(A^*_{ij} = A_{ij}/\rho\pi b\Omega^2 R_2^3)$

AR area ratio at tongue = $\bar{A}(0)/\bar{A}(2\pi)$

$C(\theta')$ velocity coefficient for total head in volute

C_p pressure coefficient at impeller discharge = $2(P_i(R_2,\theta) - h_1)/\rho\Omega^2 R_2^2$

C_r radius of stream path curvature in impeller

C_v velocity coefficient at volute discharge

C_{ij} ($i = x,y$, $j = x,y$) components of damping force matrix [C] $(C^*_{ij} = C_{ij}/\rho\pi b\Omega R_2^2)$

D_p pressure coefficient at volute inlet = $2(P_v(R_2',\theta') - h_1)/\rho\Omega^2 R_2^2$

F force acting on impeller $(F^* = F/\rho\pi b\Omega^2 R_2^3)$

$F(t)$ integration constant in Bernoulli's equation

J_{ij} ($i = x,y$, $j = x,y$) coefficients of the jerk force matrix [J] $(J^*_{ij} = J_{ij}/\rho\pi b R_2^2/\Omega)$

K_{ij} ($i = x,y$, $j = x,y$) components of stiffness force matrix [K] ($K^*_{ij} = K_{ij}/\rho\pi b\Omega^2 R_2^2$)

M_{ij} ($i = x,y$, $j = x,y$) components of inertia force matrix [M] ($M^*_{ij} = M_{ij}/\rho\pi b R_2^2$)

MA_{ij} ($i = x,y$, $j = x,y$) components of "mass alone" matrix (defined in Equation 3.9)

MC,MD off diagonal and diagonal elements of the [MA] matrix

P_i pressure in impeller ($P^*_i = 2P_i/\rho\Omega^2 R_2^2$)

P_v pressure in volute ($P^*_v = 2P_v/\rho\Omega^2 R_2^2$)

Q total volumetric flow rate through pump

R impeller radius (when no subscript $R = R_2/R_1$)

V velocity in volute (when no subscript $V^* = V_{\theta},/\Omega R_2$)

W_i width of impeller at R_2 ($W^*_i = W_i/b$)

α difference between angles measured in volute and impeller systems

β perturbation function for impeller flow

ζ angular location of the impeller center

θ_v angular position in the volute where the average flow velocity is independent of the overall flow rate

γ angle of flow path through impeller

ε distance between impeller and volute centers ($\varepsilon^* = \varepsilon/R_2$)

ρ fluid density

ϕ flow coefficient = $Q/2\pi\, b\, \Omega\, R_2^2$

ψ total head rise coefficient = $(h - h_1)/\rho\, \Omega^2 R_2^2$

ω orbit speed of impeller center

Ω rotational speed of impeller

Subscripts:

c quadrature or cos ωt component (non-dimensionalized)

d downstream of pump

exp experimental result

m force component due to momentum exchange

o off design

p force component due to pressure

r,θ radial or angular component

s in phase or sin ωt component (non-dimensionalized)

theo theoretical result

x,y components in rectangular directions (real = x and imaginary = y)

D design

0 center position in the volute

1 impeller inlet

2 impeller discharge

Superscripts:

' measurement made in volute reference frame

'' measurement made from frame fixed to rotating impeller

* non-dimensionalized quantity

Special Notation:

$\underset{\sim}{V}$ under bar denotes vector quantity

$\overline{V}$ over bar denotes centered impeller value (non-dimensionalized)

[A] square brackets denote a matrix quantity

$\dot{x}$ dot represents a time derivative

Chapter 1

INTRODUCTION

1.1 Historical Perspective

Given a rather broad definition, a pump might be considered as any device that could be used to increase the elevation of liquids, solids, or gases. One of the earliest known devices to be used in such an application was the undershot-bucket waterwheel which made its appearance in Asia and Africa about 3000 years ago, and is still in common use today. The invention that is commonly thought of as being the first pump though, is Archimedes' screw pump that was developed around 250 B.C.. Modern versions of these pumps can still be seen pumping water over the dikes of Holland. Initially, pumps were used primarily for agricultural and domestic purposes, but when mining operators began exploring at levels lower than the local water tables, an industrial interest in pumps began as well.

Most of the early pumps were of the positive displacement type, meaning that they relied on volume changes to transport the fluid such as in piston pumps, screw pumps, and the human heart. The idea that centrifugal force could be used to move liquids was suggested by Leonardo da Vinci in the fifteenth century but apparently the application of such a device had already been discovered by fifth century copper miners in Portugal. With the introduction of rotary steam engines and (later) electric motors, the centrifugal pump gained in popularity to become one of the predominant types of pumps in use today. Such pumps are relatively inexpensive to operate given the amount of fluid that they move, and have

allowed many areas of the world to grow beyond the capacity of their own local water resources (e.g., Los Angeles, California).

It is the study of the centrifugal pump that will be the main focus of this research. Inspiration for work in this area is due in part to the recent aerospace applications of such devices, particularly in connection with the High Pressure Fuel Turbopumps of the Space Shuttle. The special requirements of high power to weight ratios coupled with the necessity for reliability, have led to new problems that cannot be properly addressed by previous design practices.

1.2 Defining the Problem

1.2.1 Description of a Centrifugal Pump

Conceptually, the centrifugal pump has a fairly simple design consisting of only the two principle parts shown in Figure 1.1. The basic idea is that the fluid will axially enter into the center of the rotating impeller where it turns and passes into the moving blade passages. There, the fluid will gain momentum and pressure, and then be discharged into volute. In the volute the flow is collected and the high velocity flow at the impeller discharge is diffused into a high pressure flow. Some modifications on this concept have been made, such as placing vanes at the volute inlet to guide the flow, but fundamentally the pump remains unchanged.

In the past, pumps were designed so that their physical size generally correlated directly with the job requirements. For high power applications where weight is relatively unimportant compared to reliability, the systems chosen are typically large and run at lower speeds (less than 3000 RPM). But when the weight becomes an important factor, smaller pumps are required with much higher operating speeds (greater than 30,000

RPM). Along with the higher speeds come larger forces acting on the impeller, and the option of simply using a heavier drive train is no longer viable. Because of this situation, it becomes necessary to have a clearer understanding of what causes the forces on the impeller and what can be done to minimize their impact.

Several sources, both dynamic and hydrodynamic, have been identified as contributing to the forces on the impeller. One area that has received a great deal of attention is the force on the impeller that is generated by fluid in the annular seals separating the high pressure discharge of the pump from the relatively low pressure inlet (see for instance Black and Jensen [2], or Childs [11]). Other forces that are beginning to generate interest are the ones caused by fluid trapped between the front shroud of the impeller and the pump housing. These latter forces will be briefly investigated in this study, but the main focus will be placed on the hydrodynamic forces that arise from the interaction between the impeller and its accompanying volute.

It is traditional in studies of hydraulic forces on turbomachinery to separate the forces into one of two categories. In the first category are the forces that are developed when the rotor (impeller) is in the "centered" position. For an axial symmetric case it is easy to identify the center, but in the case of a spiral volute it is usually defined by the volute design criteria. In the second category are the forces caused by an eccentric positioning of the rotor.

1.2.2 Radial Forces on the Centered Impeller

The usual hypothesis in designing a volute for a given impeller is that it should offer a minimum interference to the symmetric flow pattern that would result if no volute was present. These free flow patterns

will change, however, with both impeller speed and discharge flow rate. For this reason, the volute can only be designed for a particular speed and flow rate, and in general, for any deviation from this point the volute will cause a disturbance in the impeller discharge flow. The end result of this interference is that the asymmetric pressure and velocity distributions at the impeller discharge will cause a net force acting on the impeller at the "off design" conditions.

As a crude approximation, it might be assumed that the radial forces are related to the discharge pressure times the area at the outer perimeter of the impeller. It is also known from an elementary treatment of the impeller (see for instance Streeter and Wylie [26]), that the discharge pressure is proportional to the square of the impeller tip speed. This would indicate that the forces on the centered impeller should scale with the square of the rotational speed and the cube of the outer diameter of the impeller. So when the impeller speed is increased by a factor of 10, it can be anticipated that the radial forces will increase by a factor of 100.

1.2.3 Forces on the Eccentrically Positioned Impeller

Forces will result on the impeller even at the design flow rate if the impeller is not in the center of the volute. The impeller may be dislocated from the center for a number of reasons, such as manufacturing flaws, bearing wear, or even shaft deflection from the radial forces mentioned above. When this happens, one must ask whether the resulting forces tend to restore the rotor to the original position or drive it further off center. There is also a third option, called "impeller whirl" or "whip", where the forces drive the impeller into a circular orbit about the center. Usually the forces are linearized with respect

to the small eccentric displacement of the impeller, so that the total force may be written as,

$$\underset{\sim}{F} = \begin{Bmatrix} F_x \\ F_y \end{Bmatrix} = \begin{Bmatrix} F_{x0} \\ F_{y0} \end{Bmatrix} + \begin{bmatrix} A_{xx} & A_{xy} \\ A_{xy} & A_{yy} \end{bmatrix} \begin{Bmatrix} \varepsilon \cos \omega t \\ \varepsilon \sin \omega t \end{Bmatrix} , \qquad (1.1)$$

where F_{x0} and F_{y0} are the steady forces on the impeller when it is located in the center of the volute. The [A] matrix, which is a function of the whirling speed of the impeller, relates the instantaneous force to the displacement. Often the [A] matrix is expanded as a quadratic of the whirl speed, ω, so that it can be described in terms of stiffness, damping, and inertial effects (see Equation 3.7).

Recently, concern has developed that the eccentric contribution to the force may cause the impeller to whirl at a speed other than that of the main shaft. In an article by Ehrich and Childs [14], it was emphasized that subsynchronous vibrations will generally cause a more hazardous failure than the one associated with synchronous vibrations. Part of the reasoning they give for this is that the synchronous vibrations (which are typically associated with unbalanced rotors) tend to cause the shafts to whirl in a "frozen" flexed condition. Subsynchronous vibrations, on the other hand, will cause alternating flexural stresses in the rotors because of the differences in rotational speeds. The problem will be further aggravated if the subsynchronous vibration occurs at a natural frequency of the shaft/impeller system. This would lead to exaggerated displacements associated with a particular mode shape for a given natural frequency.

1.3 Previous Investigations

1.3.1 Experimental Determination of Forces on a Centered Impeller

Even with the long history of centrifugal pump development, the theoretical models for such devices are still rather tentative, and most design improvements have come about through experimentation and practical experience. In connection with finding the hydrodynamic forces that act on the impeller, several experimental programs have been undertaken.

In 1936, Binder and Knapp [3] calculated the radial forces on a centrifugal pump impeller by measuring the pressures and velocities at the discharge of the impeller. The velocities were included because the authors had realized that an asymmetric momentum flux at the discharge would also contribute the force on the impeller. Knapp [18] later extended this work by studying the effect of using a single and a double spiral volute, as well as a volute with diffuser vanes. Using the same impeller for all three cases, he determined by static pressure measurements that a single spiral volute gives the greatest off design force on the impeller and the double spiral gives the least force.

Similarly, in 1961, Iversen, Rolling, and Carlson [15] performed pressure integrations to find the radial forces, but they also obtained the forces directly by measuring the bearing reactions of the shaft supporting the impeller. Their results indicated that the forces came primarily from the the pressure imbalance at the discharge. At the same time, in a paper by Agostinelli et al. [1], the forces were found by measuring the deflections of the shaft on which the impeller was mounted. They tested several volute configurations, including one hybrid of a circular and a spiral volute that minimized the radial forces over a wide range of flow rates.

1.3.2 Experimental Determination of Forces on an Eccentrically Positioned Impeller

The need to determine the forces that result when the impeller is deflected from the volute center has only recently been recognized. As a result, there are only a few pertinent experimental studies. Ohashi and Shoji [23] have undertaken an investigation where a two dimensional impeller is placed in a large circular diffuser in order to minimize the generation of steady radial forces. With a variable displacement eccentric drive mechanism they were able to cause the impeller to whirl in a circular orbit while measuring the resulting bearing reactions. Their results indicate that at low flow rates and low whirl speeds, the forces are such that there is a possibility of self-induced impeller whirl.

Another test facility also exists in the pump division at Sultzer Brothers Limited in Switzerland. Bolleter and Wyss [4] describe the pump as modeling a single section of a multi-stage pump with a vaned diffuser. The pump is constructed so that there are axial symmetric conditions at the discharge (for a centered impeller) and therefore the mean forces are eliminated. The shaft supporting the impeller is forced to undergo a small single direction translational motion, and the resulting two direction deflection of the impeller is measured with eddy current probes. The forces are found using strain gages mounted in a rotating cylinder at the base of the impeller. The results from this facility also show that for certain flow conditions impeller whirl may occur.

At the California Institute of Technology, a test program was developed by Brennen, Acosta, and Caughey [7] so that whirl excitation forces could be determined using realistic pump configurations. In their facility, the center of the impeller was caused to orbit in a circular

path of a fixed radius inside of a volute. The forces were obtained by measuring the displacement of the entire eccentric drive assembly on which the impeller was mounted. Results of this program given by Chamieh et al. [9,10], demonstrated that for both spiral and circular volutes, the forces resulting from a stationary displacement of the impeller would cause the impeller to orbit.

Work at the Caltech facility was extended by Jery et al. [16,17] to include hydrodynamic forces generated by a whirling impeller. The test section was modified so that the forces were measured directly at the base of the impeller with a strain gage balance. This study presented the dependence of the whirl excitation forces on both whirl frequency and the pump configuration.

1.3.3 Theoretical Analyses of Volute-Impeller Interactions

Because of the complicated geometries in centrifugal pumps, simple theories that adequately describe the internal flows do not exist. Still, several models have been developed in order to explain and extrapolate experimental observations. These theoretical solutions generally fall into one of two categories depending on whether a one dimensional bulk flow approximation was made or a two dimensional potential flow was assumed.

Csanady [13] was the first to introduce the concept of using a potential flow analysis of the impeller and volute. In his model, a spiral volute was transformed into an equivalent flat-plate cascade through a conformal mapping. Pressure forces on the impeller were determined by assuming that the total head was constant around the impeller periphery. This work was later broadened by Colding-Jorgensen [12] to include the effects of whirling. Colding-Jorgensen's model not

only predicted hydrodynamic forces, but it also gave stiffness and damping terms associated with the displacement of the impeller in a spiral volute.

Singularity methods were used by Shoji and Ohashi [24] to calculate fluid forces on an impeller in an unbounded region. To model the effect of an eccentric displacement of the impeller on the inlet conditions, they introduced small velocity perturbations in the flow field within the blade passages. Shockless entry conditions are assumed for the steady portion of the flow and vortices shed from the trailing edges of the blades are considered to be carried downstream along the steady streamlines at steady velocities. Tsujimoto, Acosta, and Brennen [28,29] also used singularity methods for finding the unsteady forces on a whirling impeller, but in their analysis the influence of the volute on the downstream flow was included.

A bulk flow model was purposed by Kurokawa [19] in which the flow field is divided into a diffuser region immediately at the impeller discharge, and a volute region afterwards. The equations of continuity and motion were satisfied for the flow in the diffuser region that was treated as a narrow annular gap with inlet conditions described by Busemann [8]. The flow in the volute was considered as an equivalent convergent or divergent straight channel, depending on whether the pump was being operated at high or low flow rates. These calculations predicted the steady fluid forces acting on the impeller.

Lorett [21] has also developed a bulk flow model that includes an approximation for the flow in the impeller and accounts for the effects of friction. The flow was assumed to be perfectly guided by the impeller blades and allowances were made for the peripheral variations at the discharge. Pressure distributions in the volute were obtained by linear

momentum considerations so that the steady radial forces could be calculated.

Finally, the study that the current research most closely parallels was given by Iversen, Rolling, and Carlson [15]. They presented a quasi-one dimensional treatment of the internal flows with the pressure being obtained by continuity and a linear momentum balance in the volute. The radial velocity at the inlet of the volute was assumed to be uniform and the tangential velocity was obtained using Stodola's [27] correction factor. Comparisons between their predicted and experimental results were given.

1.4 Goals of the Present Research

The need for analytical design methods in turbomachinery is clear. Previously it has been accepted that accurate information could only be obtained through extensive testing. As the pumping problems have grown more complex, the cost of maintaining a "trial and error" design program has become difficult to justify. For this reason it is necessary to provide the pump designer with analytical tools so that only a limited testing program is required.

The current research is undertaken to provide a comprehensive theoretical analysis to compliment the experimental program conducted at the California Institute of Technology by Brennen, Acosta, and Caughey [7], Chamieh [9], and Jery [16]. The ultimate aim is to develop a procedure by which the hydrodynamic radial forces on an impeller whirling in a volute can be predicted. A bulk flow analysis is chosen so that the model can be closely tied to the actual physical geometry of a centrifugal pump.

It was realized at the onset of this study that attempts had to be

made to validate the model at several levels of complexity. For this reason, an experimental program on the interaction between a non-whirling impeller and the volute is included in this thesis. There will also be a limited investigation of other sources of fluid forces that may have influenced previous investigations. Altogether, it is hoped that this will provide a clearer understanding of the origins of the hydrodynamic forces so that the observations of past studies can be better understood and that future research in this area will have a clearer direction.

In this thesis an analytical model for the hydrodynamic interactions between a whirling impeller and the surrounding volute in a centrifugal pump will be developed and tested. The model is introduced in the following chapter and the theoretical predictions are presented in Chapter 3. Chapter 4 provides a description of the test facilities used in verifying the model. Correlations between the theoretical and experimental results are given in Chapter 5, along with comparisons to previous investigations. An examination of the hydrodynamic force on the front shroud of the impeller is also presented in Chapter 5. Finally, a summary of the experimental results and an assessment of the model are given in Chapter 6.

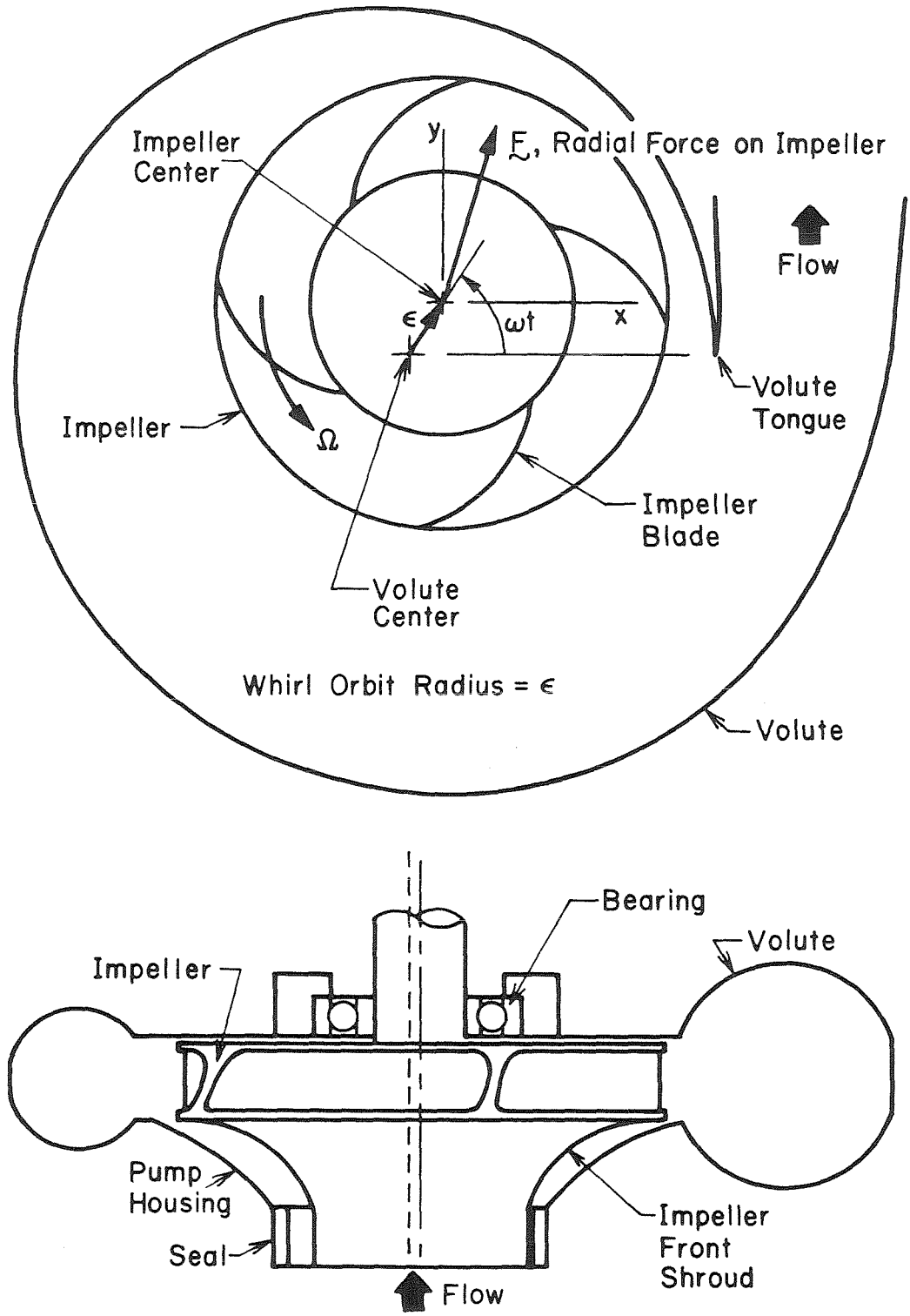

Figure 1.1 Description of a centrifugal pump

Chapter 2

THEORETICAL ANALYSIS OF A CENTRIFUGAL PUMP

2.1 Overview of the Analysis

In order to model the flow through the centrifugal pump, the problem will be broken down into two parts. First, the flow through the impeller will be investigated, and second, the flow through the volute will be considered. A circumferentially periodic perturbation of the flow is assumed in the impeller model to give a periodic non-uniformity in the flow conditions at the exit of the impeller. Non-uniform inlet flow conditions are then included in the volute analysis so that the volute and impeller models can be combined by matching pressures and flow rates at the impeller discharge. This matching of conditions will allow the magnitude and phase of the impeller flow perturbation to be found. It also allows the radial forces on the impeller that result from such a circumferential perturbation to be calculated.

2.2 Impeller Model

2.2.1 Introduction

The primary objective of the impeller model is to relate the pressure and velocity at the exit of the impeller to the pressure and velocity at the inlet. In order to do so, the flow is considered to be inviscid and two dimensional throughout the blade passage and an unsteady form of Bernoulli's Equation is used in describing the variation in pressure and velocity along an instantaneous streamline in the impeller. The form of Bernoulli's Equation used is developed in Appendix A, but for convenience it will be repeated here. With reference to Figure 2.1 it is

given as,

$$\frac{P_i}{\rho} + \frac{v^2}{2} - \frac{\Omega^2 r''^2}{2} + \int_{s''} \frac{\partial v}{\partial t}\, ds'' - \omega^2 \varepsilon \int_{s''} \cos(\omega t - \Omega t - \theta'')\, dr''$$

$$- \omega^2 \varepsilon \int_{s''} \sin(\omega t - \Omega t - \theta'') r''\, d\theta'' = F(t) \quad , \qquad (2.1)$$

where F(t) is a function of only time along a streamline, but may vary from one streamline to another.

Here Bernoulli's Equation is still in a fairly general form and to be of any use in modeling the impeller flow some restrictions must be placed on the flow path through the impeller. In an idealized model it would be assumed that there are an infinite number of blades, perfectly guiding the flow from the inlet to the discharge of the impeller. In this situation the flow path would correspond exactly with the blade passage. But most impellers use only a small number of blades for practical reasons (i.e., reducing friction and flow blockage), so it is unlikely that the flow can be considered as perfectly guided through a blade passage. Alternatively, it is just as unlikely that the blades have no influence on the fluid at all and that the flow appears as a simple source flow in the volute reference frame.

Estimating how well the flow is guided through the impeller has long been a problem faced by centrifugal pump designers. One of the more popular methods used to deal with this difficulty has been to assign a "slip factor" to the velocity at the impeller discharge. The slip factor is included to account for the difference between the predicted head rise across the impeller (assuming perfectly guided flow) and the total head rise which is actually observed. A rather extensive review of these factors is given by Wiesner [30] where both theoretical and empirical results are presented. There are, however, two major drawbacks to using

a slip factor approach in this study. The first shortcoming is that the factors do not take into account the influence of the volute on the flow at the discharge of the impeller and it is known that the volute can make an important difference (see Bowerman and Acosta [5]). The second drawback is that the slip factors generally apply only to the velocity at the impeller exit while the current model needs the velocity profile throughout the impeller.

2.2.2. Velocity Profile in the Impeller

In order to find a compromise in dealing with the flow path dilemma, it is assumed that the flow follows a spiral path with respect to the rotating impeller, with the kinematic relationship between the radial and angular velocities being,

$$\frac{v_{\theta''}}{v_{r''}} = \frac{r'' d\theta''}{dr''} = -\tan\gamma(\phi,\bar{\psi}) \qquad \text{for} \quad R_1 < r'' \leq R_2 \quad . \tag{2.2}$$

The angle, γ, in the expression will be referred to as the flow path angle and in the idealized perfectly guided case it would be equal to the blade angle, γ_B. For the time being, the flow path angle will remain as an unknown, and will be considered to be a function of only the flow rate and the total head rise for the centered impeller. It should be emphasized that this is a major assumption, because by making it the streamlines relative to the impeller will be treated as uniform and independent of the position of the impeller. The streampaths which follow from this assumption are given by the equation,

$$\theta_2'' = \theta'' + \tan\gamma \ln(r''/R_2) \quad , \tag{2.3}$$

with R_2, θ_2'' being the terminal point of each stream path. Some

generality is still maintained by having the flow path angle change with ϕ and $\overline{\psi}$. Doing so will allow for the streampaths in the impeller to change when different exit conditions are imposed on the impeller by the volute and downstream conditions.

For the problem of an impeller discharging into cylindrically symmetric environment, continuity requires that the radial velocity is inversely proportional to the radial distance from the center. In accordance with this observation, the radial velocity within the impeller is written in the form,

$$v_{r''} = \phi\,\Omega\,R_2^2\,\beta(\theta'',r'',\Omega t,\omega t,\varepsilon)/r'' \quad , \tag{2.4}$$

and the streamwise velocity through the impeller is,

$$v = (v_{r''}^2 + v_{\theta''}^2)^{1/2} = \phi\,\Omega\,R_2^2\,\beta(\theta'',r'',\Omega t,\omega t,\varepsilon)\sec\gamma/r'' \quad , \tag{2.5}$$

$$\text{for} \quad R_1 < r'' \leq R_2 \quad .$$

The function β in Equations 2.4 and 2.5 is included to account for the influence of the volute on the flow in the impeller. Although the number of variables in β makes it appear complicated, some progress towards simplification can be made by realizing the relationships that must exist between the variables. First, the perturbation associated with β must be constant along a streampath so that continuity is satisfied. For the flow perturbation within the impeller to be the same as that at the discharge will require that the relationship between r'' and θ'' in β be given by Equation 2.3. Next, because the perturbation is caused by the volute, it is reasonable to expect that β is stationary in the volute reference frame for a non-whirling impeller. This would suggest that θ'' and Ωt arguments of β combine as $\theta = \theta'' + \Omega t$.

It now remains to determine the dependence of β on ε and ωt. Since the eccentricity of the impeller orbit, ε, is small, the perturbation function, β, will be linearized in ε as,

$$\beta(\theta'', r'', \Omega t, \omega t, \varepsilon) = \bar{\beta}(\theta_2) + \varepsilon^* \{\beta_c(\theta_2)\cos \omega t + \beta_s(\theta_2)\sin \omega t\} \quad . \quad (2.6)$$

The function $\bar{\beta}$, is the perturbation in the impeller flow caused by the interaction between the centered impeller and the volute. The functions β_c and β_s are introduced to account for the first harmonic effects on the perturbation due to the impeller whirling in the volute. All three components are functions of θ_2 but remain constant along each streampath in the impeller.

2.2.3. Pressure Distribution at the Impeller Discharge

Substituting the streamwise velocity of Equation 2.5 into Bernoulli's Equation and performing the integrations along the streamline described by Equation 2.3 results in,

$$\frac{P_i(R_2,\theta_2)}{\rho} + \frac{\Omega^2 R_2^2}{2}\{\phi\,\beta^2 \sec^2\gamma - 1\} - \omega^2 \varepsilon\{R_2\cos(\omega t - \theta_2) - R_1\cos(\omega t - \theta_1)\}/\tan^2\gamma$$

$$+ \phi\,\Omega\,R_2^2\sec^2\gamma \ln(R)\left[\Omega\frac{\partial \beta}{\partial \theta_2} + \omega\varepsilon^*\{-\beta_c \sin \omega t + \beta_s \cos \omega t\}\right]$$

$$= \frac{P_i(R_1,\theta_1)}{\rho} + \frac{v^2(R_1,\theta_1)}{2} - \frac{\Omega^2 R_1^2}{2} \quad . \quad (2.7)$$

From this equation the pressure distribution at the exit of the impeller is known in terms of the perturbation β and the inlet pressure and velocity.

At the inlet of the impeller the total head will be assumed to be constant. This will mean that where the flow enters the blade passage at $r=R_1$,

$$P_i(R_1,\theta_1) + \tfrac{1}{2}\rho u^2(R_1,\theta_1) = \text{constant} = h_1 \quad , \tag{2.8}$$

where $u(R_1,\theta_1)$ is the absolute velocity of the flow at the inlet. If it is assumed that there is no pre-swirl at the inlet, then the velocity of the flow entering the blade passage has only a radial component in the absolute reference frame, and is of the form,

$$u(R_1,\theta_1) = \phi\,\Omega\,\beta\,R_2^2/R_1 + \varepsilon\,\omega\sin(\theta_1 - \omega t) \quad . \tag{2.9}$$

This gives the velocity relative to the rotating impeller as,

$$v^*(R_1,\theta_1) = \{\phi^2 R^2 \beta^2 + [\varepsilon^* \tfrac{\omega}{\Omega}\cos(\theta_1 - \omega t) + 1/R]^2\}^{1/2} \quad , \tag{2.10}$$

and the pressure distribution at the inlet of the impeller as,

$$P_i^*(R_1,\theta_1) \cong h_1^* - \phi\,R\,\bar{\beta}(\theta_2)\{\phi\,R\,\bar{\beta}(\theta_2) + 2\varepsilon^* \tfrac{\omega}{\Omega}\sin(\theta_1 - \omega t)\}$$

$$- 2\varepsilon^*\phi^2 R^2\,\bar{\beta}(\theta_2)\{\beta_c(\theta_2)\cos\omega t + \beta_s(\theta_2)\sin\omega t\} \tag{2.11}$$

where $R = R_2/R_1$ and terms of order ε^2 and higher have been neglected.

When the assumptions concerning the inlet conditions are applied to Bernoulli's Equation, the result gives the pressure distribution at the exit of the impeller in terms of the perturbation function, β, and the inlet total head. It is further assumed that this pressure distribution can be separated into three parts and that terms of order ε^2 are negligible. The result is the following expression for the pressure distribution at the exit of the impeller,

$$C_p(\theta_2,\omega t,\varepsilon) = \bar{C}_p(\theta_2) + \varepsilon^*(C_{pc}(\theta_2)\cos\omega t + C_{ps}(\theta_2)\sin\omega t) \tag{2.12}$$

$$\cong P_i^*(R_2,\theta_2) - h_1^* \quad ,$$

where,

$$\bar{C}_p(\theta_2) = 1 - \phi \sec^2 \gamma [\phi \bar{\beta}^2(\theta_2) + 2 \ln(R) \frac{d\bar{\beta}}{d\theta_2}] \quad ,$$

$$C_{pc}(\theta_2) = -2\phi \sec^2 \gamma [\phi \bar{\beta}(\theta_2) \beta_c(\theta_2) + \ln(R) \frac{d\beta_c}{d\theta_2} + \frac{\omega}{\Omega} \ln(R) \beta_s(\theta_2)]$$

$$+ 2 \frac{\omega^2}{\Omega^2} [\cos(\theta_2) - \cos(\theta_2 + \tan\gamma \ln(R))/R]/\tan^2\gamma$$

$$- 2\frac{\omega}{\Omega} [\phi R \bar{\beta}(\theta_2) \sin(\theta_2 + \tan\gamma \ln(R)) - \cos(\theta_2 + \tan\gamma \ln(R))/R] \quad ,$$

and,

$$C_{ps}(\theta_2) = -2\phi \sec^2 \gamma [\phi \bar{\beta}(\theta_2) \beta_s(\theta_2) + \ln(R) \frac{d\beta_s}{d\theta_2} - \frac{\omega}{\Omega} \ln(R) \beta_c(\theta_2)]$$

$$+ 2 \frac{\omega^2}{\Omega^2} [\sin(\theta_2) - \sin(\theta_2 + \tan\gamma \ln(R))/R]/\tan^2\gamma$$

$$+ 2 \frac{\omega}{\Omega} [\phi R \bar{\beta}(\theta_2) \cos(\theta_2 + \tan\gamma \ln(R)) + \sin(\theta_2 + \tan\gamma \ln(R))/R] \quad .$$

2.2.4. Pressure Distribution at the Volute Inlet

Equation 2.12 will be used to solve for the perturbation function, β, once the pressure distribution, C_p, is obtained from the volute model. Some care must be observed in carrying out this procedure because it will prove more convenient to describe the pressure distribution at the volute inlet in terms of a volute centered coordinate system and not the impeller centered coordinates used above. This makes it necessary to establish certain geometric relationships between the two coordinate systems. With the aid of Figure 2.2 it is seen that,

$$\sin\alpha = \varepsilon^* \sin(\theta' - \omega t) \quad ,$$

or otherwise stated,

$$\alpha \cong \varepsilon^* \sin(\theta' - \omega t) \quad . \tag{2.13}$$

With this angle known, the angular positions θ_2 and θ' at R_2 may now be related by the approximation,

$$\theta_2 = \theta' + \alpha \cong \theta' + \varepsilon^* \sin(\theta' - \omega t) \quad . \tag{2.14}$$

An expression for R_2' may also be obtained from geometric considerations as,

$$R_2' \cong R_2[1 + \varepsilon^* \cos(\theta' - \omega t)] \quad . \tag{2.15}$$

The pressure distribution is assumed to be continuous from the impeller discharge to the volute inlet. Utilizing Equation 2.14, the relationship between the pressures is found to be,

$$C_p(\theta_2) = D_p(\theta') \cong D_p(\theta_2 - \varepsilon^* \sin(\theta_2 - \omega t)) \tag{2.16}$$

$$\cong D_p(\theta_2) - \varepsilon^* \sin(\theta_2 - \omega t) \frac{dD_p(\theta_2)}{d\theta_2} \quad .$$

If it is further assumed that the pressure distribution at the entrance of the volute may be linearized in ε as,

$$D_p(\theta') = \bar{D}_p(\theta') + \varepsilon^* [D_{pc}(\theta') \cos\omega t + D_{ps}(\theta') \sin\omega t] \quad , \tag{2.17}$$

then the final expression for the impeller discharge pressure in terms of the volute pressure distribution becomes,

$$C_p(\theta_2) = \bar{D}_p(\theta_2) + \varepsilon^*[(D_{pc}(\theta_2) - \sin\theta_2 \frac{d\bar{D}_p(\theta_2)}{d\theta_2})\cos\omega t$$

$$+ (D_{ps}(\theta_2) + \cos\theta_2 \frac{d\bar{D}_p(\theta_2)}{d\theta_2})\sin\omega t] \quad . \tag{2.18}$$

With this description of the pressure distribution and the previous results of Equation 2.12, Bernoulli's Equation resolves into three parts. Together these three parts relate the perturbation in the flow through the impeller to the pressure distribution at the inlet of the volute. The first part accounts for the interaction between the centered impeller and the volute. The other two parts yield the in-phase and quadrature components ($\sin\omega t$ and $\cos\omega t$ coefficients) of the first harmonic effects of the whirling impeller. These three equations are as follows :

steady term:

$$\phi \sec^2\gamma[2\ln(R)\frac{d\bar{\beta}}{d\theta_2} + \phi\bar{\beta}^2] + \bar{D}_p - 1 = 0 \tag{2.19a}$$

$\cos\omega t$ term:

$$2\phi\sec^2\gamma[\ln(R)\frac{d\beta_c}{d\theta_2} + \phi\bar{\beta}\beta_c + \frac{\omega}{\Omega}\ln(R)\beta_s] + D_{pc} - \sin\theta_2\frac{d\bar{D}_p}{d\theta_2}$$

$$+ 2\frac{\omega}{\Omega}[\phi R\bar{\beta}\sin(\theta_2 + \tan\gamma\ln(R)) - \cos(\theta_2 + \tan\gamma\ln(R))/R]$$

$$- 2\frac{\omega^2}{\Omega^2}[\cos\theta_2 - \cos(\theta_2 + \tan\gamma\ln(R))/R]/\tan^2\gamma = 0 \tag{2.19b}$$

sin ωt term :

$$2\phi \sec^2 \gamma[\ln(R)\frac{d\beta_s}{d\theta_2} + \phi \bar{\beta}\beta_s - \frac{\omega}{\Omega} \ln(R)\beta_c] + D_{ps} + \cos\theta_2 \frac{d\bar{D}_p}{d\theta_2}$$

$$- 2 \frac{\omega}{\Omega} [\phi R \bar{\beta} \cos(\theta_2 + \tan\gamma \ln(R)) + \sin(\theta_2 + \tan\gamma \ln(R))/R]$$

$$- 2 \frac{\omega^2}{\Omega^2} [\sin\theta_2 - \sin(\theta_2 + \tan\gamma \ln(R))/R]/\tan^2\gamma = 0 \quad . \qquad (2.19c)$$

2.3 Volute Model

The volute model is developed so that the flow conditions at the exit of the impeller may be related to the geometry of the volute. The three basic equations used in the volute model are the continuity equation, the moment of momentum equation, and the radial equation of motion. These three equations are derived in Appendix B but will be repeated here for convenience. With reference to the geometry described in Figure 2.3, the basic equations are as follows.

continuity :

$$\frac{\partial}{\partial\theta'}\left[V_\theta' \int_{R_2'}^{R_3'} w\, dr'\right] = w|_{R_2'}(V_r'|_{R_2'} R_2' - V_\theta'|_{R_2'} \frac{\partial R_2'}{\partial\theta'}) \quad . \qquad (2.20)$$

moment of momentum :

$$\frac{\partial}{\partial\theta'}\left[V_\theta'^2 \int_{R_2'}^{R_3'} wr'dr'\right] + w V_\theta'^2|_{R_2'} R_2' \frac{\partial R_2'}{\partial\theta'} - w V_\theta' V_r'|_{R_2'} R_2' R_2'$$

$$+ \frac{\partial}{\partial t}\left[V_\theta' \int_{R_2'}^{R_3'} w\, r'r'dr'\right] + w V_\theta'|_{R_2'} R_2' R_2' \frac{\partial R_2'}{\partial t}$$

(continued)

$$= -\frac{1}{\rho}\frac{\partial P_v(R_2',\theta')}{\partial\theta'}\int_{R_2'}^{R_3'} w\, r'dr' - \frac{\partial V_{\theta'}^2}{\partial\theta'}\int_{R_2'}^{R_3'} w\, r'\ln(r'/R_2')dr'$$

$$+ V_{\theta'}^2,\ \frac{1}{R_2'}\frac{\partial R_2'}{\partial\theta'}\int_{R_2'}^{R_3'} w\, r'dr' \quad . \tag{2.21}$$

radial equation of motion :

$$P_v(r',\theta') = P_v(R_2',\theta') + \rho V_{\theta'}^2,(\theta')\ln(r'/R_2') \quad . \tag{2.22}$$

Underlying the development of these equations were the assumptions that within the volute the flow is primarily in the θ' direction, and that this velocity is a function of only θ' and t . The radial and axial velocities along with their gradients were considered negligible and any viscous effects are also ignored.

Using the expression for R_2' given by Equation 2.15, the volute cross section integrals may be written in terms of their mean quantities and a perturbation due to the eccentric impeller position. With an additional assumption that the width of the volute at the impeller discharge is a constant, W_i, the cross section integrals are given by,

$$\int_{R_2'}^{R_3'} wdr'/bR_2 = \overline{A}(\theta') - \varepsilon^* W_i\cos(\theta' - \omega t)/b \ ,$$

$$\int_{R_2'}^{R_3'} r'wdr'/bR_2^2 = \overline{rA}(\theta') - \varepsilon^* W_i\cos(\theta' - \omega t)/b \ ,$$

$$\int_{R_2'}^{R_3'} r'r'wdr'/bR_2^3 = \overline{rrA}(\theta') - \varepsilon^* W_i\cos(\theta' - \omega t)/b \ ,$$

$$\int_{R_2'}^{R_3'} \ln(r'/R_2')wdr'/bR_2 = \overline{\ln rA}(\theta') - \varepsilon^* \overline{A}(\theta')\cos(\theta' - \omega t) \quad ,$$

$$\int_{R_2'}^{R_3'} r'\ln(r'/R_2')wdr'/bR_2^2 = \overline{r\ln rA}(\theta') - \varepsilon^* \overline{rA}(\theta')\cos(\theta' - \omega t) \quad ,$$

and,

$$\frac{1}{R_2'} \frac{\partial R_2'}{\partial \theta'} \int_{R_2'}^{R_3'} r'wdr'/bR_2^2 = - \varepsilon^* \overline{rA}(\theta') \sin(\theta' - \omega t) \quad ,$$

where,

$$\overline{A}(\theta') = \int_{R_2}^{R_3'} wdr'/bR_2 \quad , \quad \overline{\ln rA}(\theta') = \int_{R_2}^{R_3'} \ln(r'/R_2)wdr'/bR_2 \quad , \qquad (2.23a,b)$$

$$\overline{rA}(\theta') = \int_{R_2}^{R_3'} r'wdr'/bR_2^2 \quad , \quad \overline{rrA}(\theta') = \int_{R_2}^{R_3'} r'r'wdr'/bR_2^3 \quad , \qquad (2.23c,d)$$

$$\overline{r\ln rA}(\theta') = \int_{R_2}^{R_3'} r'\ln(r'/R_2)wdr'/bR_2^2 \quad , \qquad (2.23e)$$

and b is the width of the impeller discharge.

In order to complete the connection between the impeller discharge and the volute inlet, the relationships between the velocities must be found. From kinematic relationships and Equations 2.2 and 2.4 of the impeller study, it is known that the velocity distribution at the impeller discharge is given by,

$$\underset{\sim}{u}(R_2,\theta) = [\phi\, \Omega\, R_2 \beta(\theta_2) + \omega\, \varepsilon \sin(\theta_2 - \omega t)]\underset{\sim}{e}_r$$

$$+ [\Omega\, R_2(1 - \phi \tan\gamma\, \beta(\theta_2)) + \omega\, \varepsilon \cos(\theta_2 - \omega t)]\underset{\sim}{e}_\theta \quad , \qquad (2.24)$$

where, as was previously described, the perturbation function is given as,

$$\beta(\theta_2,\omega t,\varepsilon) = \bar{\beta}(\theta_2) + \varepsilon^*[\beta_c(\theta_2)\cos\omega t + \beta_s(\theta_2)\sin\omega t] \quad . \tag{2.6}$$

It will be assumed that this velocity is equal to the velocity at the inlet of the volute. Care must be taken at this point, however, because what is needed is the velocity at the volute inlet in terms of the volute reference frame. The unit vectors appearing in Equation 2.24 can be approximated in the volute reference frame by using the unit vector transformations,

$$\underset{\sim}{e}_r \cong \underset{\sim}{e}_{r'} + \varepsilon^*\sin(\theta' - \omega t)\underset{\sim}{e}_{\theta'} \quad , \tag{2.25a}$$

and

$$\underset{\sim}{e}_\theta \cong -\varepsilon^*\sin(\theta' - \omega t)\underset{\sim}{e}_{r'} + \underset{\sim}{e}_{\theta'} \tag{2.25b}$$

In addition, the perturbation function, $\beta(\theta_2)$, may also be written in terms of the volute coordinates as,

$$\beta(\theta_2) \cong \beta(\theta' + \varepsilon^*\sin(\theta' - \omega t)) \cong \beta(\theta') + \varepsilon^*\sin(\theta' - \omega t)\frac{d\bar{\beta}(\theta')}{d\theta'} \quad , \tag{2.26}$$

which, when combined with the Equation 2.6 becomes,

$$\beta(\theta_2) \cong \bar{\beta}(\theta') + \varepsilon^*\{[\beta_c(\theta') + \sin\theta'\frac{d\bar{\beta}(\theta')}{d\theta'}]\cos\omega t$$

$$+ [\beta_s(\theta') - \cos\theta'\frac{d\bar{\beta}(\theta')}{d\theta'}]\sin\omega t\} \quad . \tag{2.27}$$

Incorporating the preceding transformations gives the velocity components of the flow entering the volute from the impeller as,

$$\frac{V_r'(R_2',\theta')}{\Omega R_2} = \phi\{\bar{\beta}(\theta') + \varepsilon^*[\beta_c(\theta')\cos\omega t + \beta_s(\theta')\sin\omega t]\}$$

$$- \varepsilon^*[1 - \phi\tan\gamma\,\bar{\beta}(\theta') - \phi\frac{d\bar{\beta}(\theta')}{d\theta'}]\sin(\theta' - \omega t)$$

$$+ \varepsilon^*\frac{\omega}{\Omega}\sin(\theta' - \omega t) \qquad (2.28)$$

and,

$$\frac{V_\theta'(R_2',\theta')}{\Omega R_2} = 1 - \phi\tan\gamma\{\bar{\beta}(\theta') + \varepsilon^*[\beta_c(\theta')\cos\omega t + \beta_s(\theta')\sin\omega t]\}$$

$$+ \varepsilon^*\phi[\bar{\beta}(\theta') - \tan\gamma\frac{d\bar{\beta}(\theta')}{d\theta'}]\sin(\theta' - \omega t)$$

$$+ \varepsilon^*\frac{\omega}{\Omega}\cos(\theta' - \omega t) \qquad (2.29)$$

Both the continuity and the moment of momentum equations may now be broken into three parts by substituting the preceding relationships for cross sectional area integrals and the inlet velocities. These three parts are : (1) a steady mean flow term that is due to the interaction between the centered impeller and the volute; (2) an unsteady term with a $\cos\omega t$ dependence generated by the whirling impeller; and (3) an unsteady term with a $\sin\omega t$ dependence. The three components of the continuity equation are :

steady centered :

$$\frac{d(\bar{V}\,\bar{A})}{d\theta'} = \phi\bar{\beta} \qquad (2.30a)$$

whirling cos ωt :

$$\frac{d(V_c\bar{A})}{d\theta'} = W_i^* \frac{d(\bar{V}\cos\theta')}{d\theta'} + \frac{\omega}{\Omega}\sin\theta' + \phi[\beta_c + \frac{d(\bar{\beta}\sin\theta')}{d\theta'}] \qquad (2.30b)$$

whirling sin ωt :

$$\frac{d(V_s\bar{A})}{d\theta'} = W_i^* \frac{d(\bar{V}\sin\theta')}{d\theta'} - \frac{\omega}{\Omega}\cos\theta' + \phi[\beta_s - \frac{d(\bar{\beta}\cos\theta')}{d\theta'}] \qquad (2.30c)$$

In the above equations $\beta = \beta(\theta')$, and the tangential velocity in the volute is separated into components as,

$$V^*(\theta') = \bar{V}(\theta') + \varepsilon^*[V_c(\theta')\cos\omega t + V_s(\theta')\sin\omega t] \cong \frac{V_{\theta}'}{\Omega R_2} \quad . \qquad (2.31)$$

Similarly, the moment of momentum equation yields three parts relating the pressure gradients to the velocity distributions and the volute geometry. These three parts are :

steady centered :

$$\frac{\overline{rA}}{2}\frac{d\overline{D_p}}{d\theta'} = -\frac{d(\overline{rA}\,\bar{V}^2)}{d\theta'} - \overline{rlnrA}\,\frac{d(\bar{V}^2)}{d\theta'} + \phi(1 - \phi\tan\gamma\,\bar{\beta})\bar{\beta} \qquad (2.32a)$$

whirling cos ωt :

$$\frac{\overline{rA}}{2}\frac{dD_{pc}}{d\theta'} = -2\frac{d(\overline{rA}\,\bar{V}\,V_c)}{d\theta'} + \frac{\omega}{\Omega}(W_i^*\sin\theta'\bar{V} - \overline{rrA}\,V_s) \qquad (2.32b)$$

$$+ (W_i^* + \overline{rA})\frac{d(\bar{V}^2\cos\theta')}{d\theta'} - 2\overline{rlnrA}\,\frac{d(\bar{V}\,V_c)}{d\theta'}$$

$$+ \phi^2\sin\theta'\bar{\beta}^2 + \phi\cos\theta'(\frac{\omega}{\Omega} + 2 - 2\phi\tan\gamma\,\bar{\beta})\bar{\beta}$$

(continued)

$$+ \phi(1 - 2\phi \tan\gamma\, \bar{\beta})(\beta_c + \sin\theta' \frac{d\bar{\beta}}{d\theta'}) + \frac{W_i^*}{2} \cos\theta' \frac{d\overline{D_p}}{d\theta'}$$

whirling $\sin \omega t$:

$$\frac{\overline{rA}}{2} \frac{dD_{ps}}{d\theta'} = -2 \frac{d(\overline{rA}\,\bar{V}\,V_s)}{d\theta'} - \frac{\omega}{\Omega}(W_i^* \cos\theta' \bar{V} - \overline{rrA}\,V_c) \qquad (2.32c)$$

$$+ (W_i^* + \overline{rA}) \frac{d(\bar{V}^2 \sin\theta')}{d\theta'} - 2\overline{rlnrA} \frac{d(\bar{V}\,V_s)}{d\theta'}$$

$$- \phi^2 \cos\theta' \bar{\beta}^2 + \phi \sin\theta' (\frac{\omega}{\Omega} + 2 - 2\phi \tan\gamma\, \bar{\beta})\bar{\beta}$$

$$+ \phi(1 - 2\phi \tan\gamma\, \bar{\beta})(\beta_s - \cos\theta' \frac{d\bar{\beta}}{d\theta'}) + \frac{W_i^*}{2} \sin\theta' \frac{d\overline{D_p}}{d\theta'}$$

In these expressions the volute pressure coefficient is defined as,

$$D_p(\theta') = \overline{D_p}(\theta') + \varepsilon^* [D_{pc}(\theta') \cos\omega t + D_{ps}(\theta') \sin\omega t] \qquad (2.33)$$

$$\cong \frac{(P_v(R_2', \theta') - h_1)}{(\rho\, \Omega^2 R_2^2/2)} \,.$$

2.4 Closure Conditions

2.4.1 Restrictions on the Flow Perturbations in the Impeller

Although β is referred to as the perturbation function, nowhere in the derivation was it assumed to be small. However, by the definition of the flow coefficient, ϕ, one restriction has already been placed on β. In order to find the total flow rate through the impeller, the radial velocity in Equation 2.4 can be integrated around the discharge of the impeller. Doing so gives,

$$Q = b\int_0^{2\pi} \phi\, \Omega\, R_2 \beta(\theta_2)\, d\theta_2 \quad . \tag{2.34}$$

Since the flow rate through the pump is not necessarily steady for a whirling impeller, Q might be considered to be composed of steady and non-steady parts. This may be written as,

$$Q = \bar{Q}\,[1 + \varepsilon^*(q_c \cos \omega t + q_s \sin \omega t)] \quad , \tag{2.35}$$

thereby making,

$$\phi\int_0^{2\pi} \bar{\beta}(\theta_2)\, d\theta_2/2\pi = \bar{Q}/2\pi b\, \Omega\, R_2^2 = \phi \quad , \tag{2.36a}$$

$$\phi\int_0^{2\pi} \beta_c(\theta_2)\, d\theta_2/2\pi = \bar{Q}\, q_c/2\pi b\, \Omega\, R_2^2 = \phi\, q_c \quad , \tag{2.36b}$$

and,

$$\phi\int_0^{2\pi} \beta_s(\theta_2)\, d\theta_2/2\pi = \bar{Q}\, q_s/2\pi b\, \Omega\, R_2^2 = \phi\, q_s \quad . \tag{2.36c}$$

From the first equation it is clear that the mean value of $\bar{\beta}$ is one. Unfortunately, the appropriate mean values of β_c and β_s are not so obvious.

Physically, the flow rate perturbations would come about from the interaction between the centrifugal pump and the piping system to which it is attached. As the impeller orbits about in the volute, the performance characteristics of the pump will change slightly and this will cause the flow rate and the total head rise across the pump to fluctuate. The amount of fluctuation, though, would depend on how the piping system attached to the pump reacts to such perturbations. The significance of the flow rate perturbations is not known at this point. For the time being, the quantities q_c and q_s will be retained as a reminder of the possible influence of the entire hydraulic system.

The final restriction placed on β is that it has at least zeroth

order continuity everywhere. This limitation is based on the physical argument that the flow in the impeller is not capable of the infinite acceleration necessary to maintain a discontinuity. What this means is that β must be continuous around the discharge of the impeller, and in particular that,

$$\beta(R_2,0) = \beta(R_2,2\pi) \quad , \tag{2.37}$$

even though the pressure may be discontinuous at the tongue.

2.4.2. Matching Conditions Across the Volute Tongue

At the tongue of the volute, the cross sectional area distribution is discontinuous and this is likely to cause a discontinuity in the pressure and velocity distributions. In order to deal with this, it is assumed that the total head of the recirculated flow remains constant from one side of the tongue to the other. This may be stated as,

$$\int_{R_2'}^{R_3'(0)} (P_v + \rho V_\theta^2,/2)\Big|_{\theta'=2\pi} wdr' = \int_{R_2'}^{R_3'(0)} (P_v + \rho V_\theta^2,/2)\Big|_{\theta'=0} wdr' \quad , \tag{2.38}$$

or, when non-dimensionalized and separated into harmonics Equation 2.38 becomes,

$$[\overline{D_p}(2\pi) - \overline{D_p}(0)]\bar{A}(0) + [\bar{V}^2(2\pi) - \bar{V}^2(0)][\bar{A}(0) + 2\,\overline{\ln r A}(0)] = 0 \quad , \tag{2.39a}$$

$$[D_{pc}(2\pi) - D_{pc}(0)]\bar{A}(0) - [\overline{D_p}(2\pi) - \overline{D_p}(0)]W_i^* \tag{2.39b}$$

$$+2\,[\bar{V}(2\pi)V_c(2\pi) - \bar{V}(0)V_c(0)][\bar{A}(0) + 2\,\overline{\ln r A}(0)]$$

$$- [\bar{V}^2(2\pi) - \bar{V}^2(0)][W_i^* + 2\bar{A}(0)] = 0 \quad ,$$

and

$$[D_{ps}(2\pi) - D_{ps}(0)]\bar{A}(0)$$

$$+ 2[\bar{V}(2\pi)V_s(2\pi) - \bar{V}(0)V_s(0)][\bar{A}(0) + 2\,\overline{\ln rA}(0)] = 0 \quad . \qquad (2.39c)$$

These three equations may be further simplified by implementing the continuity equation developed in the volute model. Integrating the continuity equation of Expressions 2.30a, 2.30b, and 2.30c from 0 to 2π gives,

$$\bar{V}(2\pi)\bar{A}(2\pi) = \bar{V}(0)\bar{A}(0) + 2\pi\phi \quad , \qquad (2.40a)$$

$$V_c(2\pi)\bar{A}(2\pi) = V_c(0)\bar{A}(0) + W_i^*[\bar{V}(2\pi) - \bar{V}(0)] + 2\pi\phi q_c \quad , \qquad (2.40b)$$

and,

$$V_s(2\pi)\bar{A}(2\pi) = V_s(0)\bar{A}(0) + 2\pi\phi q_s \quad . \qquad (2.40c)$$

Combining these three relations with those given by matching the total head at the tongue yields three expressions for the initial volute flow velocity at the tongue. These three expressions are :

steady centered :

$$\bar{V}(0) = \frac{2\pi\phi a/\bar{A}(2\pi) + \sqrt{[2\pi\phi/\bar{A}(2\pi)]^2 + [1 - a^2][\overline{D_p}(2\pi) - \overline{D_p}(0)]/c}}{1 - a^2} \qquad (2.41a)$$

whirling cos ωt :

$$V_c(0) = \frac{\left[\begin{array}{l} -\bar{V}(2\pi)[W_i^*(\bar{V}(2\pi) - \bar{V}(0)) + 2\pi\phi q_c]/\bar{A}(2\pi) \\ \\ + \frac{1}{2c}\left[\begin{array}{l} \{\bar{V}^2(2\pi) - \bar{V}^2(0)\}\{2 + W_i^*/\bar{A}(0)\} \\ \\ -\{D_{pc}(2\pi) - D_{pc}(0)\} + W_i^*\{\overline{D_p}(2\pi) - \overline{D_p}(0)\}/\bar{A}(0) \end{array}\right] \end{array}\right]}{\bar{A}(0)[\bar{V}(2\pi)/\bar{A}(2\pi) - \bar{V}(0)/\bar{A}(0)]} \qquad (2.41b)$$

whirling sin ωt :

$$V_s(0) = -\frac{[\{D_{ps}(2\pi) - D_{ps}(0)\}/2c + 2\pi\phi q_s\bar{V}(2\pi)/\bar{A}(2\pi)]}{\bar{A}(0)[\bar{V}(2\pi)/\bar{A}(2\pi) - \bar{V}(0)/\bar{A}(0)]} \qquad (2.41c)$$

In these three expressions,

$$a = \bar{A}(0)/\bar{A}(2\pi) \quad \text{and} \quad c = 1 + 2\,\overline{\ln r}\bar{A}(0)/\bar{A}(0) \quad .$$

Of course, matching the total head across the tongue is not the only option possible. Matching velocities or the pressures from one side of the tongue to the other might also be considered appropriate, as would several other more intricate solutions. The consequences of some of the choices available will be mentioned later in Section 5.6.

2.4.3. Determination of the Flow Path Angle

Finally, the flow path angle, γ, must be found in order to complete the solution of Equations 2.19, 2.30, and 2.32 . In the derivation of the impeller model this angle was assumed to be a function of only the flow coefficient, ϕ, and the total head rise across the pump, $\bar{\psi}$. This statement can also be interpreted to mean that once ϕ and $\bar{\psi}$ are chosen then γ may be calculated using the model. For the theoretical model, the

total head rise is defined as,

$$\psi = \int_{R_3(0)}^{R_3(2\pi)} [P_v^*(2\pi) + V^{*2}(2\pi)]wdr/\{2[\bar{A}(2\pi) - \bar{A}(0)]\} \qquad (2.42)$$

Usually the relationship between ϕ and ψ is known through experimental results presented in the performance curves for a given pump. So an iterative procedure is adopted to find the appropriate value of γ for which the theoretical total head rise matches the experimental value, or,

$$\psi_{exp} = \bar{\psi} = [\overline{D_p}(2\pi) + C_v\bar{V}^2(2\pi)]/2 \quad , \qquad (2.43a)$$

where

$$C_v = 1 + 2[\overline{\ln rA}(2\pi) - \overline{\ln rA}(0)]/[\bar{A}(2\pi) - \bar{A}(0)] \quad .$$

Once the flow path angle is found, it is assumed not to change for small eccentric displacements of the impeller. The total head rise across the pump, however, does change and the in-phase and quadrature components of this change are found from Equation 2.42 to be,

$$\psi_c = [D_{pc}(2\pi) + 2C_v\bar{V}(2\pi)V_c(2\pi) - 2\bar{V}^2(2\pi)]/2 \quad , \qquad (2.43b)$$

and

$$\psi_s = [D_{ps}(2\pi) + 2C_v\bar{V}(2\pi)V_s(2\pi)]/2 \quad . \qquad (2.43c)$$

This information will be needed in finding q_c and q_s, once it is known how the piping connected to the pump responds to fluctuations in the flowrate.

2.4.4. Additional Restrictions

All of the restrictions listed in Equations 2.36, 2.37, 2.41 and 2.43 are necessary for finding a unique solution to the theoretical model. There is one additional equation which is actually redundant, but it will make solving Equations 2.19, 2.30, and 2.32 much simpler. In the impeller model a restriction is placed on D_p by Equation 2.19 that must be met by D_p in Equation 2.32 . This restriction is found by integrating the three expressions of Equation 2.19 around the discharge of the impeller to give,

$$\int_0^{2\pi} (\phi^2 \sec^2\gamma\, \bar{\beta}^2 + \overline{D_p})\, d\theta_2/2\pi = 1 \quad , \tag{2.44a}$$

$$\int_0^{2\pi} \{2\phi^2 \sec^2\gamma\, \bar{\beta}\beta_c + D_{pc} + \cos\theta\, \overline{D_p}$$

$$+ 2\,\frac{\omega}{\Omega}\,\phi\, R\,\bar{\beta}\sin(\theta + \tan\gamma \ln(R))\}\, d\theta/2\pi$$

$$= -\,2\,\frac{\omega}{\Omega}\,\phi\, q_s \sec^2\gamma \ln(R) \quad , \tag{2.44b}$$

and,

$$\int_0^{2\pi} \{2\phi^2 \sec^2\gamma\, \bar{\beta}\beta_s + D_{ps} + \sin\theta\, \overline{D_p}$$

$$- 2\,\frac{\omega}{\Omega}\,\phi\, R\,\bar{\beta}\cos(\theta + \tan\gamma \ln(R))\}\, d\theta/2\pi$$

$$= \{\overline{D_p}(0) - \overline{D_p}(2\pi)\}/2\pi + 2\,\frac{\omega}{\Omega}\,\phi\, q_c \sec^2\gamma \ln(R) \tag{2.44c}$$

2.5 Hydrodynamic Forces on the Impeller

There are two contributions to the forces on the impeller which will be considered. One deals with the momentum exchange between the impeller and the fluid, and the other concerns the pressure acting at the impeller inlet and discharge.

In Appendix A an expression for the net momentum flux contribution to the force is developed for an impeller of constant blade passage width, that rotates and whirls at constant speeds. Referring back to the geometry of Figure 2.1, the contribution of the momentum flux to the force acting on the impeller is given in complex notation as,

$$\frac{\underset{\sim}{F}_m}{\rho b} = \frac{(F_x + jF_y)_m}{\rho b} = -e^{j\Omega t}\frac{\partial}{\partial t}\int_0^{2\pi}\int_{R_1}^{R_2}(v_r'' + jv_\theta'')e^{j\theta''}r''dr''d\theta''$$

$$- e^{j\Omega t}\left[\int_0^{2\pi}(v_r'' + jv_\theta'')v_r''e^{j\theta''}r''d\theta''\right]\Bigg|_{R_1}^{R_2}$$

$$- e^{j\Omega t}2\Omega\int_0^{2\pi}\int_{R_1}^{R_2}(jv_r'' - v_\theta'')e^{j\theta''}r''dr''d\theta''$$

$$+ \omega^2\varepsilon\pi(R_2^2 - R_1^2)e^{j\omega t} \quad . \qquad (2.45)$$

This equation can be written in terms of β and γ by using the velocity profiles described by Equations 2.2, 2.4, 2.6, and 2.10, and then divided into three parts for the steady, in-phase, and quadrature force components. The resulting expressions for the momentum flux force on the impeller are as follows:

steady centered :

$$\underset{\sim}{\bar{F}}_m = -\phi^2(1 - j\tan\gamma - \underset{\sim}{k}R)\int_0^{2\pi}\bar{\beta}^2(\theta_2)e^{j\theta_2}d\theta_2/\pi$$

$$- j\phi\int_0^{2\pi}\bar{\beta}(\theta_2)e^{j\theta_2}d\theta_2/\pi \quad , \qquad (2.46a)$$

whirling cos ωt :

$$\underset{\sim}{F}_{mc} = -2\phi^2(1 - j\tan\gamma - \underset{\sim}{k}R)\int_0^{2\pi}\bar{\beta}(\theta_2)\beta_c(\theta_2)e^{j\theta_2}d\theta_2/\pi$$

(continued)

$$- j\phi\int_0^{2\pi} \beta_c(\theta_2) e^{j\theta_2} d\theta_2/\pi + \frac{\omega^2}{\Omega^2}(1 - 1/R^2)$$

$$- \frac{\omega}{\Omega}\,\phi(1 - \underset{\sim}{k}/R)\int_0^{2\pi} \beta_s(\theta_2) e^{j\theta_2} d\theta_2/\pi$$

$$- \frac{\omega}{\Omega}\,\phi j\underset{\sim}{k}\int_0^{2\pi} \bar{\beta}(\theta_2)\cos(\theta_2 + \tan\gamma\,\ln(R)) e^{j\theta_2} d\theta_2/\pi \quad , \qquad (2.46b)$$

whirling $\sin\omega t$:

$$\underset{\sim}{F}_{ms} = -2\phi^2(1 - j\tan\gamma - \underset{\sim}{k}\,R)\int_0^{2\pi} \bar{\beta}(\theta_2)\beta_s(\theta_2) e^{j\theta_2} d\theta_2/\pi$$

$$- j\phi\int_0^{2\pi} \beta_s(\theta_2) e^{j\theta_2} d\theta_2/\pi + j\frac{\omega^2}{\Omega^2}(1 - 1/R^2)$$

$$+ \frac{\omega}{\Omega}\,\phi(1 - \underset{\sim}{k}/R)\int_0^{2\pi} \beta_c(\theta_2) e^{j\theta_2} d\theta_2/\pi$$

$$- \frac{\omega}{\Omega}\,\phi\, j\,\underset{\sim}{k}\int_0^{2\pi} \bar{\beta}(\theta_2)\sin(\theta_2 + \tan\gamma\,\ln(R)) e^{j\theta_2} d\theta_2/\pi \quad , \qquad (2.46c)$$

where, $\underset{\sim}{k} = \cos(\tan\gamma\,\ln(R)) + j\sin(\tan\gamma\,\ln(R))$.

The contribution to the impeller force made by the pressure is found by integrating the pressure distributions around the inlet and exit of the impeller. In terms of the previously defined geometry, the pressure force acting on the impeller is,

$$\underset{\sim}{F}_p = (F_x + jF_y)_p = b\int_0^{2\pi} P_i(R_1,\theta_1) R_1 e^{j\theta_1} d\theta_1$$

$$- W_i\int_0^{2\pi} P_i(R_2,\theta_2) R_2 e^{j\theta_2} d\theta_2 \quad . \qquad (2.47)$$

The entire exit width of the impeller, W_i, is used because the pressure was considered continuous across the width at the volute inlet. The indicated integrations may be performed using the pressure distributions

given in Equations 2.11 and 2.12 . The resulting contribution of the pressure to the force acting on the impeller is divided into the steady, in-phase, and quadrature components to give the following expressions.

steady centered :

$$\bar{\underset{\sim}{F}}_p = \phi^2[W_i^* \sec^2\gamma - \underset{\sim}{k} R]\int_0^{2\pi} \bar{\beta}^2(\theta_2) e^{j\theta_2} d\theta_2/2\pi$$

$$- jW_i^* \phi \sec^2\gamma \ln(R)\int_0^{2\pi} \bar{\beta}(\theta_2) e^{j\theta_2} d\theta_2/\pi \qquad (2.48a)$$

whirling cos ωt :

$$\underset{\sim}{F}_{pc} = 2\phi^2[W_i^* \sec^2\gamma - \underset{\sim}{k} R]\int_0^{2\pi} \bar{\beta}(\theta_2)\beta_c(\theta_2) e^{j\theta_2} d\theta/2\pi$$

$$- jW_i^* \phi \sec^2\gamma \ln(R)\int_0^{2\pi} \beta_c(\theta_2) e^{j\theta_2} d\theta_2/\pi$$

$$+ \frac{\omega}{\Omega} W_i^* \phi \sec^2\gamma \ln(R)\int_0^{2\pi} \beta_s(\theta_2) e^{j\theta_2} d\theta_2/\pi$$

$$- \frac{\omega}{\Omega} \phi(\underset{\sim}{k} - W_i^* R)\int_0^{2\pi} \bar{\beta}(\theta_2)\sin(\theta_2 + \tan\gamma \ln(R)) e^{j\theta_2} d\theta_2/\pi$$

$$- \frac{\omega}{\Omega} W_i^*/(\underset{\sim}{k} R) - \frac{\omega^2}{\Omega^2} W_i^*[1 - 1/(\underset{\sim}{k} R)]/\tan^2\gamma \quad , \qquad (2.48b)$$

whirling sin ωt :

$$\underset{\sim}{F}_{ps} = 2\phi^2[W_i^* \sec^2\gamma - \underset{\sim}{k} R]\int_0^{2\pi} \bar{\beta}(\theta_2)\beta_s(\theta_2) e^{j\theta_2} d\theta_2/2\pi$$

$$- jW_i^* \phi \sec^2\gamma \ln(R)\int_0^{2\pi} \beta_s(\theta_2) e^{j\theta_2} d\theta_2/\pi$$

$$- \frac{\omega}{\Omega} W_i^* \phi \sec^2\gamma \ln(R)\int_0^{2\pi} \beta_c(\theta_2) e^{j\theta_2} d\theta_2/\pi$$

(continued)

$$+ \frac{\omega}{\Omega}\,\phi(\underset{\sim}{k} - W_i^* R)\int_0^{2\pi} \bar{\beta}(\theta_2)\cos(\theta_2 + \tan\gamma\,\ln(R))e^{j\theta_2}d\theta_2/\pi$$

$$- \frac{\omega}{\Omega}\,j\,W_i^*/(\underset{\sim}{k}\,R) - \frac{\omega^2}{\Omega^2}W_i^*[1 - 1/(\underset{\sim}{k}\,R)]/\tan^2\gamma \quad , \qquad (2.48c)$$

In order to find the total force acting on the impeller the force contributions of the momentum flux and the pressure are added together. The resulting total force is given by,

$$\underset{\sim}{F}^* = \underset{\sim}{F}_p^* + \underset{\sim}{F}_m^* = \bar{\underset{\sim}{F}} + \varepsilon^*(\underset{\sim}{F}_c \cos\omega t + \underset{\sim}{F}_s \sin\omega t) \quad , \qquad (2.49)$$

where,

$$\bar{\underset{\sim}{F}} = \phi^2[W_i^*\sec^2\gamma + \underset{\sim}{k}\,R - 2 + 2j\tan\gamma]\int_0^{2\pi} \bar{\beta}^2(\theta_2)e^{j\theta_2}d\theta/2\pi$$

$$- j\phi[W_i^*\sec^2\gamma\,\ln(R) + 1]\int_0^{2\pi} \bar{\beta}(\theta_2)e^{j\theta_2}d\theta_2/\pi \quad , \qquad (2.50a)$$

$$\underset{\sim}{F}_c = \phi^2[W_i^*\sec^2\gamma + \underset{\sim}{k}\,R - 2 + 2j\tan\gamma]\int_0^{2\pi} \bar{\beta}(\theta_2)\beta_c(\theta_2)e^{j\theta_2}d\theta_2/\pi$$

$$- j\phi[W_i^*\sec^2\gamma\,\ln(R) + 1]\int_0^{2\pi} \beta_c(\theta_2)e^{j\theta_2}d\theta_2/\pi$$

$$+ \frac{\omega}{\Omega}\,\phi[W_i^*\sec^2\gamma\,\ln(R) + \underset{\sim}{k}/R - 1]\int_0^{2\pi} \beta_s(\theta_2)e^{j\theta_2}d\theta_2/\pi$$

$$+ \frac{\omega}{\Omega}\,[\phi\,R\,W_i^*\int_0^{2\pi} \bar{\beta}(\theta_2)\sin(\theta_2 + \tan\gamma\,\ln(R))e^{j\theta_2}d\theta_2/\pi]$$

$$- \frac{\omega}{\Omega}[2j\phi + W_i^*/(\underset{\sim}{k}\,R)]$$

$$- \frac{\omega^2}{\Omega^2}\{W_i^*[1 - 1/(\underset{\sim}{k}\,R)]/\tan^2\gamma - 1 + 1/R^2\} \quad , \qquad (2.50b)$$

and,

$$\underset{\sim}{F}_s = \phi^2[W_i^* \sec^2\gamma + \underset{\sim}{k}\, R - 2 + 2j \tan\gamma]\int_0^{2\pi} \bar{\beta}(\theta_2)\beta_s(\theta_2)e^{j\theta_2}d\theta_2/\pi$$

$$- j\phi[W_i^* \sec^2\gamma \ln(R) + 1]\int_0^{2\pi} \beta_s(\theta_2)e^{j\theta_2}d\theta_2/\pi$$

$$- \frac{\omega}{\Omega}\phi[W_i^* \sec^2\gamma \ln(R) + \underset{\sim}{k}/R - 1]\int_0^{2\pi} \beta_c(\theta_2)e^{j\theta_2}d\theta_2/\pi$$

$$- \frac{\omega}{\Omega}[\phi R W_i^* \int_0^{2\pi} \bar{\beta}(\theta_2)\cos(\theta_2 + \tan\gamma \ln(R))e^{j\theta_2}d\theta_2/\pi]$$

$$- \frac{\omega}{\Omega} j[2j\phi + W_i^*/(\underset{\sim}{k}\, R)]$$

$$- \frac{\omega^2}{\Omega^2} j\{W_i^*[1 - 1/(\underset{\sim}{k}\, R)]/\tan^2\gamma - 1 + 1/R^2\} \quad , \qquad (2.50c)$$

where $\underset{\sim}{k}$ was defined in Equation 2.46 .

The force equation may also be written in vector form as,

$$\begin{Bmatrix} F_x^* \\ F_y^* \end{Bmatrix} = \begin{Bmatrix} \bar{F}_x \\ \bar{F}_y \end{Bmatrix} + \varepsilon^* \begin{bmatrix} A_{xx}^* & A_{xy}^* \\ A_{yx}^* & A_{yy}^* \end{bmatrix} \begin{Bmatrix} \cos\omega t \\ \sin\omega t \end{Bmatrix}, \qquad (2.51)$$

where the force components are obtained from,

$$\underset{\sim}{\bar{F}} = \bar{F}_x + j\bar{F}_y \;, \quad \underset{\sim}{F}_c = A_{xx}^* + jA_{yx}^* \;, \quad \text{and} \quad \underset{\sim}{F}_s = A_{xy}^* + jA_{yy}^* \;.$$

Matrix $[A^*]$ is referred to in the literature as the generalized hydrodynamic force matrix and it will be written here as $[A^*(\omega/\Omega)]$ to emphasize that it is a function of the ratio between the whirling speed and the shaft speed.

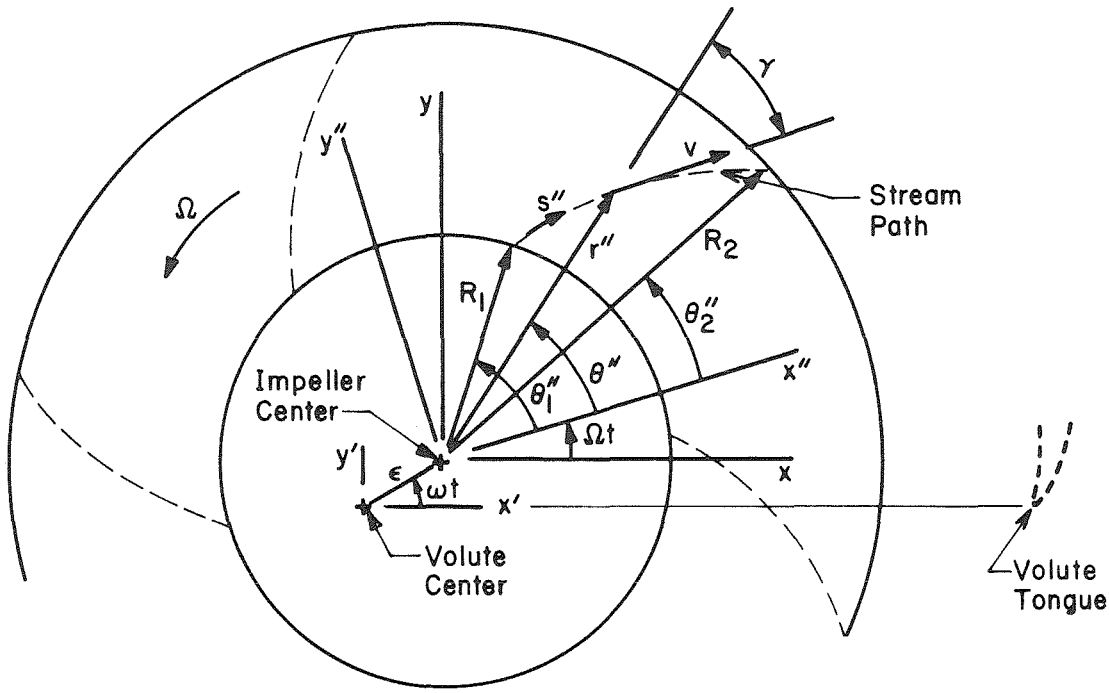

Figure 2.1 Two dimensional representation of the impeller.

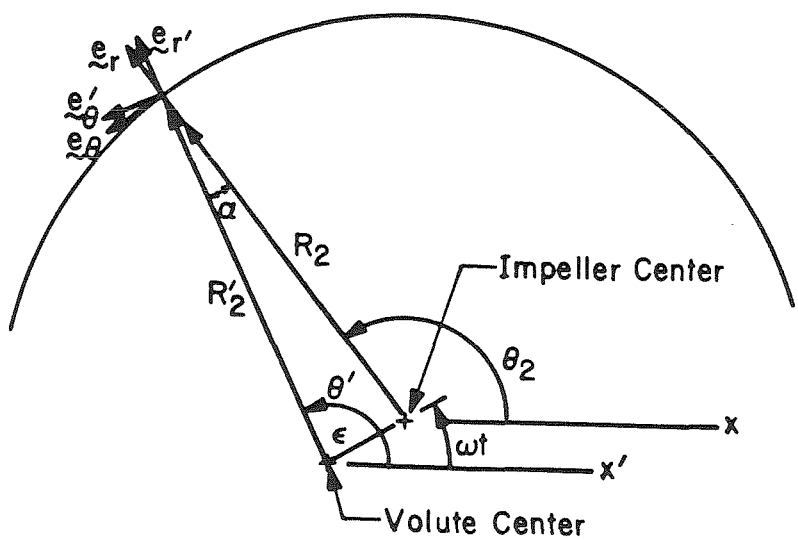

Figure 2.2 Geometric relationships between the impeller and volute centered coordinate systems

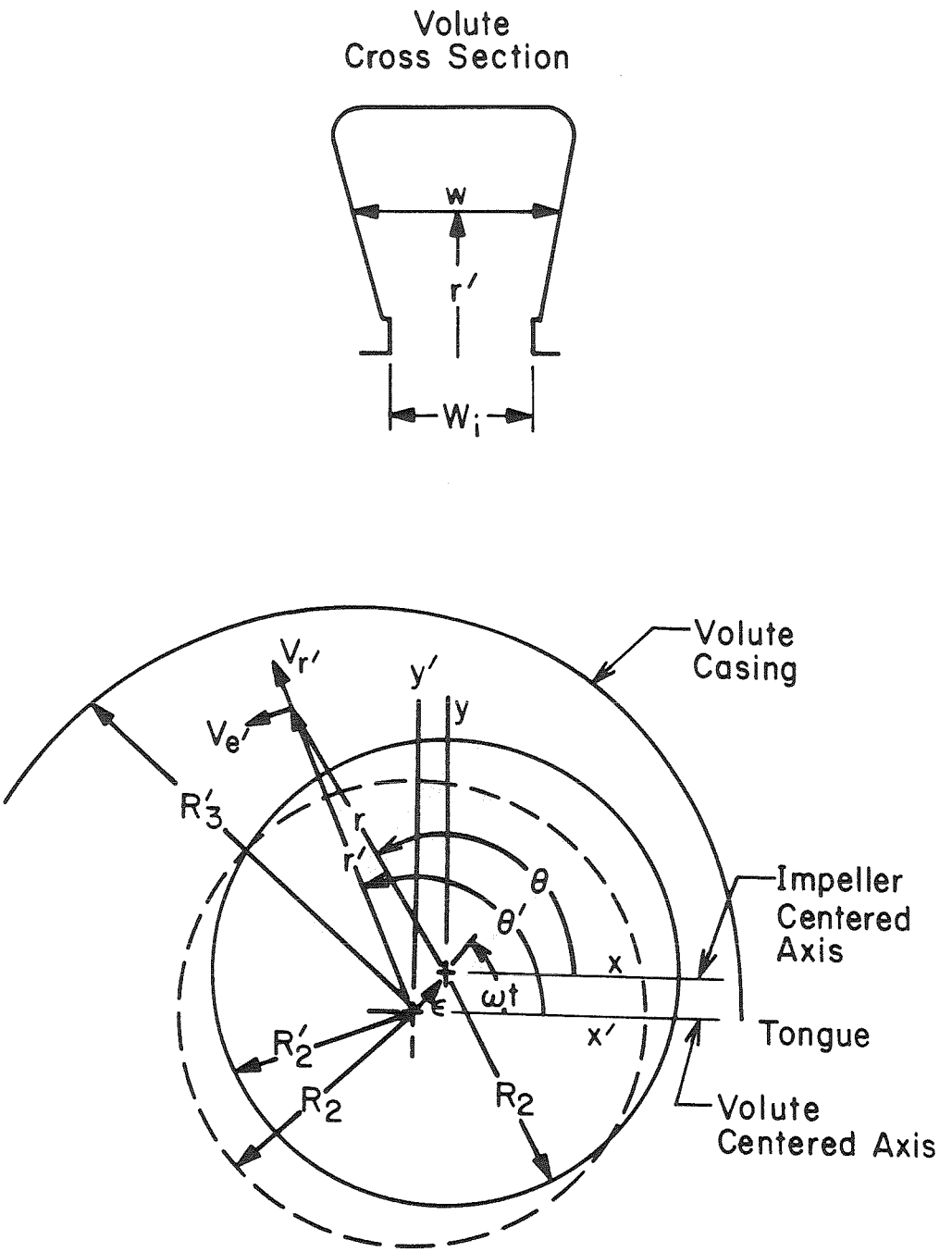

Figure 2.3 Geometry used in the volute model.

CHAPTER 3

RESULTS OF THE THEORETICAL ANALYSIS

3.1 Measurements Required for the Theoretical Analysis

In order to perform the theoretical analysis on a centrifugal pump, the dimensions of the impeller and the volute must be known in advance. The geometry used in this analysis was taken from one of the impellers and two of the volutes available in Caltech's Turbomachinery Lab. This choice allows the theoretical results to be compared in detail to experimental measurements gathered from the Caltech facilities. A full description of the impeller and volutes will be presented in Chapter 4, but the measurements necessary for the theoretical calculations will be described here.

The impeller discharge radius, R_2, and the inlet radius, R_1, must be known, along with the blade discharge width, b, and the width of the impeller at R_2, W_i. The impeller used (referred to as Impeller X) has the following properties:

$$R_2 = 3.19 \text{ inches} , \quad R = R_2 / R_1 = 2.00 ,$$

$$b = 0.62 \text{ inches} , \quad \text{and} \quad W^* = W_i / b = 1.54$$

As for the volute, the integrals of Equation 2.23 must be evaluated and presented as a function of the angle from the tongue, θ'. These integrals were calculated at several angles where the cross sectional geometry of the volute was available from fabrication drawings. Once the integrals were evaluated, the intermediate values were estimated using a quadratic spline fit to interpolate between the measured values. The resulting cross section integrals for the two volutes, A and C, are shown

in Figure 3.1. The circles indicate points where actual measurements of the volute geometry were available.

The cross sectional area of Volute C is only slightly smaller than that of Volute A, and this in turn makes the moments of the cross sectional area smaller. The major difference between the two volutes, though, is that the cross sectional area at the tongue in Volute C is only about half the size of that in Volute A. This by-pass area is of considerable importance in the theoretical model because of the part it plays in the closure conditions at the tongue.

In addition to the pump geometry, the relationship of the total head rise across the pump to the flow rate must also be known for the theoretical analysis to be undertaken. This information is presented in Section 5.1. Figure 5.1 shows the measured performance of Impeller X in Volute A, and Impeller X in Volute C. The mean values for the total head rise are given by the lines in Figure 3.2 and the circles indicate the measured results.

The last bit of information that must be known has more to do with the plumbing of the test facility than with the centrifugal pump being tested. As was indicated in the theoretical analysis, the way in which the entire pumping network responds to fluctuations in the flow rate and total head might prove to be important in calculating the flow perturbations caused in the pump by an eccentrically whirling impeller. The total head perturbations, ψ_c and ψ_s, were included in the pump analysis to account for the response of the pump to the flow rate perturbations, q_c and q_s. What must be known from the test facility, is the magnitude and the phase of the perturbation in the total head losses of the pumping system that would be caused by a perturbation in the flow rate.

It was indicated in the work of Braisted [6] that the present test loop can be represented by dynamic transfer functions for the inlet piping, the discharge piping, and the accumulator (air bag) used for system pressure control. Those transfer functions can be used to evaluate the system response in this situation, but the complexity of estimating such functions for any other system might prove to be a limiting factor in applying the current model. Fortunately, the resistance alone in most realistic pumping systems should prove large enough to make the whirling impeller's effect on the flowrate negligible.

3.2 Preliminary Steps in Obtaining a Solution

Once the impeller and volute information described above is available, the steady parts of the impeller flow perturbation and the volute pressure and velocity distributions can be found by integrating Equations 2.19a, 2.30a, and 2.32a, while meeting the restrictions imposed by Expressions 2.36a, 2.37, 2.41a, and 2.43a. When calculating for the distributions, it is first necessary to solve for the flow path angle, γ. This was done for Impeller X in both volutes A and C and the results are shown in Figure 3.3. The blade angle of Impeller X is 65 degrees and from the theoretical analysis the flow path angle is found to be approximately 82 degrees. From this it can be concluded that the flow is not being perfectly guided through the impeller. This was to be expected though, because Impeller X has only five blades, giving each blade passage a 72 degree arc of flow to turn in less than 2 inches. The consequence of the 82 degree flow path angle is that the velocity entering into the volute has a much lower tangential velocity (in an absolute reference frame) than a perfectly guided flow would have.

As was mentioned earlier in the theoretical analysis, most models

used to predict the direction of the flow at the discharge, consider only the impeller geometry and the flow rate, and neglect the influence of the volute. As shown in Figure 3.3, there are only small differences in the flow path angles (~ 1 degree) between the two volutes. These discrepancies, however, will result in significant changes (~ 10%) in the relative tangential velocity, since it is the tangent of the angles which is used in their determination.

After the flow path angle and the steady distributions are obtained for a given flow rate, the disturbances caused by the impeller whirling in an eccentric orbit may also be found. The perturbation distributions for the eccentrically positioned impeller are generated by solving both parts b and c of Equations 2.19, 2.30, and 2.32, subject to the restrictions of Expressions 2.36b and c, 2.37, and 2.41b and c. When such calculations were performed, the resulting perturbations in the total head rise, ψ_c and ψ_s, were found to have a maximum of about 0.12. This perturbation was used with the system resistance given by Braisted's [6] transfer functions to determine that the flow rate disturbances, q_c and q_s, were less than order ε^2. For this reason it is felt that q_c and q_s can justifiably be set equal to zero.

Further detail on the method used in obtaining a numerical solution may by found in Appendix C.

3.3 Predicted Flow Properties for the Centered Impeller

3.3.1 Pressure Distributions at the Volute Inlet

Figure 3.4 gives the calculated pressure distributions at the inlet of the volute for flow rates both above and below the empirically determined design flow rates of ϕ =0.092 for Volute A and ϕ =0.085 for Volute C (see Section 4.2). It is apparent from this figure that a

discontinuity exists in the pressure distribution from one side of the volute tongue to the other. This might be expected, however, since the cross sectional area is discontinuous at this point and it was the total head that was equated across the tongue in the model. Whether this discontinuity is a pressure drop or a pressure rise depends on whether the pump is being operated below or above the empirically determined design point. For Volute C, the pressure distributions are similar to those that were calculated for Volute A, except that the discontinuities across the tongue are much larger for the off design flow rates. This was anticipated, though, because the discontinuity in the cross sectional area at the tongue is also much larger in Volute C.

At the empirically determined design flow rate for Volute A, a nearly symmetric pressure distribution is observed at the discharge of the impeller. The same result is also true for Volute C. This suggests that volutes with similar geometries would probably be chosen by the past design methods and the current theoretical model.

The phenomena of all pressure distributions passing through a single point (at $\theta' \sim 60°$, for example, in Volute A) should be mentioned at this time but further discussion of this issue will be postponed until Subsection 3.3.4.

3.3.2 Velocity Distributions in the Volute

Along with the pressure distributions at the volute inlet, the velocity distributions within the volute were also calculated for various flowrates, and the results are presented in Figure 3.5. As might have been anticipated from the pressure results, a discontinuity across the tongue also exists in the velocity profile in the volute. The velocity distributions for Volute C are similar to those of Volute A, except that

the flow accelerated immediately after the tongue in Volute A for below design flow coefficients, whereas there was for Volute C only a rapid deceleration in the flow. This is clearly a result of the smaller by-pass area of Volute C restricting the amount of flow re-circulation past the tongue.

There is one problem with the current theoretical model which occurs when calculating the velocity in the volute at the tongue by-pass. At flow rates above design, the velocities at this point decrease to a point where the model becomes no longer viable. The flow was never actually predicted to stagnate, but rather the pressure increase across the tongue grows large enough that the term under the radical of Equation 2.41a becomes negative. Since this problem occurred above the design flowrate, the model is still applicable over the most important range of flowrates and for this reason the question of how to handle the flow reversal problem will not be pursued any further at this point. This problem will be discussed further in Section 5.6 where the alternative solutions that have been tried will be mentioned.

3.3.3 Velocity Distributions in the Impeller

The steady portion of the impeller flow velocity can be determined by combining Equations 2.2, 2.4 and 2.6 to give the radial and tangential velocities relative to the rotating impeller as,

$$\bar{v}_{r''} = \phi\,\bar{\beta}(\theta_2)R_2/r'' \quad \text{and} \quad \bar{v}_{\theta''} = -\phi \tan\gamma\,\bar{\beta}(\theta_2)R_2/r'' \quad . \tag{3.1}$$

The impeller flow perturbations, $\beta(\theta_2)$, are presented in Figure 3.6 and the accompanying flow path angles were already given in Figure 3.3.

When interpreting the impeller flow perturbation curves of Figure 3.6, it should be remembered that $\bar{\beta}$ has an average value of one and that

any deviation from this average is the result of the impellers interaction with the volute. It might be tempting to neglect this deviation, because as shown in Figure 3.6, it accounts for only about 5% of the flow at any point of the impeller discharge. In fact, this is what was done by Iversen, Rolling, and Carlson [15] in their pump model, when they assumed that the discharge velocity around the impeller was symmetric. But there are at least two reasons why this assumption may cause problems in the analysis of the pump. The first reason is that this assumption will neglect the cumulative effect that these small perturbations have on the average velocity within the volute. The second reason is that without allowing for this perturbation, it becomes difficult to justify why the asymmetric pressure distribution around the impeller discharge has no effect on the flow through the impeller. So for these two reasons alone it is felt that the perturbation in the impeller flow must be included in any centrifugal pump model.

It should be pointed out that it is the gradient of the flow perturbation and not the magnitude that is the major cause of the asymmetric pressure distribution on the impeller. This point can be established by examining Equation 2.19a and realizing that the coefficient in front of the $\bar{\beta}$ term is ϕ times the coefficient of the gradient of $\bar{\beta}$, where ϕ is usually much less than one. The gradient of $\bar{\beta}$ originates from the unsteady part of Bernoulli's Equation and is the result of the perturbation being stationary in the volute reference frame, but appearing as an unsteady distribution to the rotating impeller. The gradient of $\bar{\beta}$ tends to be largest around the constricted area of the volute immediately following the tongue, and is even seen to be discontinuous at the tongue itself for the off design flowrates.

3.3.4 Comments on the Property Distributions for the Centered Impeller

One of the original attempts to model the volute flow in this research was to assume that the average total head rise around the volute was a constant that depended only on the overall flow rate. As a matter of interest, the total head distributions around the volute generated by current model are presented in Figure 3.7. The total head increases in the radial direction, so in order to find a mean value, it was averaged over the volute cross section as,

$$\bar{h}_v(\theta') - h_1^* = \int_{R_2}^{R_3} \{\bar{D}_p(\theta') + \bar{V}^2(\theta')[1 + 2\ln(r'/R_2)]\}wdr'/\bar{A}(\theta') \quad ,$$

or,

$$\bar{h}_v(\theta') - h_1^* = \bar{D}_p(\theta') + C(\theta')\bar{V}^2(\theta') \quad , \tag{3.2}$$

where,

$$C(\theta') = 1 + 2\overline{\ln r}A(\theta')/\bar{A}(\theta') \quad .$$

Since the velocity is assumed to be constant over the volute cross section, this can also be considered to be the mass flow averaged total head rise. It might be noticed in Figure 3.7 that the total head is discontinuous at the tongue, while in the model it was assumed that the total head was constant across the tongue. This contradiction can be clarified by recalling from Equation 2.38 that the total head was matched across the tongue only for the recirculated portion of the flow. The remaining discharged portion was not included in the matching condition and this is what causes the apparent total head discontinuity.

Figure 3.7 shows that the average total head does vary with θ', but to a much lesser extent than either the pressure or velocity distributions. It is hoped that this might provide a clue as to why the volute pressure curves presented in Figure 3.5 tend to all pass through a single point. This same feature also occurs in the velocity profiles of Figure 3.6, although the particular point that is passed through is different. A complete physical description of why this happens would, by necessity, end up being as complicated as the model, but a couple of simple oberservations can be made about the consequences of this phenomena. First, all of the velocity distributions in the volute passing through a single point, θ_v, would require that the total flow rate at θ_v was independent of the overall flow through the pump. From the continuity equation for the volute, this would require θ_v to be given by,

$$(\phi_o - \phi_D)\theta_v = -\phi_o \int_0^{\theta_v'} (\bar{\beta}_o - 1)d\theta' + \bar{A}(\theta)[\bar{V}_o(\theta) - \bar{V}_D(\theta)] \quad , \qquad (3.3)$$

where the subscripts D and o designate properties at design and off design points respectively. Second, while the pressure distribution curves do not intersect each other at θ_v, they do appear to cross at a point where the total head curves of Figure 3.7 have either a minimum or maximum.

The one reason for mentioning that all the pressure distributions have a particular point in common, is that this observation eliminates the need to know the complete pump performance curve before applying the model. If it is known in advance that the volute inlet pressure distribution passes through a single value at a single point, independent of the flow rate, then this information could be used to find γ, rather than the total head rise across the pump. In essence, this means that

the model could be used to extrapolate the performance data once the total head rise across the pump was known for two different flow rates. Even though this was sucessfully done with the current model, the argument remains rather speculative until experimental pressure distributions are given.

3.4 Whirl Induced Perturbations

In the introduction it was mentioned that in some applications the whirl may be synchronous with the shaft speed and for this reason it would be desirable to calculate the hydrodynamic force matrix up to $\frac{\omega}{\Omega} = 1$. Unfortunately, the model begins to encounter complications in converging to a solution for whirling speeds of much over 15% of the shaft speed. Part of the problems arise because the governing equations become increasingly coupled as the whirling increases, making it difficult to update the guess on β_c and β_s from one iteration to the next. In addition, the discontinuity of the pressure at the tongue also grows with whirling, and causes the gradients of β_c and β_s to change sharply with θ near $\theta = 0$. This of course only adds to the difficulty in updating the approximation and generates some concern that the pressure perturbation caused by increasing whirl speeds can no longer be considered of order ε. Because of these problems the model will be assumed to be applicable only for whirling speeds from -15% to +15% of the shaft speed, where the pressure discontinuities will be less than 20ε times the mean.

The predicted pressure perturbations, D_{pc} and D_{ps}, at the inlet of Volute A are presented in Figure 3.8 for both stationary and whirling impeller situations. The figure indicates that the pressure disturbance caused by the eccentric positioning of the Impeller X will increase with

decreasing flow coefficient. This leads to the conclusion that the hydrodynamic stiffness of the pump will be a function of flow rate just as the forces were predicted to be.

Given in Figure 3.9 are the disturbances in the impeller flow perturbations, β_c and β_s, that correspond to the pressure disturbances given in Figure 3.8. The distributions show that not only do the magnitudes of the disturbances change with the whirl speed, but the phases also change, making it difficult to use lower whirl speed results to predict β_c and β_s at higher speeds.

3.5 Performance Curves and Mixing Losses

Possibly the largest compromise that has been made in this theoretical analysis is that the total head rise across the pump must be known before the model can be applied. A restriction that requires the pump to have been built and tested certainly limits the use of the model as a preliminary design tool, even though the model might greatly extend the usefulness of the test results once they are obtained. To see if a previous impeller model could be used to predict the performance curves in advance of testing, a model developed by Stodola [27] and a potential flow model by Busemann [8] were applied to Impeller X. The results are shown in Figure 3.10, along with the experimental total head coefficient across the entire pump composed of Volute A and Impeller X. The impeller flow models of both Stodola and Busemann give the total head rise across the impeller alone by correcting for the inability of the blades to perfectly guide the flow. They do not take into account the mixing in the volute or the frictional losses in the pump, and these are the reasons that are traditionally used to explain the differences between their results and actual pump performances.

In order to obtain an estimate of the volute mixing losses, the current model was used to calculate the total head rise coefficient across the impeller alone. The total head rise across the impeller can be found by combining the discharge pressure given in Equation 2.12 with the exit velocities of Equation 3.1 to give,

$$\bar{h}_2 - h_1^* = \bar{C}_p + \bar{v}_{r,,}^2 + (1 - \bar{v}_{\theta,,}^2) = 2\{1 - \phi\bar{\beta}\tan\gamma - \sec^2\gamma \ln(R)\frac{d\bar{\beta}}{d\theta}\} \quad . \qquad (3.4)$$

To find the average value of the total head rise, Equation 3.4 is integrated around the impeller discharge and the resulting total head coefficient across the pump is given by,

$$\psi_2 = \int_0^{2\pi} (\bar{h}_2 - h_1)d\theta/4\pi = 1 - \phi\tan\gamma \quad . \qquad (3.5)$$

If the flow path angle were to match the blade angle, the above equation would become Euler's prediction for the total head rise across the pump. But, as has already been demonstrated, the current model predicts that the flow path angle is actually greater than the blade angle, and varies with both the flow rate and the particular volute being used. The total head coefficient found by applying Equation 3.5 to Volute A and Impeller X is shown as a dashed line in Figure 3.10 . By comparing the predicted total head rises shown in this figure it is evident that the previous theories will be of little use in calculating the performance characteristics needed by the current model.

In the current model, it is difficult to distinguish what should be considered a volute loss and what should be considered an impeller loss, because of the influence that the two parts have on each other. However, from the results of the current theory shown in Figure 3.9, it appears that between the exit of the impeller and the exit of the volute, there

is a substantial volute mixing loss at lower flow rates that becomes almost negligible at higher flow rates. Experimental evidence presented by Bowerman and Acosta [5] tends to support these findings, but the results are somewhat contradictory to previous notions. Streeter and Wylie [26] contend that much of the head loss at lower flow rates is due to improper flow alignment at the impeller inlet, and that at higher flow rates a large portion is due to friction in the blade passages.

3.6 Radial Forces on the Centered Impeller

From the asymmetric pressure and velocity distributions that were presented in Section 3.3, it can be anticipated that there will be a net force acting on the impeller. The expressions to determine the momentum and pressure contributions to the forces on the centered impeller are given in Equations 2.46a and 2.48a, respectively, and the combined total force on the impeller is given by 2.50a . Shown in the upper part of Figure 3.11 are the predicted x,y components of the total hydrodynamic force acting on Impeller X when it is used with Volute A, and in the lower part of the figure are the resulting force components when Volute C is used. For both volutes, the magnitude of the force tends to go through a minimum near the empirical design point and steadily increase as the pump operates further from the design conditions. It is also noticed that for Volute C the total force on the impeller never goes to zero as it does for Volute A. This is due to the large pressure discontinuities that result from the small tongue by-pass area.

Theoretically it was found that the force on the impeller is almost entirely due to the asymmetric pressure distribution at the impeller discharge. Less than two percent of the force is contributed by the momentum flux terms and the pressure variation at the impeller inlet.

This suggests that a reasonable approximation to the hydrodynamic forces could be calculated from pressures measured at the impeller discharge. The calculation of forces in this manner is supported by the work of Iversen et al. [15], where it was found that forces obtained by measuring bearing reactions were almost identical to those obtained by integrating the pressure distributions around the impeller discharge. This observation, however, is contradictory to the earlier finding of Binder and Knapp [3] that up to twenty five percent of the force on the impeller was caused by the asymmetric momentum flux. In obtaining the momentum force contribution, Binder and Knapp were required to measure the velocity as close as possible to the impeller discharge, and even then, there was no assurance that it was the impeller discharge velocity that was being measured.

3.7 Stiffness Matrices for the Displaced Impeller

Displacing the impeller from the center of the volute in essence creates a new pump with new velocity and pressure distributions. The perturbations in the hydrodynamic forces that occur when the impeller is statically perturbed from the volute center are found by applying Equations 2.50b and c with $\omega = 0$. In rotordynamic analyses, the matrix relating the force perturbations to the displacement is traditionally referred to as the stiffness matrix, and the total force acting on the impeller is written in a simplified version of Equation 2.51 as,

$$\begin{Bmatrix} F_x^* \\ F_y^* \end{Bmatrix} = \begin{Bmatrix} \bar{F}_x \\ \bar{F}_y \end{Bmatrix} - \begin{bmatrix} K_{xx}^* & K_{xy}^* \\ K_{yx}^* & K_{yy}^* \end{bmatrix} \begin{Bmatrix} \varepsilon^* \cos\zeta \\ \varepsilon^* \sin\zeta \end{Bmatrix} , \qquad (3.6)$$

where the stiffness matrix, $[K^*]$, is equal to the $[A^*(\omega/\Omega)]$ matrix of Equation 2.51 when $\omega = 0$. The positive direction of each of the components of Equation 3.6 is indicated in Figure 3.12.

To clarify the implications of the stiffness forces, suppose that the impeller is displaced a small distance ε along the +x axis. If K_{xx} and K_{yx} are both positive, then the impeller is subject to a force εK_{xx} tending to restore it to the original position and εK_{yx} driving it in the -y direction. Likewise, if the impeller is moved ε along the +y axis, then a positive K_{xy} and K_{yy} would produce forces εK_{xy} in the -x direction and a restoring force εK_{yy}. Now if the off diagonal terms had opposite signs, the impeller could be expected to travel in a small orbit unless other forces were present to dissipate the stiffness forces.

The stiffness matrix components for Impeller X in Volute A are given in Figure 3.13 as a function of flow rate, and the similar results are also shown for Impeller X in Volute C. For both volutes the stiffness components are such that the impeller could be caused to orbit. It is also evident from these figures that the stiffness components for y displacements are rather insensitive to changes in the flow rate and are generally smaller than the stiffness components for x impeller displacements. Physically this seems reasonable though, since displacements of the impeller in the x direction are likely to cause larger discontinuities in the pressure across the tongue (and therefore larger perturbations) than impeller displacements in the y direction.

3.8 Effects of Whirling on the Impeller Forces

It has already been demonstrated in the stiffness analysis that the forces necessary to cause the impeller to orbit exist once the impeller is displaced from the volute center. How the impeller proceeds to orbit will depend at least in part on the dynamic elements of the generalized hydrodynamic force matrix, $[A(\omega/\Omega)]$ of Equation 2.51 . The $[A(\omega/\Omega)]$ matrix was calculated for Volute A using a discrete number of whirl speed to shaft speed ratios from -12% and +12% for several different flowrates. The resulting components for the flow coefficients $\phi = 0.06$ and $\phi = 0.10$ are shown as circles in Figure 3.14.

Usually those who work in rotordynamics prefer to write the generalized hydrodynamic force matrix in terms of powers of ω/Ω. For the impeller progressing in a circular orbit, the governing equations take on the more familiar appearance of a mass, stiffness, and damping system. From the A_{xy} results with $\phi = 0.06$ it is apparent that the quadratic form associated with a simple damped oscillator will not appropriately model the [A] matrix. A cubic expression, however, will adequately characterize the [A] matrix elements, with only minor discrepancies from the theoretical predictions. The results for the cubic expansion of the [A] matrix elements are shown in Figure 3.14 as dashed lines. Of course, the temptation to assume that the hydrodynamic force matrix can always be approximated by a cubic equation should be avoided because of the limited range of whirl frequencies that were used in the theoretical model.

Knowing the coefficients of the cubic expansion of [A] will allow the matrix to be written in powers of ω/Ω as,

$$\begin{bmatrix} A_{xx} & A_{xy} \\ A_{yx} & A_{yy} \end{bmatrix} = \tag{3.7}$$

$$\begin{bmatrix} -K_{xx} - \omega C_{xy} + \omega^2 M_{xx} + \omega^3 J_{xy} & -K_{xy} + \omega C_{xx} + \omega^2 M_{xy} - \omega^3 J_{xx} \\ -K_{yx} - \omega C_{yy} + \omega^2 M_{yx} + \omega^3 J_{yy} & -K_{yy} + \omega C_{yx} + \omega^2 M_{yy} - \omega^3 J_{yx} \end{bmatrix}$$

or alternatively, as

$$[A(\omega/\Omega)] \begin{Bmatrix} x \\ y \end{Bmatrix} = -[K] \begin{Bmatrix} x \\ y \end{Bmatrix} - [C] \begin{Bmatrix} \dot{x} \\ \dot{y} \end{Bmatrix} - [M] \begin{Bmatrix} \ddot{x} \\ \ddot{y} \end{Bmatrix} - [J] \begin{Bmatrix} \dddot{x} \\ \dddot{y} \end{Bmatrix} \tag{3.8}$$

where $x = \varepsilon \cos \omega t$ and $y = \varepsilon \sin \omega t$. The [K] matrix has already been discussed as representing the stiffness of the hydrodynamic forces, and similarly the [C] matrix represents the damping and the [M] matrix represents the mass, or inertial components of the hydrodynamic forces. The cubic term of Equation 3.7 would be the result of the time rate of change of acceleration on the hydrodynamic forces. Because the rate of change of acceleration is known as the "jerk" in most other dynamic systems, the elements of the [J] matrix will be referred to as the jerk coefficients.

For Impeller X in Volute A, the variation of the matrix elements of Equation 3.7 with flow rate are presented in Figures 3.15a and b. Just as the off diagonal elements in the stiffness matrix would encourage a whirling motion of the impeller, the diagonal terms of the damping matrix would also encourage whirling when the flow rate drops below $\phi = 0.07$. The off diagonal elements, however, will always oppose any tendency of the orbit to increase in size. The inertial forces will tend to drive the impeller in the direction of displacement over most of the flow range that is shown in Figure 3.15b, but will discourage an orbital motion of the impeller. The jerk coefficients would also act to retard the impeller whirling, but their influence is almost negligible for flow

rates over $\phi = 0.07$.

One surprising observation about the mass matrix is that only a small portion of it can be attributed to the actual mass of the fluid in the blade passages. To estimate the inertial forces that are not due to the flow through the impeller, the centrifugal terms of equations 2.50b and c can be evaluated to give the "mass alone" term as,

$$[MA] = \begin{bmatrix} MD & MC \\ -MC & MD \end{bmatrix} , \tag{3.9}$$

where,

$$MD = -\{W_i^*[1 - \cos(\tan\gamma \ln(R))/R]/\tan^2\gamma - 1 + 1/R^2\} ,$$

and,

$$MC = W_i^* \sin(\tan\gamma \ln(R))/(R \tan^2\gamma) .$$

Even though the [MA] matrix was said to be independent of the flow rate, it does depend on the flow path as demonstrated by the $\tan\gamma$ terms in Equation 3.9. This dependence turns out to be rather insignificant though. Over the range of flow rates investigated with either Volute A or C, the [MA] matrix elements are approximately MD=0.73 and MC=0.0013, which is far less than the [M] matrix elements.

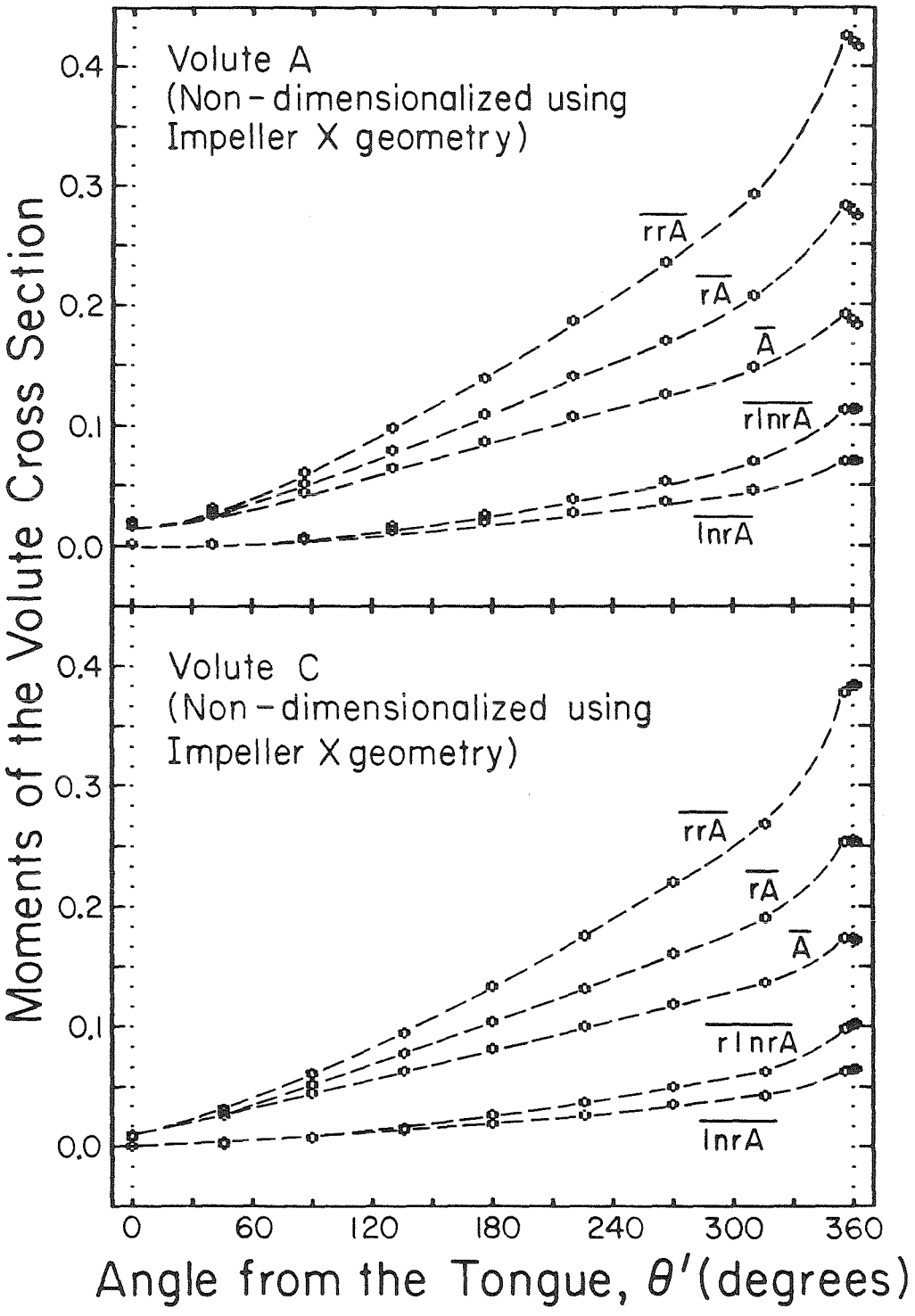

Figure 3.1 Moments of the cross sectional area around Volute A and Volute C (defined in equations 2.23a, b, c, d, and e).

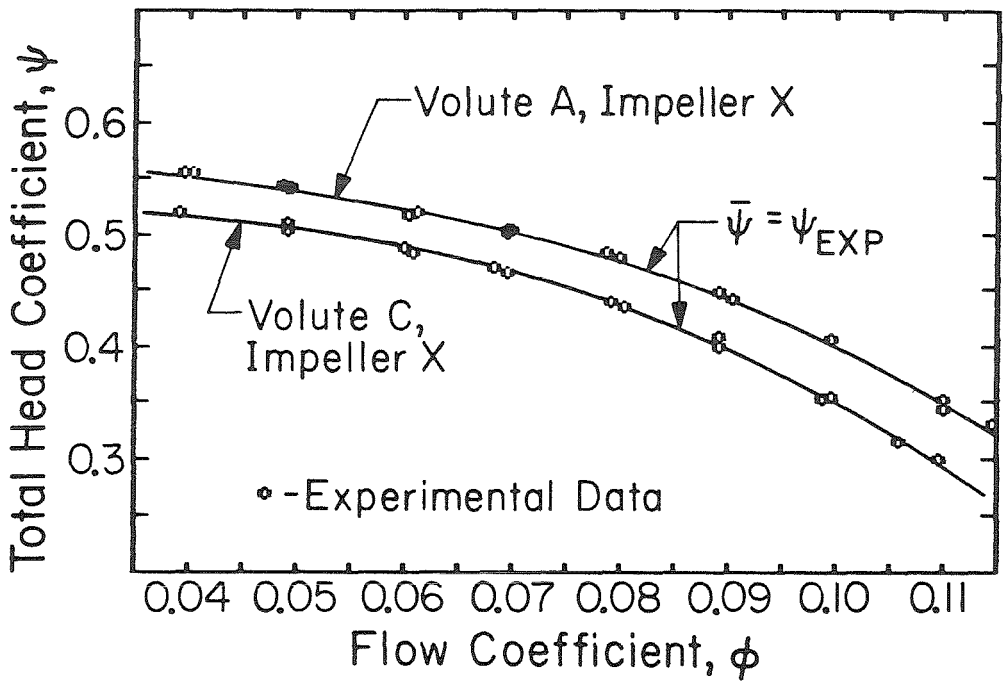

Figure 3.2 Total head rise across the pump as a function of flow coefficient for Impeller X in Volute A and Volute C.

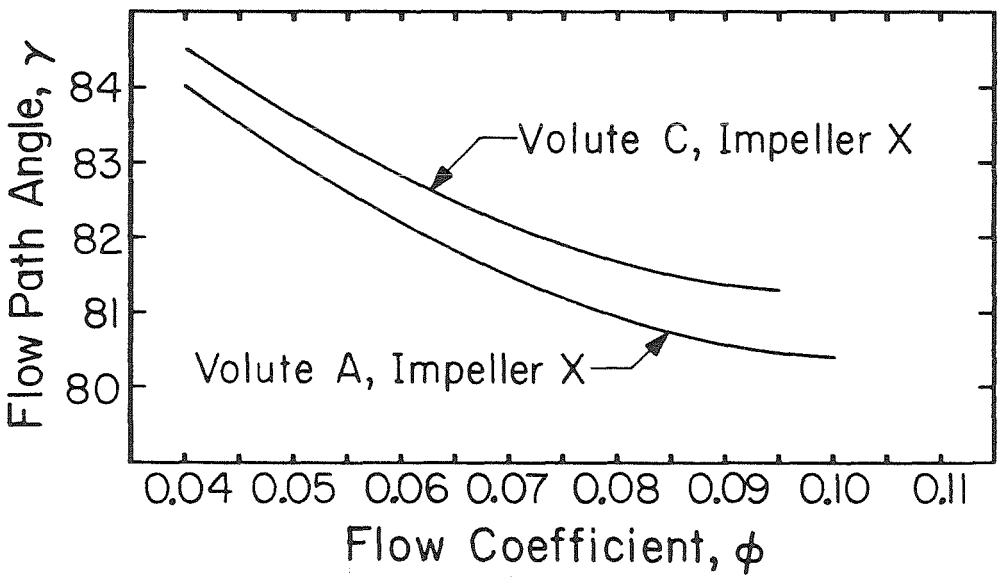

Figure 3.3 Flow path angle as a function of flow coefficient for Impeller X in Volute A and Volute C.

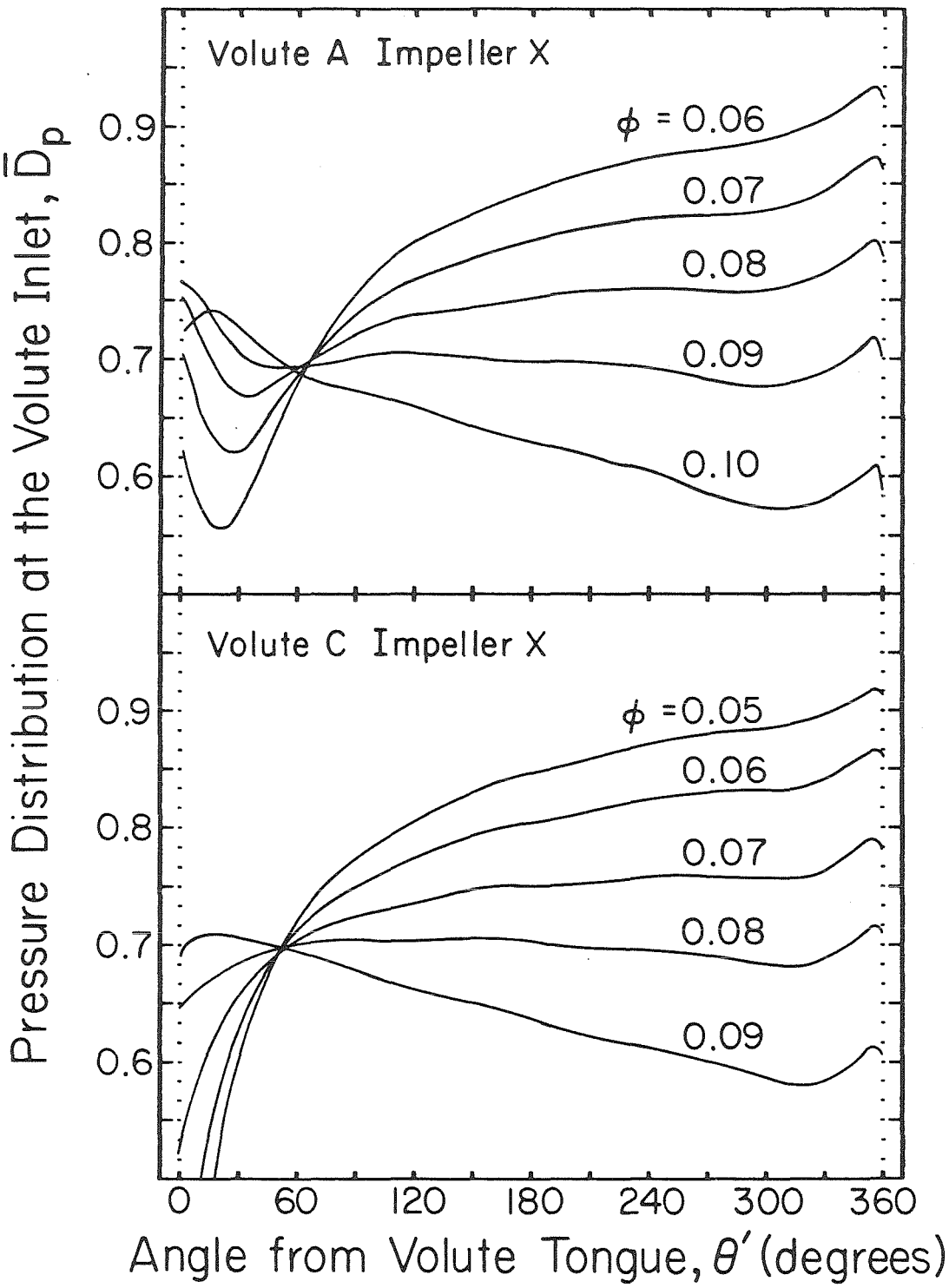

Figure 3.4 Theoretical pressure distributions around the inlet of Volute A and Volute C for various flow coefficients.

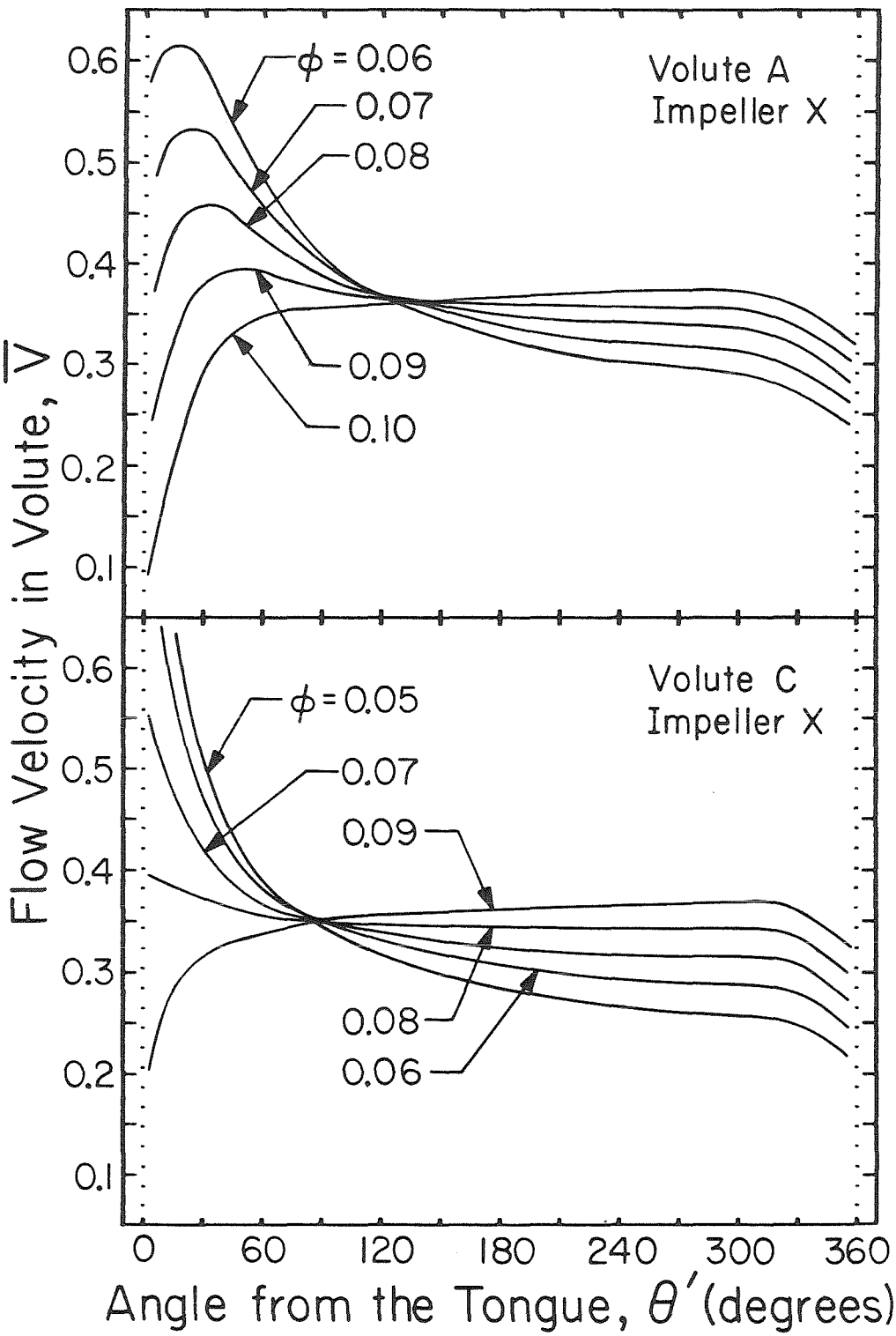

Figure 3.5 Theoretical velocity distributions in Volute A and Volute C for various flow coefficients.

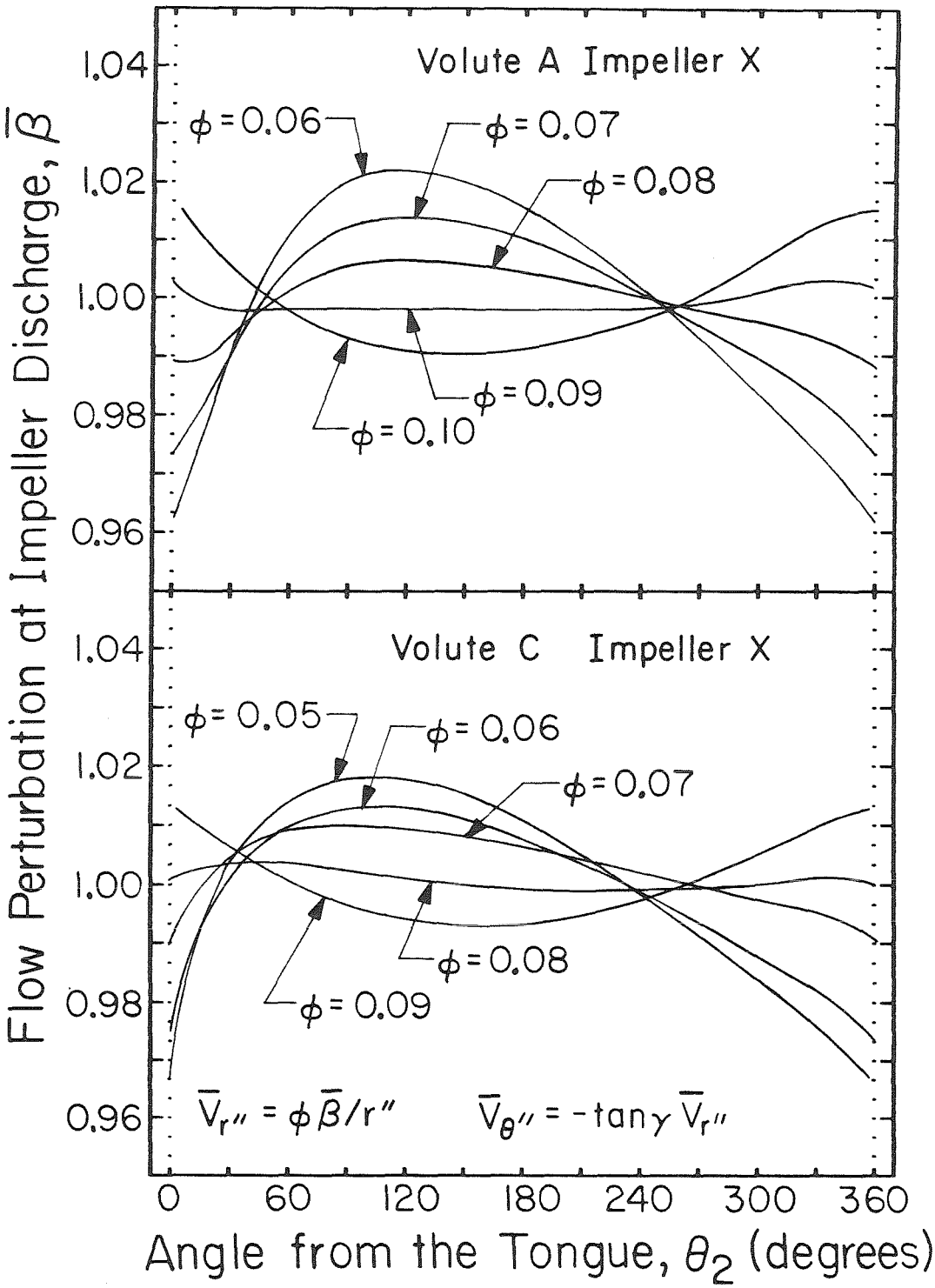

Figure 3.6 Theoretical impeller flow velocity distributions for Impeller X in Volute A and Volute C for various flow coefficients.

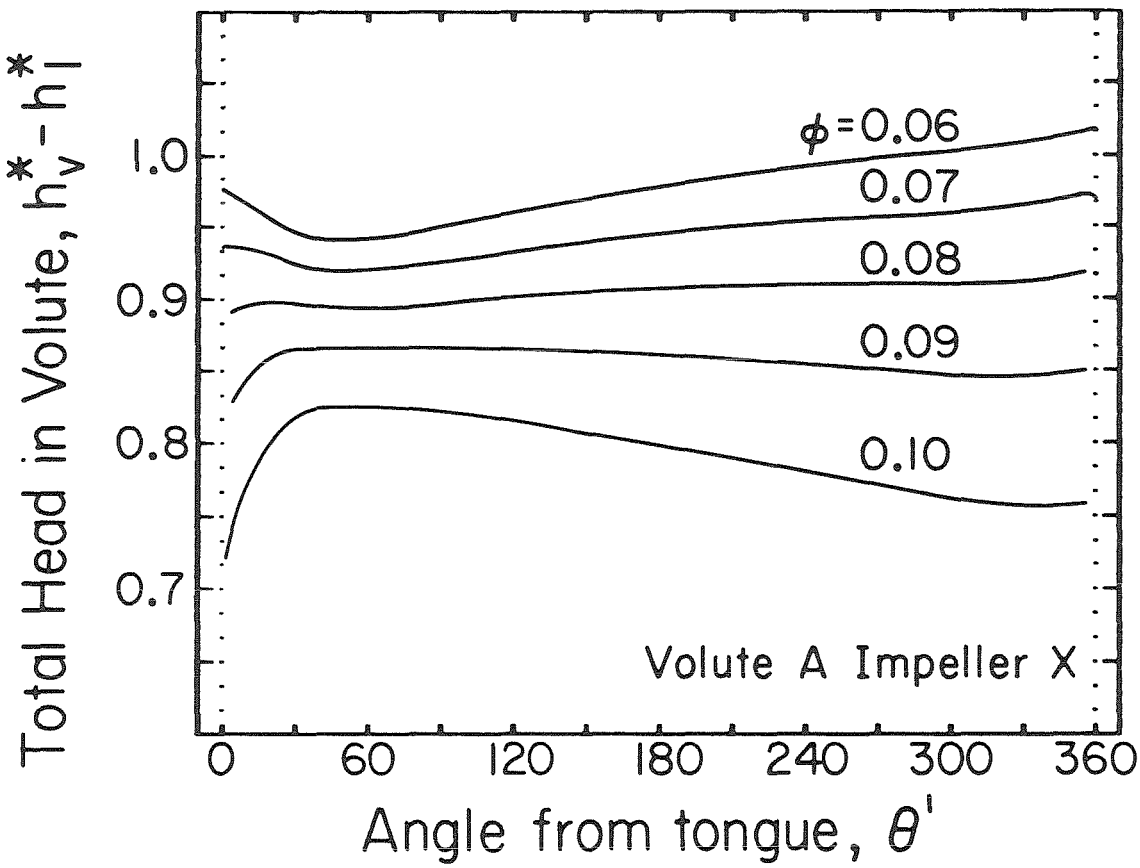

Figure 3.7 Theoretical total head distributions in Volute A for various flow coefficients.

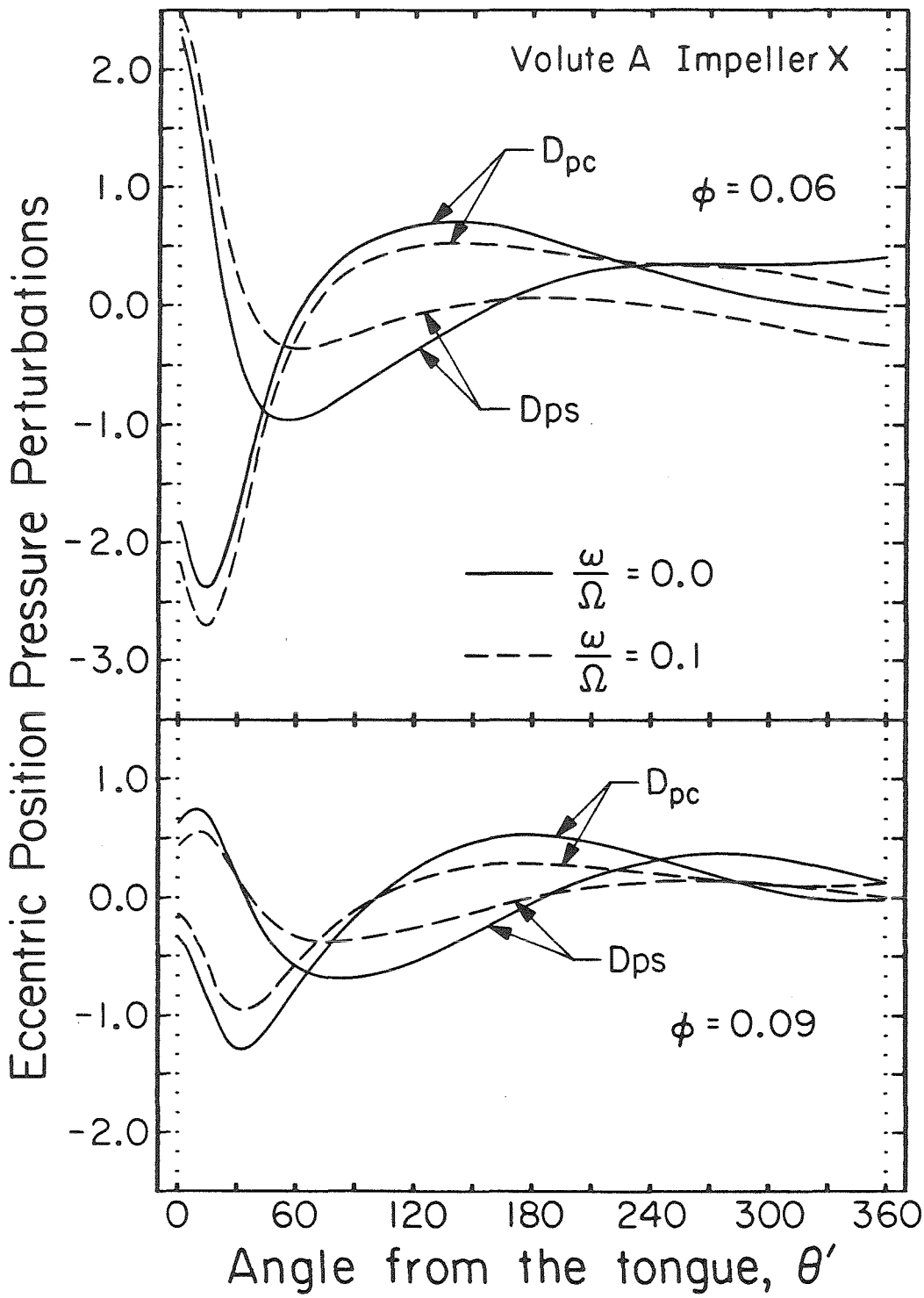

Figure 3.8 Pressure perturbations caused by Impeller X whirling in Volute A.

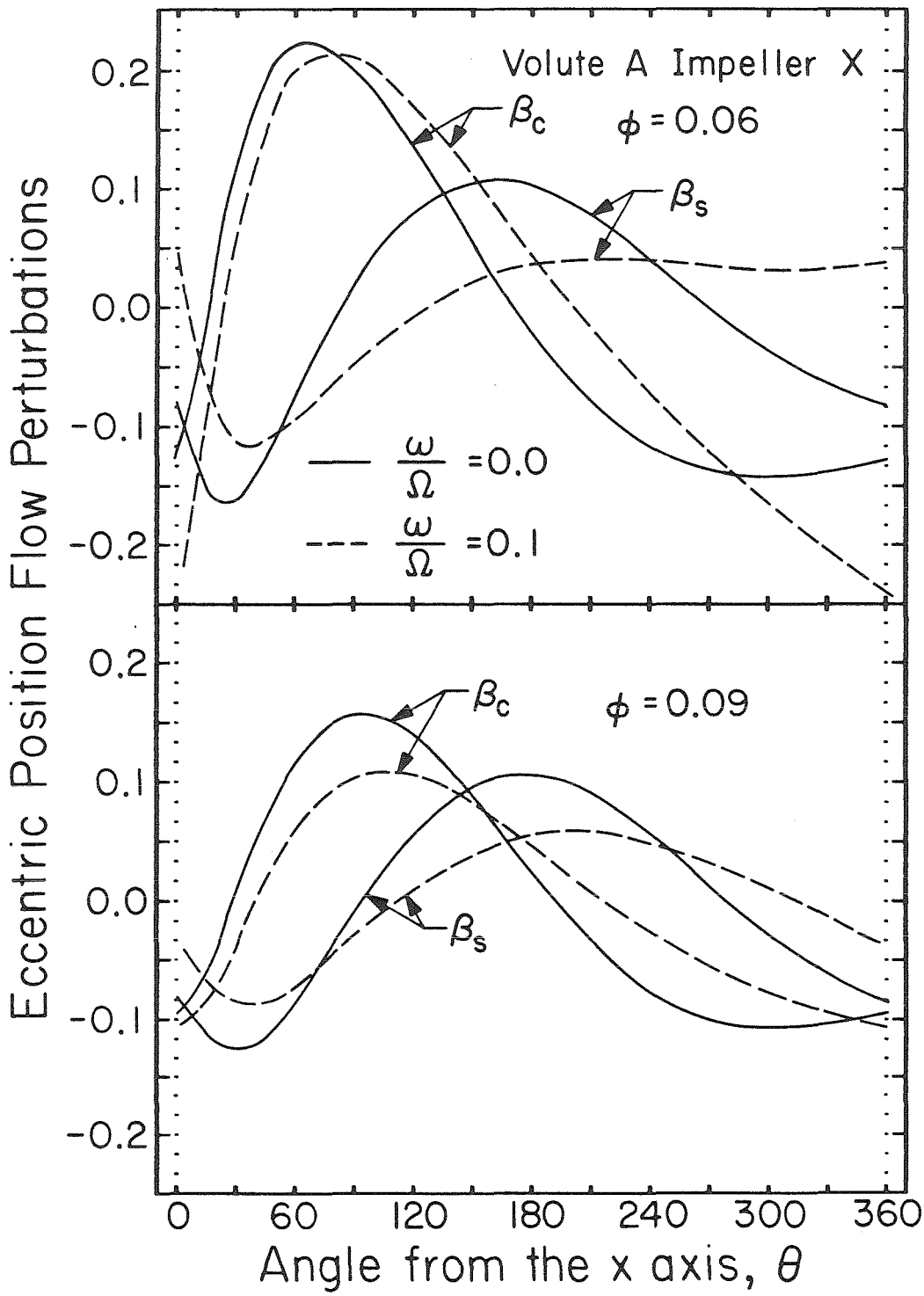

Figure 3.9 Flow perturbations in the impeller caused by Impeller X whirling in Volute A.

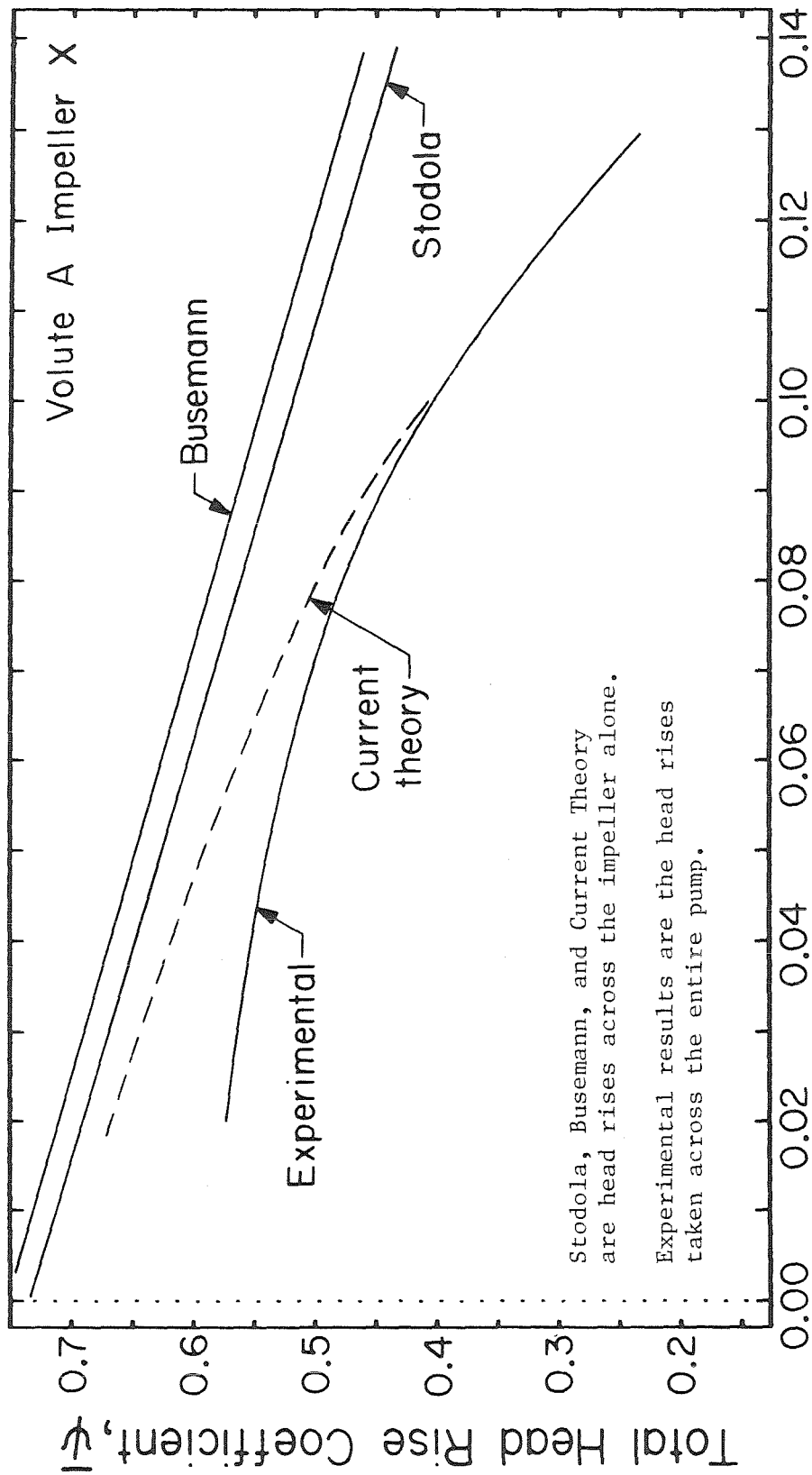

Figure 3.10 Comparison of different models used to predict the total head rise across a pump as a function of flow rate.

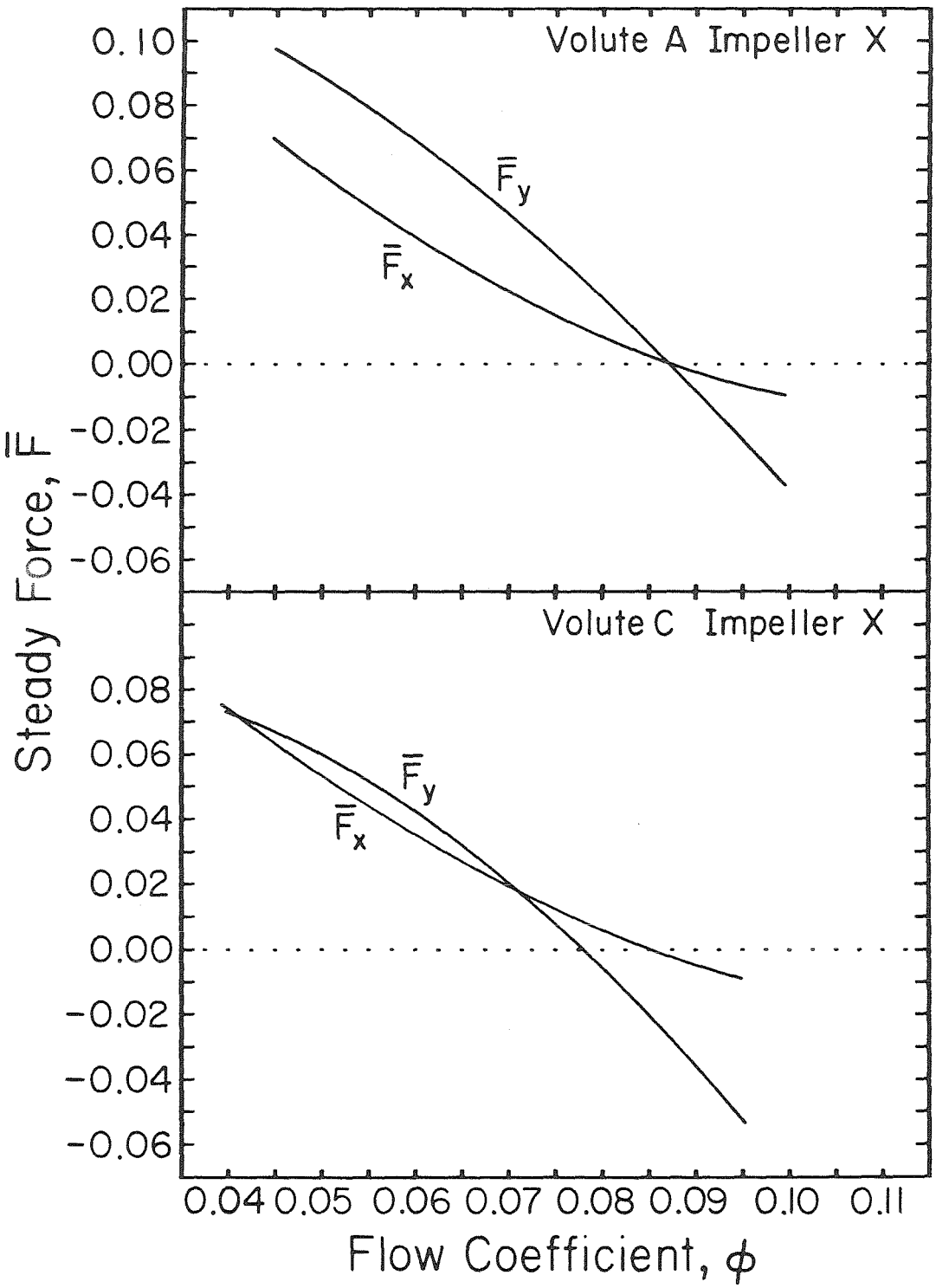

Figure 3.11 Theoretical radial forces on Impeller X when located in the center position of either Volute A or Volute C.

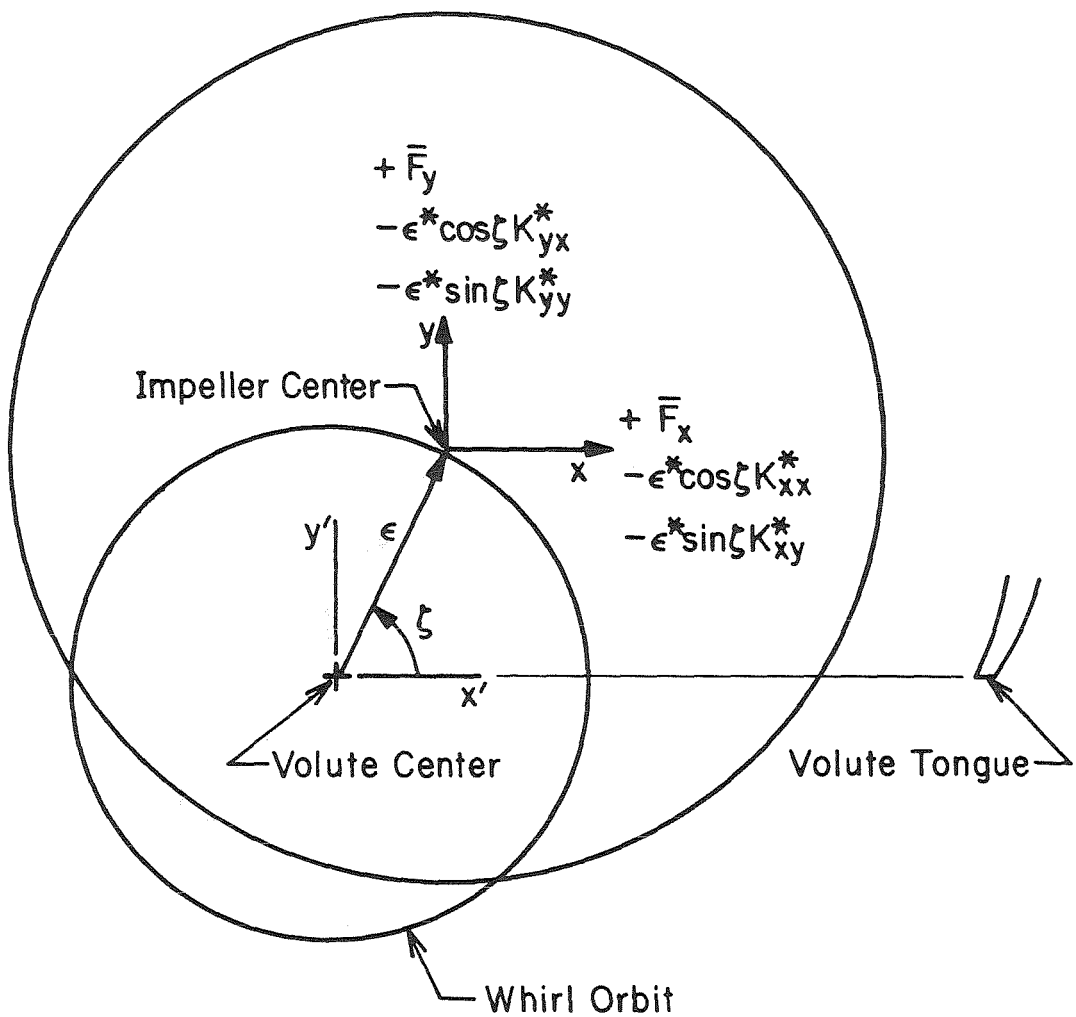

Figure 3.12 Description of the hydrodynamic forces on a stationary (non-whirling) impeller in an eccentric position.

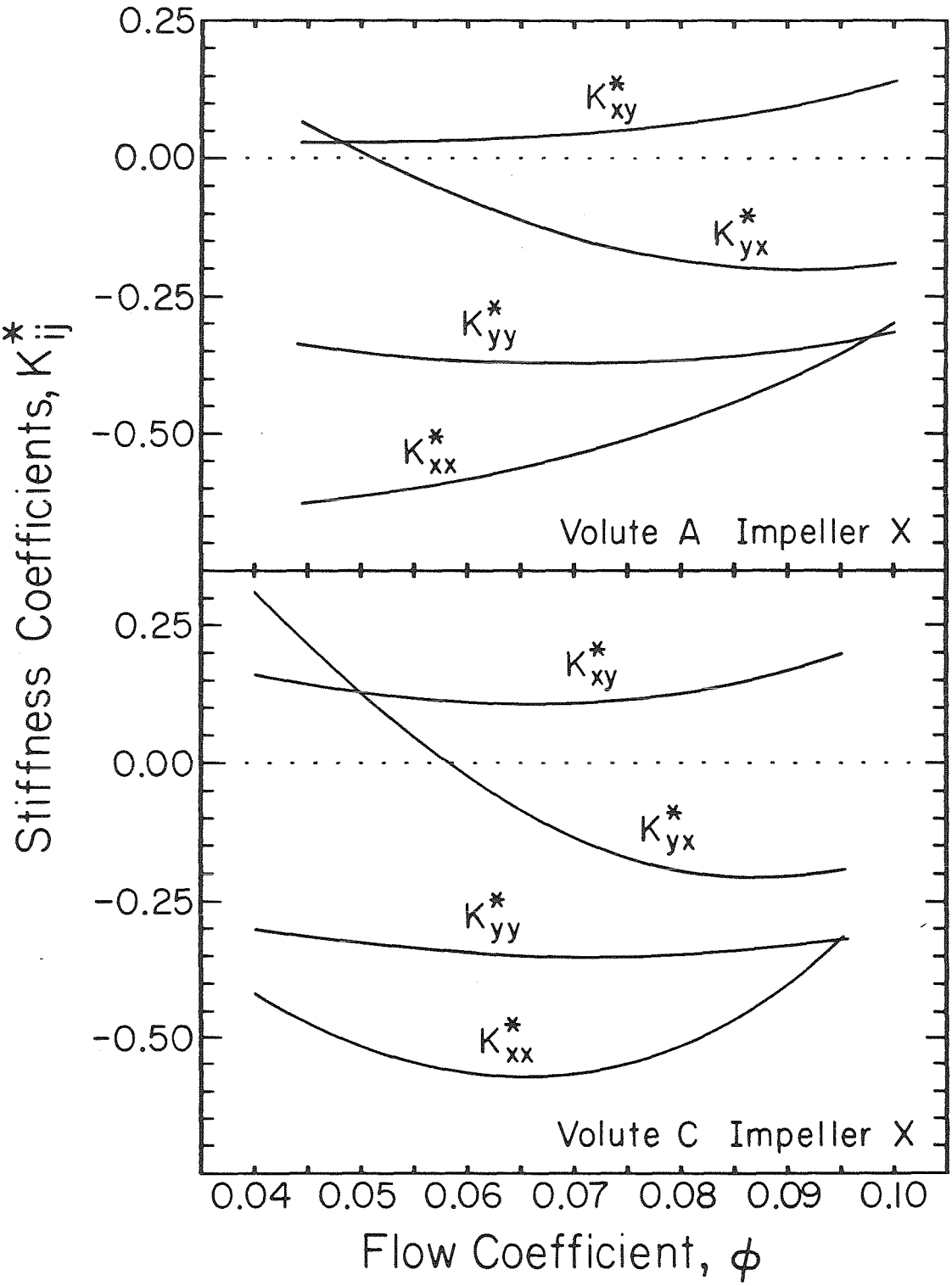

Figure 3.13 Stiffness coefficients as a function of flow coefficient for Impeller X in Volute A and Volute C.

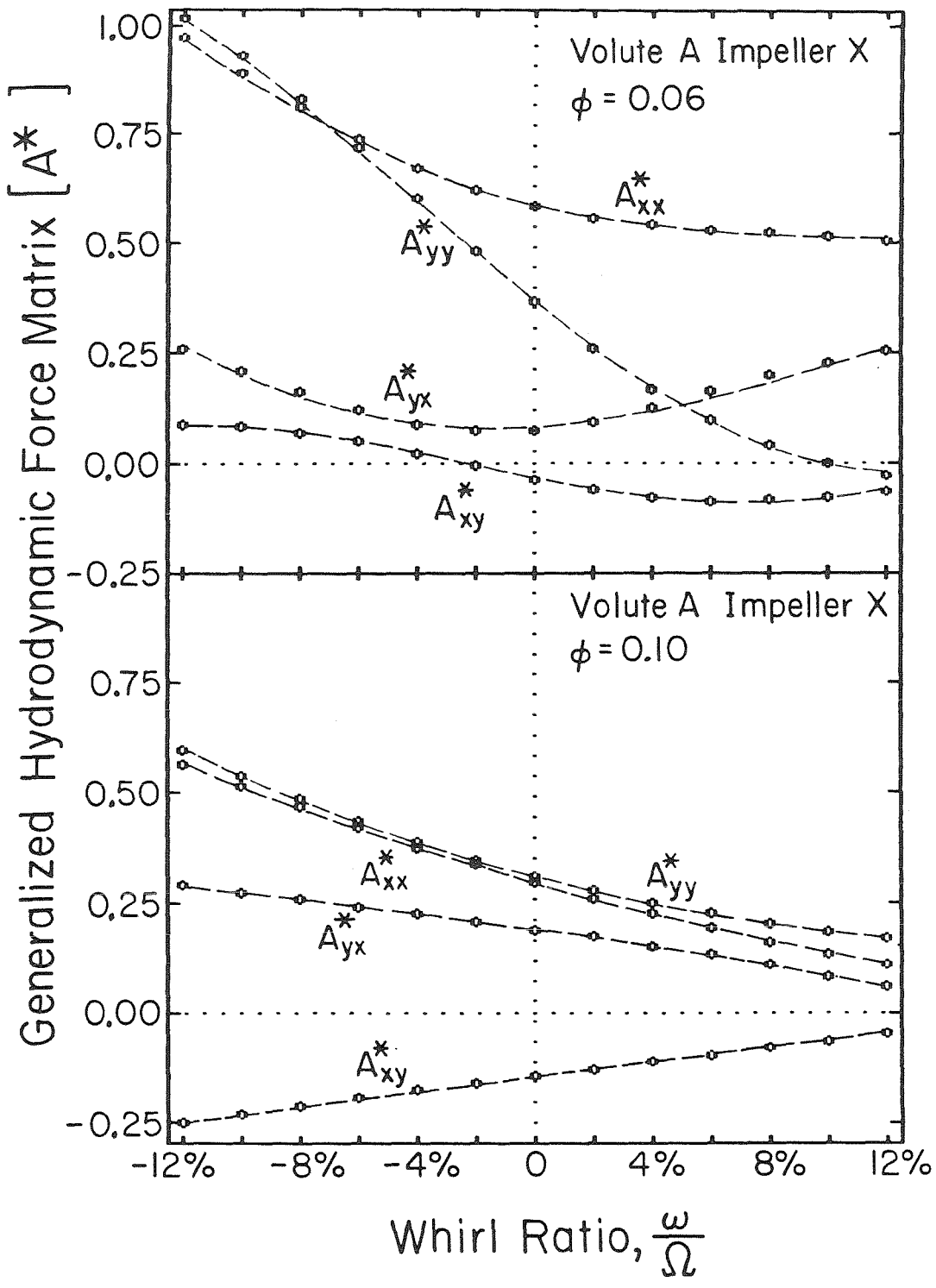

Figure 3.14 Generalized hydrodynamic force matrix, $[A(\omega/\Omega)]$, as a function of the ratio between the whirl speed and the shaft speed for Impeller X in Volute A at two different flow rates.

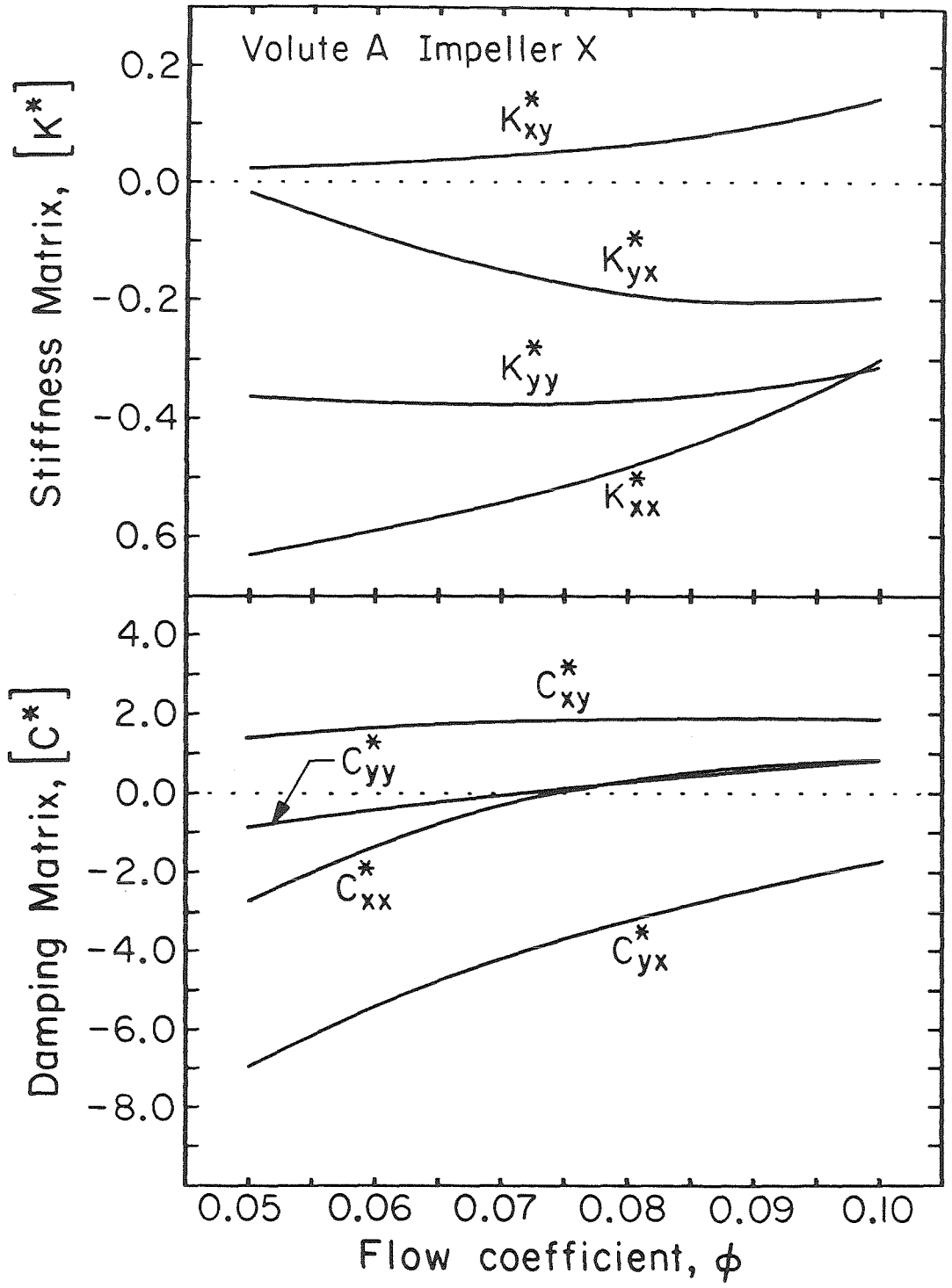

Figure 3.15a Stiffness and damping coefficients as a functions of flow rate for Impeller X in Volute A.

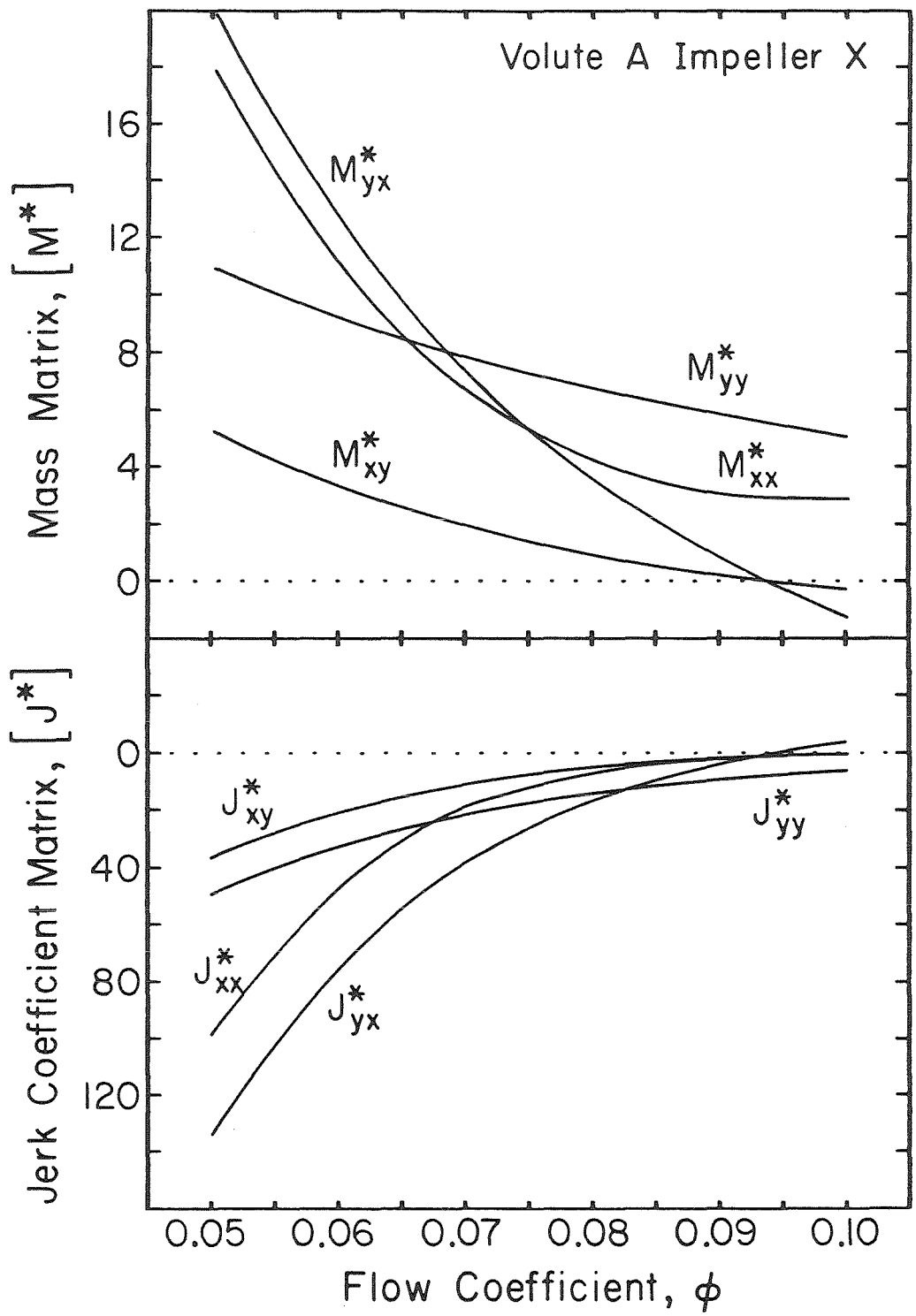

Figure 3.15b Mass and jerk coefficients as functions of flow rate for Impeller X in Volute A.

Chapter 4

EXPERIMENTAL TEST FACILITY

4.1 Description of the Test Facility

The experimental results for this research were obtained using the Rotor Force Test Facility available at the California Institute of Technology. Extensive detail of this facility has been given by Ng [22], Braisted [6], Chamieh [9], and most recently Jery [16], but it is still appropriate to include a general description of the apparatus.

Shown in Figure 4.1 is an overhead view of the Rotor Pump Test Facility with the key components identified. The centrifugal pump being examined is located in the test section. Utilizing this pump, water is circulated in a clockwise direction through the closed loop. The flow rate is governed by the "silent" throttle valve which is servo-controlled using the output from the turbine flow meter located downstream. The overall system pressure is regulated by an air bag situated in the reservoir. The flow fluctuators on either side of the reservoir are remnants from earlier experiments designed to obtain transfer functions for cavitating turbomachinery (see Ng [22] and Braisted [6]). In the present work, the fluctuators have been dismantled. The flow smoothing sections are honeycomb shaped passages which were also used by Ng and Braistead to obtain a more uniform velocity profile for observation with a laser doppler velocimeter (LDV) located downstream of each smoothing section. The LDV's have since been removed, but the flow smoothing sections were retained in the system.

A simplified schematic of the test section is shown in Figure 4.2

along with the internal components of the eccentric drive mechanism. The volute is located in the pressurized chamber of the test section housing so that the volute casings can be inexpensively manufactured from less durable materials. The impeller is mounted on the internal balance (see Section 4.4) and the entire assembly is turned by the 20 hp d.c. main motor that is capable of delivering speeds of 3500 RPM after the 2:1 step-up gear box. The shaft that drives the internal balance and impeller passes through an eccentrically drilled cylinder that causes a 0.0495 inch displacement of the impeller from the center position in the volute. This cylinder is located in the eccentric drive mechanism and can be rotated in either direction by the whirl motor up to 1000 RPM. The eccentric drive causes the impeller to whirl in a 0.0990 inch diameter circular orbit.

4.2 Description of the Test Pumps

4.2.1 Test Impeller

The Byron-Jackson Company of Commerce, California donated the impeller that was used to obtain all of the experimental data in this thesis. A machine drawing of this five bladed cast bronze impeller (referred to as Impeller X) is given in Figure 4.3. Through testing, Byron-Jackson determined that Impeller X has a specfic speed of $N_s = 0.57$ where,

$$N_s = \frac{\sqrt{2\pi\phi_D b/R_2}}{\psi_D^{3/4}} \quad . \tag{4.1}$$

Here, the subscript D refers to the best efficiency point of Impeller X in the Byron-Jackson test volute.

4.2.2 Test Volutes

Two volutes were designed and fabricated out of fiberglass at Caltech. The method used to design the volutes was the principle of constant mean velocity of flow in the volute described in Lazarkiewicz and Troskolanski [20]. Because many analyses place such an emphasis on the design point of a volute, it is important to give a brief description of this procedure. The principle of constant mean velocity assumes that the velocity is uniform around the volute and, according to Stepanoff [25], can be related to the flow coefficient and the specific speed of the impeller by,

$$\bar{V} = K_{cv}\sqrt{2}\,[(2\pi\phi_D b/R_2)/N_s^2]^{1/3} \quad , \tag{4.2}$$

where K_{cv} is an empirical coefficient used to account for the non-uniform velocity distribution and friction in the volute. A constant velocity around the volute will require a linear variation of the cross section with distance from the tongue so that,

$$\bar{A}(\theta') = A_v\,\theta'/2\pi \quad . \tag{4.3}$$

From Equation 4.2 and the definition of the flow coefficient,

$$A_v = (2\pi N_s\phi_D)^{2/3}(R_2/b)^{1/3}/(K_{cv}\sqrt{2}) \quad . \tag{4.4}$$

The coefficient K_{cv} is presented as a function of specific speed in Stepanoff [25] and for Impeller X it is determined that $K_{cv} = 0.37$.

Using the above procedure, Volute A was designed and constructed by Chamieh [9]. According to this empirical methodology it is considered to be "well matched" with Impeller X for $\phi_D = 0.092$. Similiarly, Volute C was designed with $\phi_D = 0.085$. Figures 4.4 and 4.5 present the overall geometry of the two volutes and Figure 4.6 gives the cross sectional

dimensions every 45 degrees. It is important to recognize from the above discussion that these design points are purely empirical and depend upon the particular method used in designing the volute. This is why an emphasis was placed on using the actual volute geometry in developing the theoretical analysis of this paper.

4.3 Modification of the Test Facility

4.3.1 Remodeling the Test Section

In order to evaluate the present theoretical analysis or "model", the forces acting on the impeller and the pressure distributions at the inlet of the volute are measured. Since the model only deals with the interaction between the impeller and the volute, it is necessary to isolate the flow in the volute from all other flows. This was partially achieved by placing rings at the impeller discharge as shown in Figure 4.7. These rings were installed so that there was approximately 0.005 inch clearance between the rings and the impeller (this is approximate because a $\pm$0.002 inch axial misalignment of the impeller exists at the discharge). In addition to using the rings, the front seal was adjusted to 0.005 inch clearance to reduce leakage flow at the inlet of the impeller.

From the way in which the test section is constructed, it is possible that fluid trapped in the eccentric annular gap between the impeller front shroud and the front alignment flange of the test section will contribute to the net force on the impeller. The area described is shown in Figure 4.7. In an attempt to reduce this effect, most of the experiments were performed with the alignment flange removed. Doing so exposes the front shroud of the impeller to the reservoir conditions of the test section chamber. The influence of these forces can then be estimated by

comparing the current test results to those taken by Chamieh [10] and Jery [17] when the flange was in place. The point at which the flange was removed is shown in Figure 4.7.

4.3.2 Pressure Taps in the Volute

Pressure taps were installed in both Volutes A and C in order to observe the static pressure variations around the volute near the inlet, as shown in Figure 4.7. Small tubes that ran through port holes in the test section connected the pressure taps to a total of forty manometers. The taps were placed alternately on the front and back of each volute about every 10 degrees, but extra taps were used near the tongue. The precise angular locations of the pressure taps are documented in Appendix D and the circle diameters on which the taps were drilled are shown in Figures 4.4 and 4.5. It might have been instructive if the taps could have been placed directly at the impeller discharge, but this was precluded by the eccentric position of the impeller in the volute.

4.3.3 Pressure Taps in the Front Alignment Flange

Taps were placed in the front alignment flange before it was removed so that the pressure in the annular gap could be measured. This was done so that the net force on the impeller contributed by the flow in this region could be estimated for further comparison with the work of [10] and [17]. Because the axial variation of the pressure in the annular gap was unknown, two rows of twenty taps were used (see Appendix D for precise location). One row was placed over the front seal of the impeller at the narrowest point of the gap, and the other row was installed where the gap was widest as shown in Figure 4.7. The tap holes were connected in such a way that either the seal tap or the mid-section tap could be viewed independently by plugging the unused pressure tap

with epoxy. With the same arrangement of tubes that was used in the volute pressure measurements, the pressure taps for the annular gap were connected to a bank of twenty manometers.

4.4 Instrumentation and Measurement Errors

4.4.1 The Internal Balance for Force Measurements

The most complicated piece of instrumentation used in this research was the internal balance developed by Jery [16] under the supervision of Professors Acosta, Brennen, and Caughey at the California Institute of Technology. Basically the internal balance consists of a single piece of steel that has been machined into two disks linked parallel to one another by four square posts. Nine solid state strain gage bridges are located on the four posts so that the deflections of the posts can be measured. The wiring from the strain gages runs through the main drive shaft to the slip ring assembly and from there to the signal amplifiers and processing equipment. The forces on the cantilever impeller that is mounted directly to the internal balance were calculated using a force to strain signal transfer matrix. This transfer matrix was obtained by a static calibration, and was further reinforced by dynamic tests (see Jery [16]). Since there are six force components, three of the bridges are actually redundant and only used as auxiliaries. For the current work only the radial forces are of interest.

The principle way of performing a dynamic check of the calibration was to use the internal balance to measure the weight of the impeller while it was rotating. When this was done for Impeller X over a range of speeds from 300 to 3000 RPM the results were within $\pm$4% for the magnitude of the weight (~9.5 pounds) and within 2 degrees for the direction. An additional test was performed by whirling the impeller and measuring the

centifugal force. The mass was predicted to within 2% by this procedure.

4.4.2 Pressure Transducers for Total Head Rise Measurements

Two Statham pressure transducers were used to measure the static pressures in the large pipes immediately downstream of both the upstream and the downstream flow smoothing sections. From these results the total head rise across the pump was calculated after including a small correction for the dynamic head difference caused by the difference in the cross sectional areas. The two transducers were calibrated by comparing their conditioned outputs (read in volts on a digital voltmeter) against an accurate Heise pressure gage. The signals were found to be linear over the range of pressures measured.

4.4.3 Manometer Measurements of the Pressure Taps

The pressure taps around the volute were read using forty 42 inch inverted air/water manometers. A common pressure was applied to the airspace the top of the manometers and the tubes leading from the pressure taps were connected to the bottom of each manometer. Flip valves at the base of the manometer tubes allowed the pressure taps to be switched off simultaneously, thereby freezing the results once the system came to equilibrium. One of the pressure taps was also connected to the bottom of a mercury manometer. The top of the mercury manometer was connected to a static pressure tap in the pipe upstream of the lucite viewing window (and therefore upstream of the pump). This furnished the upstream total head reference for the pressure tap measurements once the correction for the velocity head was made.

Before each series of tests the manometers were leveled and the lines leading to the pressure taps were bled. The water manometers could accurately be read to within $\pm$0.2cm (0.08 in.) of water meaning that the

pressure taps measurements relative to one another at a given flowrate are fairly accurate. The mercury manometers were slightly less accurate and could only be read to within $\pm$0.2in. of Hg (2.5 in. of water). This will effect the relative accuracy of the readings from one flow rate to another.

4.4.4 Magnetic Pickup for Impeller Speed

A magnetic pick-up transducer in conjunction with an HP 5302A universal counter was used to find the rotational speed of a 64 tooth steel wheel mounted on the main shaft. A rather intricate speed control system is used because an accurate assessment of the angular position of the impeller is required by the internal balance. The reader is referred to the work of Jery [16] for discussion of the control system and the data acquisition procedure.

4.4.5 Turbine Flowmeter

The flow rates were measured using a 1250 GPM Potter turbine flow meter. In comparing the measurements of the turbine meter to those of an electro-magnetic flow meter, the results were found to be linear. However, for flows less than 40 GPM the turbine meter did exhibit oscillations of approximately 2 GPM.

4.5 Eliminating the Tare Forces

In the data reduction procedure, all of the forces that were clearly not associated with the hydrodynamic forces were eliminated from the results of the internal balance measurements. These tare forces were in part calculated by running the impeller dry and inside of the test chamber without a volute. This procedure was repeated for every combination of main shaft and whirl speeds that were to be used in actual test

runs so that the dead weight and inertial forces could be eliminated. In addition, the buoyancy forces were also eliminated by directly subtracting the difference between the wet and dry weight of the impeller from the results.

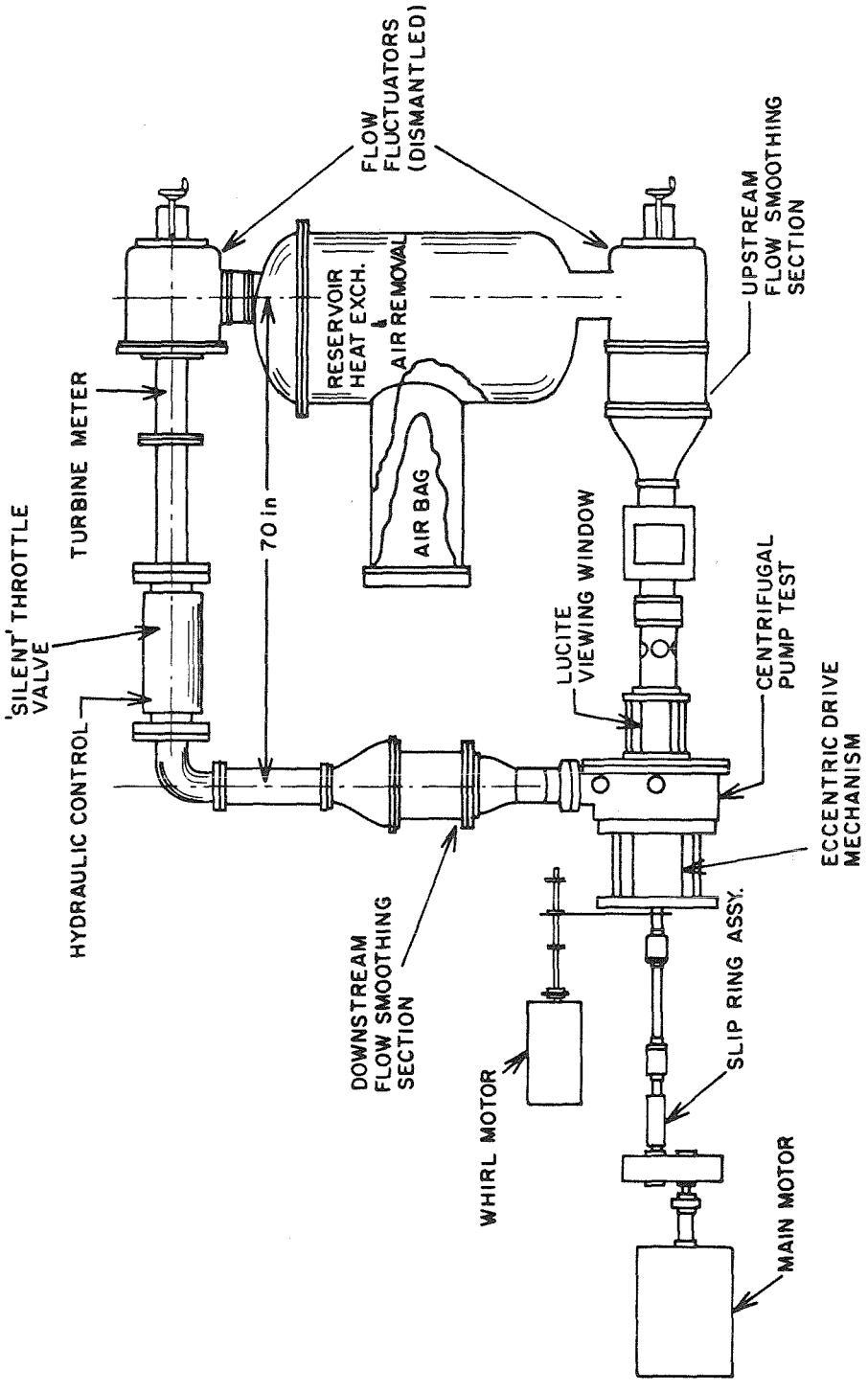

Figure 4.1 Schematic overhead view of the Rotor Force Test Facility.

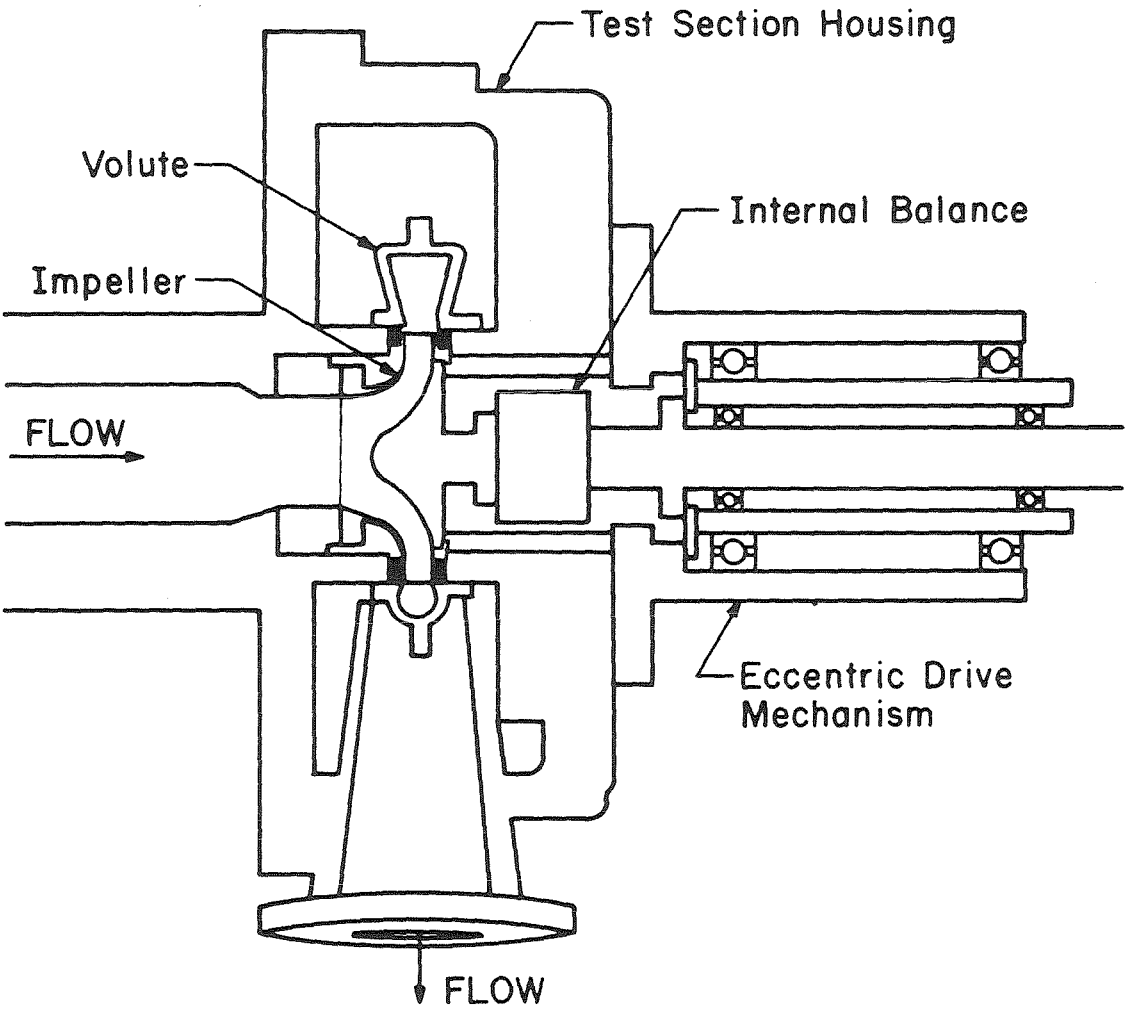

Figure 4.2 Schematic of the test section and the eccentric drive mechanism.

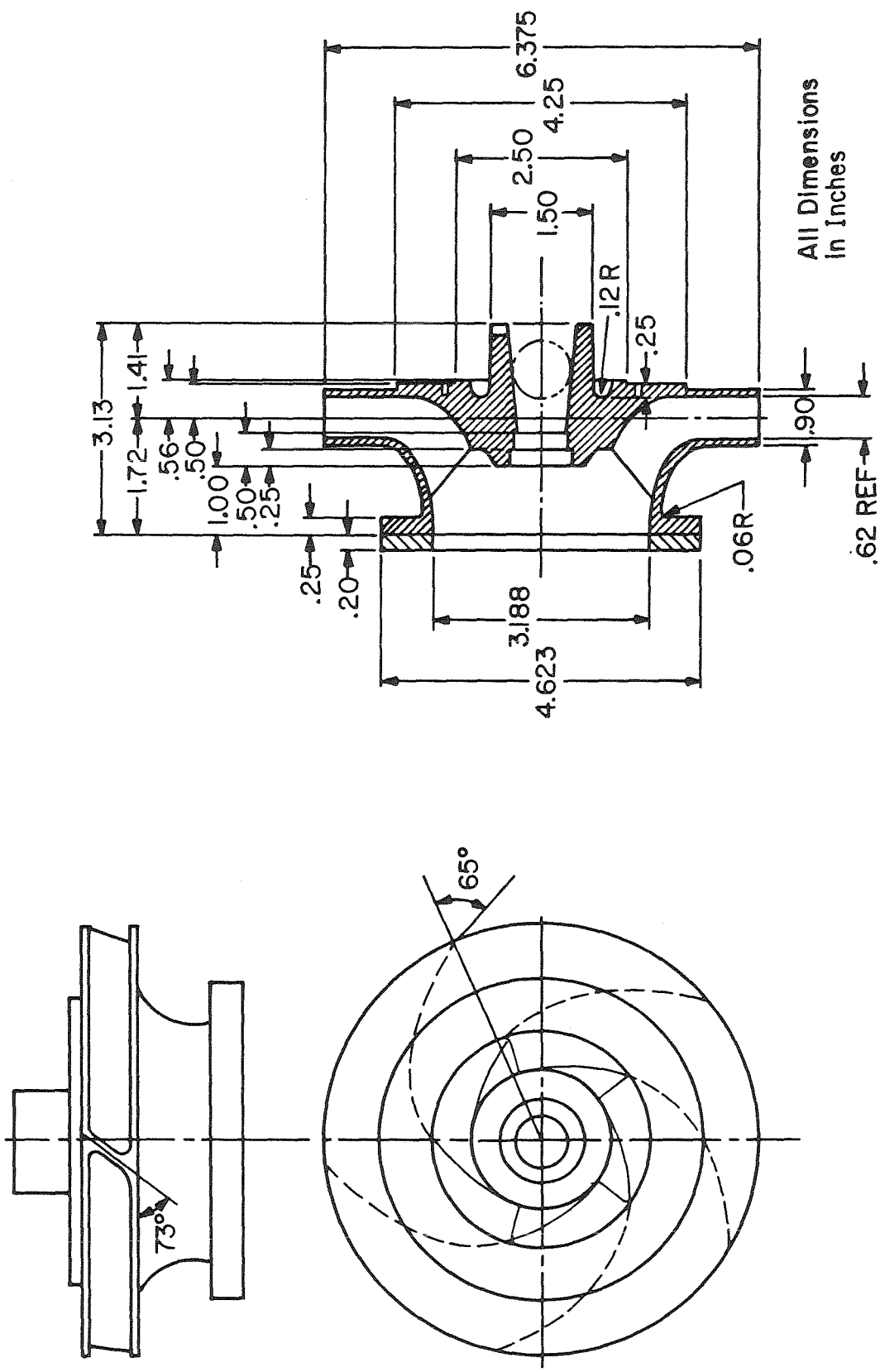

Figure 4.3 Dimensions of Impeller X.

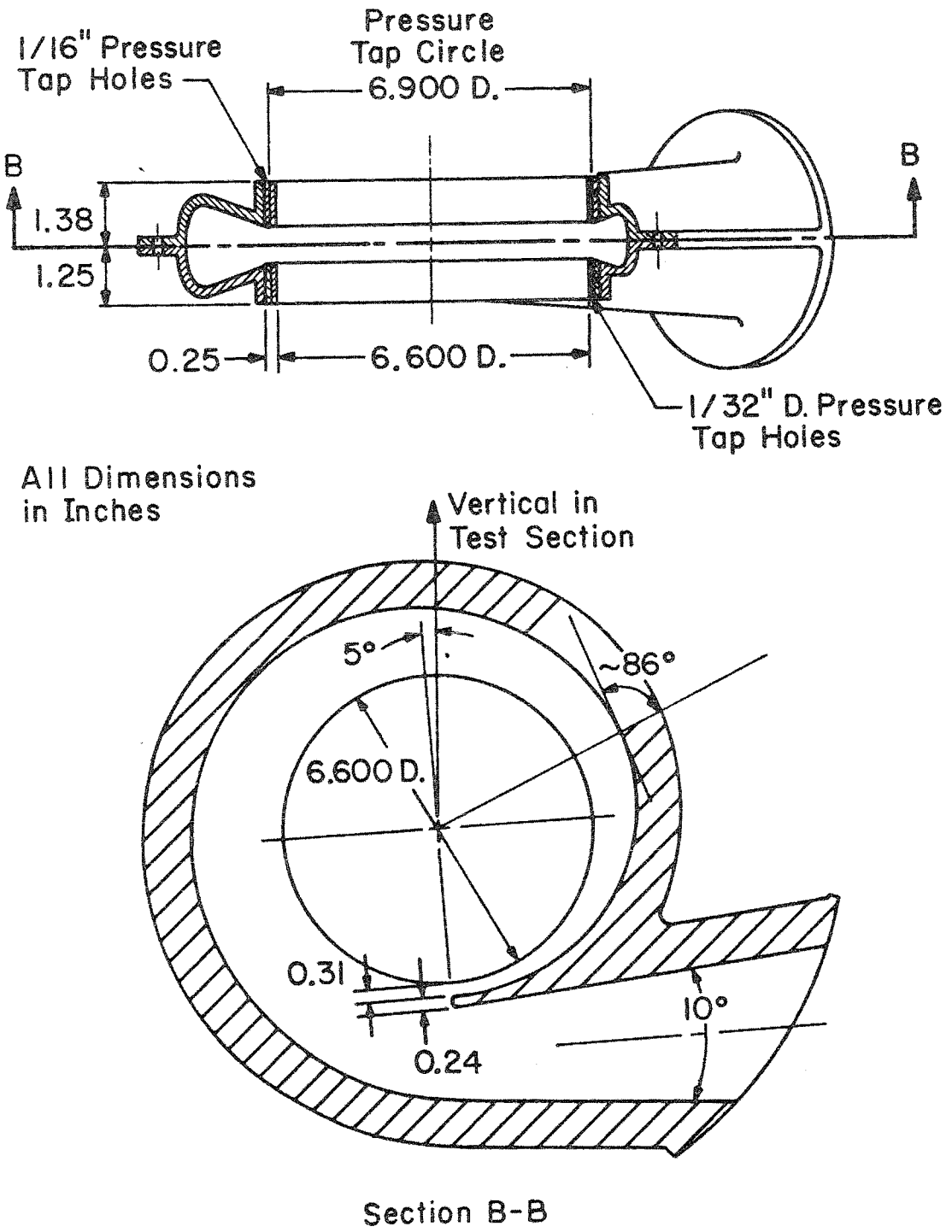

Figure 4.4 Overall dimensions of Volute A.

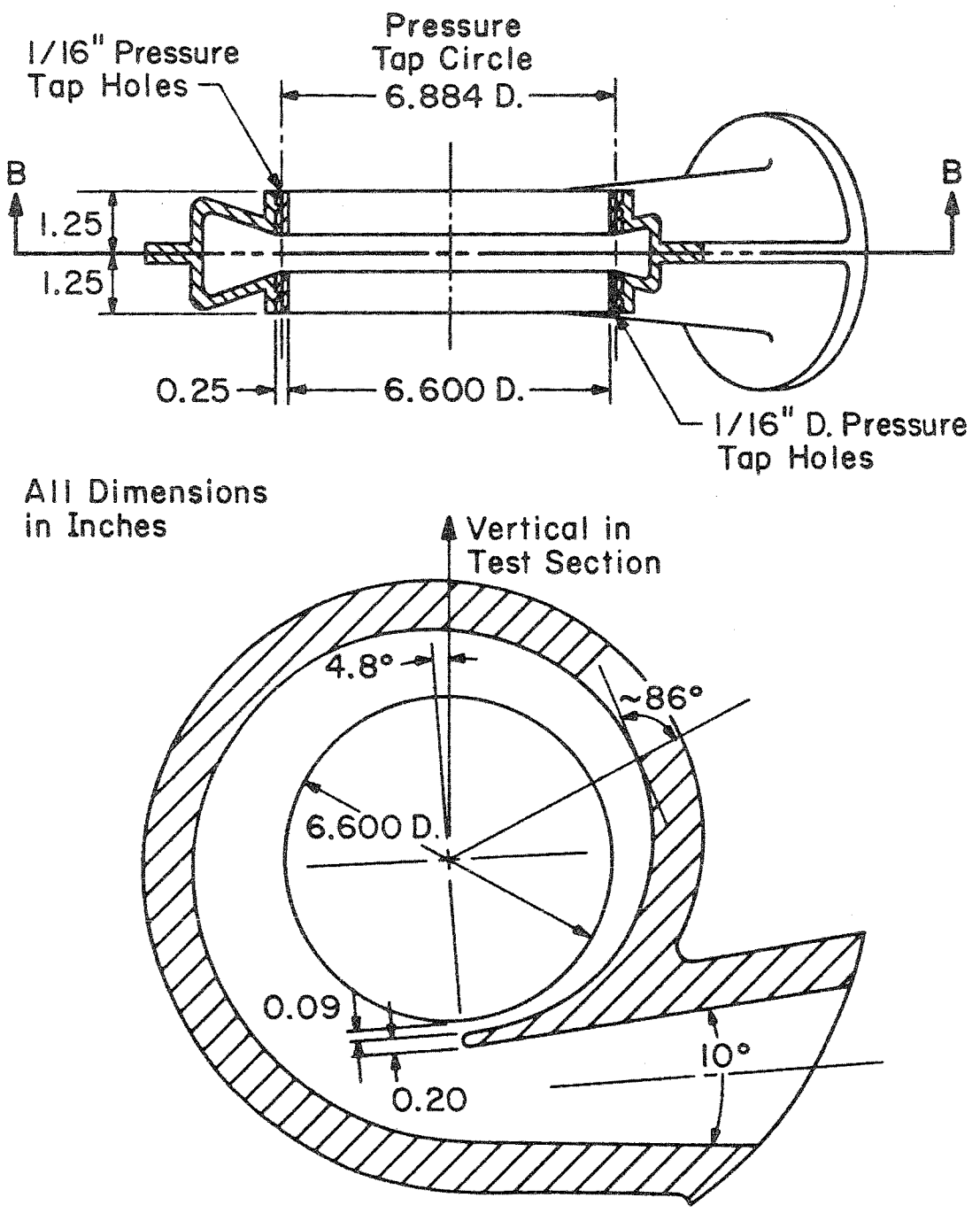

Section B-B

Figure 4.5 Overall dimensions of Volute C.

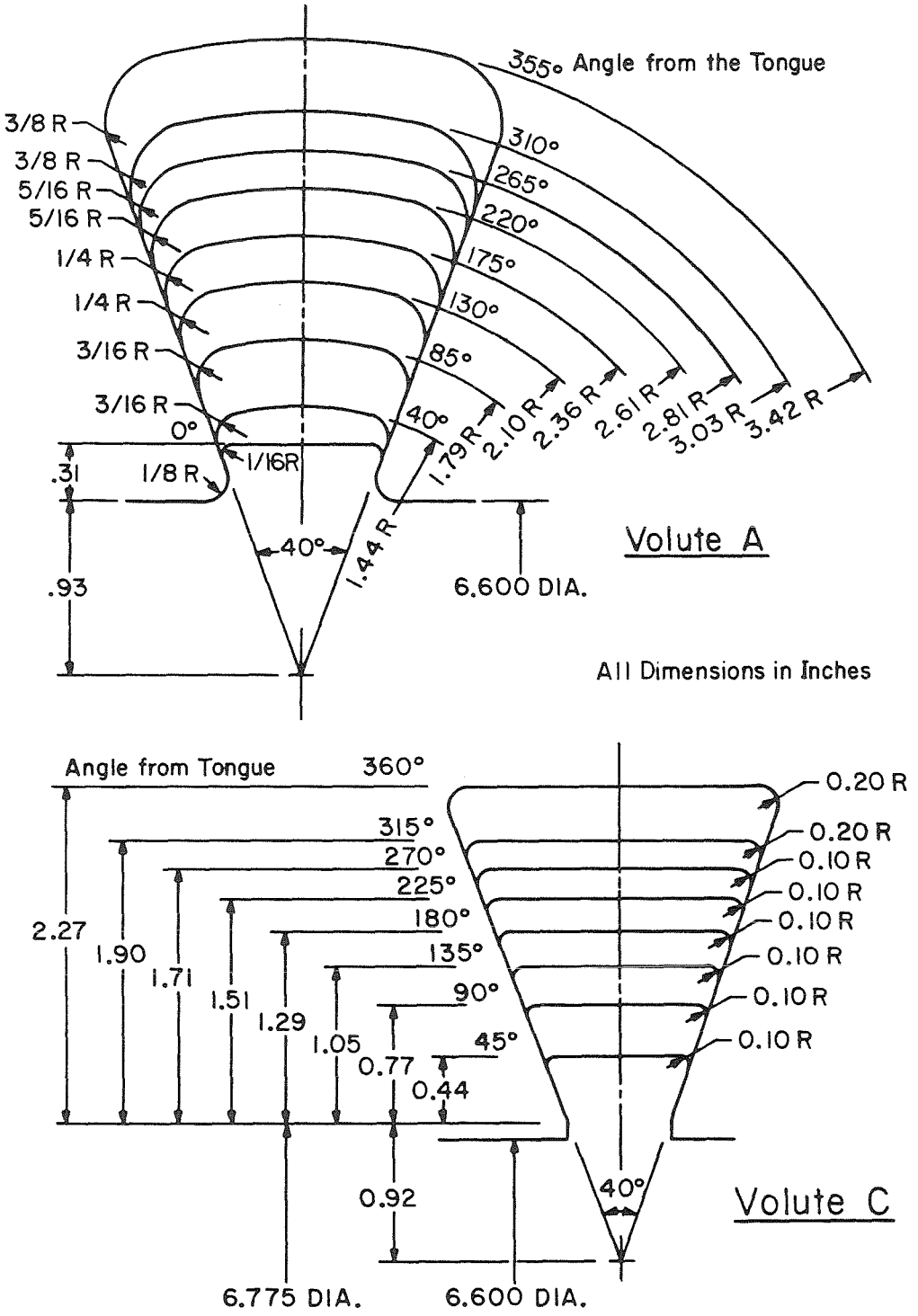

Figure 4.6 Dimensions of the cross sections of Volute A and Volute C.

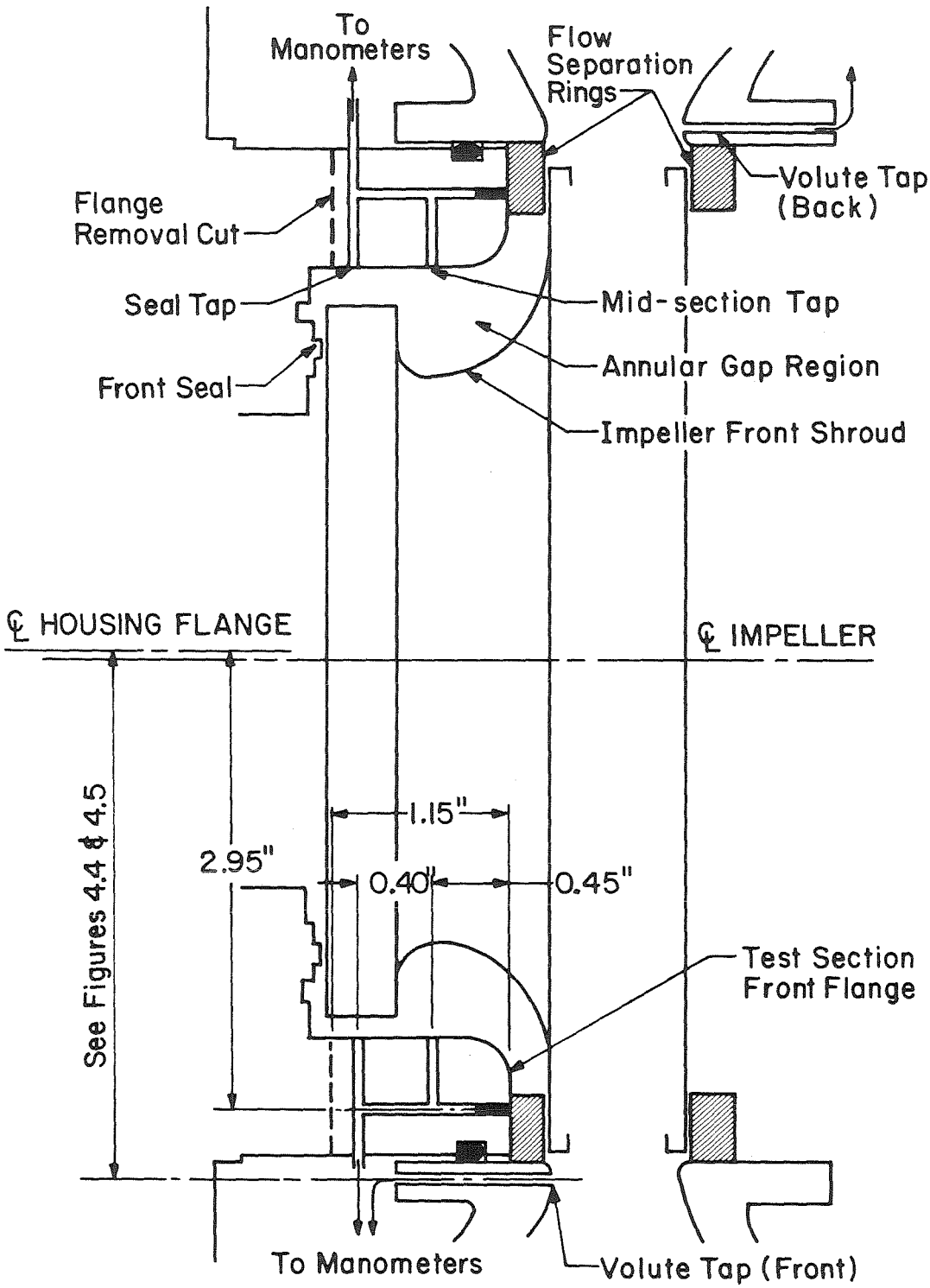

Figure 4.7 Schematic to show the placement of pressure taps and flow separation rings.

Chapter 5

EXPERIMENTAL RESULTS AND COMPARISON WITH THEORY

5.1 Head Rise Performance Characteristics

To apply the current theoretical model, it is essential to have an accurate measurement of the total head rise across the pump as a function of flow rate. Shown in the upper part of Figure 5.1 are the experimental total head measurements for the pump consisting of Impeller X in Volute A, and in the lower part of the figure are the results for Impeller X in Volute C. As expected, the head coefficients were found to be independent of speed and therefore Reynolds Number effects. For neither volute was there any consistent and observable variation of the head coefficient with the impeller position.

The only noticeable change in the pump performance that occurred, took place when the flow separation rings were installed (see Figure 4.7). To demonstrate the difference in the total head output, Chamieh's [9] results for the same pump without the flow separation rings are included in the upper graph of Figure 5.1. Unless otherwise stated, all of the results presented in this thesis were taken with the rings installed because the interaction between the impeller and the volute is the primary focus of this investigation. It is, however, recognized that the leakage flow from the volute into the annular gap (see Figure 4.7) will have an influence on the total force acting upon the impeller. Further discussion of flow in this region will be given in Section 5.5.

5.2 Correlation Between Predicted and Measured Pressures

As was described in the previous chapter, pressure readings were taken at the inlet of the volute in order to evaluate the predictions of the model. Measurements from the ring of pressure taps at $r' = R_t$ in Volute A are shown in Figure 5.2 and the same information for Volute C is shown in Figure 5.3. The dotted lines in both of these figures are included only to aid in distinguishing the results from one flow rate to another. The pressures were taken at impeller speeds from 800 RPM to 1000 RPM and the resulting pressure coefficients were found to be independent of the speed. The taps were installed so that they alternately measured pressures from the front and back of the volute over most of the pressure ring perimeter. This is the why there is an apparent jump in the data from one tap to the next. The slightly larger pressures measured by the front taps might be attributed to the front taps being larger than the back taps in Volute A. But in Volute C the tap holes were all the same size and the front taps still gave slightly higher readings. This leads to the conclusion that the difference was caused by a small rearward axial component of the velocity at the discharge of the impeller.

When examining the pressure coefficients at lower flow rates, the most noticeable feature is that there appears to be one particular point where volute inlet pressure is independent of the flow rate. This same feature was predicted by the model and even the particular crossing point is very close to the observed results when allowances are made for the impeller not being positioned at the volute center. To account for the impeller position and the fact that the pressures are not measured at the impeller discharge, Equations 2.15, 2.22, 2.31 and 2.33 are combined to give the theoretical pressure at the volute tap ring as,

$$P_v^* \Big|_{R_t} = \overline{D_p} + 2\overline{V}^2[\ln(R_t/R_2) - \varepsilon^* \cos(\theta' - \zeta)] \qquad (5.1)$$

$$+ \varepsilon^*[D_{pc} + 4\overline{V}V_c \ln(R_t/R_2)]\cos\zeta$$

$$+ \varepsilon^*[D_{ps} + 4\overline{V}V_s \ln(R_t/R_2)]\sin\zeta$$

Figures 5.4 through 5.6 give a direct comparison of the theoretical and experimental pressures at $r' = R_t$. Figure 5.4 shows that from about 75% to 100% of the design flow rate of Volute A ($\phi_D = 0.092$), there is an extremely good correlation of the results. For flow rates less than about 75% of design the correspondence is still fair, as shown in the upper part of Figure 5.5, but for flow rates greater than the design point the predictions begin to falter as demonstrated in the lower part of Figure 5.5. Figure 5.5 also illustrates the effects of moving the impeller from a position nearest to the tongue ($\zeta = 0°$) of Volute A to a position farthest from the tongue ($\zeta = 180°$). From this figure it appears that the model adequately predicts the pressure changes which occur when the impeller is moved in the x direction. Similar results were found for movement in the y direction but the magnitude of the changes were smaller.

To complete the comparison of pressure distributions, Figure 5.6 gives the results when Impeller X is positioned near the tongue of Volute C. The range of flow coefficients presented is from about 63% to 112% of the design ($\phi_D = 0.085$). Just as with Volute A, the best predictions are for flow rates just below design.

5.3 Radial Forces Acting on the Impeller

5.3.1 Integrated Pressure Forces

In the theoretical results presented in Chapter 3, it was found that the asymmetric pressure distribution at the impeller discharge was the major contributor to the radial force acting on the impeller. When the measured pressure results are integrated around the impeller, an estimation of this force can be made. It will be assumed that on the average the pressure is constant in the axial direction across the impeller, even though small variations were shown to exist in Figures 5.2 and 5.3.

Because the impeller is actually located a distance $\varepsilon^* = 0.0155$ from the center of the pressure taps, the pressure results cannot be directly integrated. Instead, the change in the relative coordinate systems must be taken into account using the approximation,

$$P_v(R_2,\theta') = P_v(R_2,\theta_2 - \varepsilon^*\sin(\theta_2 - \zeta)) = P_v(R_2,\theta_2) - \varepsilon^*\sin(\theta_2 - \zeta)\,\frac{dP_v}{d\theta_2} \quad , \quad (5.2)$$

and neglecting the radial variation in the pressure from $r = R_2$ to R_t'. The pressures may then be integrated around the perimeter of the impeller to give,

$$F_{vx}(\zeta) = -W_i R_2 \int_0^{2\pi} P_v \Big|_\zeta [\cos(\theta_2) + \varepsilon^*\cos(2\theta_2 - \zeta)]d\theta_2 \quad , \quad (5.3a)$$

and,

$$F_{vy}(\zeta) = -W_i R_2 \int_0^{2\pi} P_v \Big|_\zeta [\sin(\theta_2) + \varepsilon^*\sin(2\theta_2 - \zeta)]d\theta_2 \quad , \quad (5.3b)$$

These expressions are only approximate because the radial variation in the pressure was neglected, and from Equation 2.22 of the volute model the pressure was predicted to vary logarithmically in the radial direction. One note of caution that should be added is that even if the

impeller was positioned in the center of the volute, there would still be error introduced into the force calculation by the radial pressure variation. This error would come about because of the dependence on the volute flow velocity which varies with θ'. Unless the pressure results are taken directly at the impeller discharge there will always be a velocity contribution. It was assumed though, that Equations 5.3a and 5.3b would at least give an estimate to the pressure forces acting upon the impeller.

Using the above approximations, the volute pressure forces on Impeller X when it positioned near the tongue ($\zeta = 0°$) are given in Figure 5.7. The theoretical curves that are included in this figure were also calculated with $\zeta = 0°$. From the top graph of Figure 5.7 the predicted forces are shown to correlate well with the pressure forces on Impeller X in Volute A. The comparison is not as good when Volute C is used as shown in the lower part of the figure, but for most engineering applications only the magnitude of the force is of primary concern and the theory predicts this satisfactorily. Also included in Figure 5.7 are the direct force measurements taken with the internal balance developed by Jery [16]. These results reaffirm the conjecture that the non-uniform pressure distribution at the impeller discharge is the principal cause of the radial force on the impeller.

5.3.2 Direct Force Measurements

Using the internal balance, the forces were measured with the impeller placed in four positions of the eccentric orbit, $\zeta = 0, 90, 180,$ and 270 degrees. The forces were then averaged and the results when Volute A was used in the pump are presented in Figure 5.8. Also included in the figure are the average pressure forces for two flow rates and the

corresponding theoretical predictions. It is shown that the analytical model over-predicts the mean forces slightly, but in general the comparison is good. Similar results for Volute C are shown in Figure 5.9. For Volute C the radial force measurements were taken at both 1000 RPM and 2000 RPM impeller speeds. The results show that the non-dimensionalized force is independent of the impeller speed, as was anticipated from the pressure measurements.

5.3.3 Comparison with Previous Force Predictions

For historical reference, Figure 5.10 presents a comparison between the current theoretical radial forces on Impeller X in Volute A, the forces predicted by Colding-Jorgensen [12], and the experimental results obtained by Chamieh [9]. The results of Colding-Jorgensen were calculated using the same spiral angle as Volute A (86 degrees), but the blade angle used was slightly different from that of Impeller X (67.5 degrees as compared to 65 degrees for Impeller X). Even with this minor difference in the impeller geometry, the two pumps are still similar enough to estimate that Colding-Jorgensen's model will predict forces with about half the magnitude of the current model.

The experimental results of Chamieh [9] were obtained using Impeller X in Volute A, but without the flow separation rings and the modified front flange (see Section 4.3.1). The impeller forces in the y direction measured by Chamieh are shown to be very close to those predicted by the current model, unlike the forces in the x direction. It is difficult to justify a direct comparison with this work though, because without the flow separation rings in place, there would be extensive leakage into the annular gap shown in Figure 4.7. The forces on the impeller that result from this leakage will be discussed further in Section 5.5.

5.4 Stiffness and the Generalized Hydrodynamic Force Matrices

5.4.1 Hydrodynamic Stiffness Matrices

Using the internal balance, the hydrodynamic stiffnesses were experimentally determined by measuring the radial forces on the impeller when it was positioned at four eccentric positions ($\zeta = 0,90,180,270$ degrees) in the volute. Once the x and y force components are obtained from each of the four positions, the elements of the stiffness matrix are calculated by,

$$K_{xx} = (F_x(0) - F_x(180))/2\varepsilon \quad , \qquad K_{xy} = (F_x(90) - F_x(270))/2\varepsilon \quad , (5.4a,b)$$

$$K_{yx} = (F_y(0) - F_y(180))/2\varepsilon \quad , \qquad K_{yy} = (F_y(90) - F_y(270))/2\varepsilon \quad , (5.4c,d)$$

These calculations were made at several different flow rates for Impeller X in Volute A and Volute C and the results are shown in Figures 5.11 and 5.12 respectively along with the theoretical predictions. Also given in Figure 5.11 are the stiffness matrix components that were calculated using the volute pressure forces described in Section 5.3. Comparing the experimental and theoretical results, it is shown that the model gives slightly lower magnitudes for the stiffnesses, but their variation with flow rate is predicted fairly well. The only exception to this is the K_{yx} coefficient, which from the experiments would appear to be independent of the flow rate. Presently there is no suitable explanation of why this might be true.

In Chamieh's [10] work it was experimentally determined that the stiffnesses were given approximately by $K_{xx} = K_{yy} = -2.0$ and $K_{xy} = -Kyx = 0.9$ for Impeller X in Volute A, regardless of the flow rate. The stiffnesses from the current experiments are shown to vary with flow rate and are only about 25% of those given by Chamieh. This difference

can be directly attributed to the installation of the flow separation rings and the removal of the front flange of the test section as will be shown in Section 5.5.

5.4.2 Force Effects of Whirling the Impeller

It is uncertain how much of the force measured on the whirling impeller is the result of the interaction with the volute, and how much is caused by the presence of fluid at the outer shroud of the impeller. As was explained in the Chapter 4, a portion of the front flange of the test section was removed so that the front shroud of the impeller was subject to the "reservoir" conditions of the test chamber. While this may have eliminated the front shroud pressure imbalance for the stationary impeller, it is unlikely that there will be no net force on the front shroud when the whirling impeller is agitating the water in the test section chamber.

Under the assumption that these forces will be small at lower whirling speeds, tests were run for whirl ratios between $\pm$ 20% with a main shaft speed of $\Omega = 1000$ RPM. The resulting generalized hydrodynamic force matrix coefficients are shown in Figure 5.13 for Impeller X in Volute A operating at the design flow rate, along with the predictions of the current model and the two dimensional distributed vortex model of Tsujimoto [29]. In comparing the results, it is shown that both models predict the general trends of the coefficients, but the model proposed by Tsujimoto tends to give a more accurate assessment of the magnitudes.

To complete the comparison between the current model and previous models, Figure 5.14 shows the hydrodynamic stiffness and damping matrices calculated by Colding-Jorgensen [12] for a pump similar to that of Impeller X in Volute A. Even though the diagonal elements of the stiff-

ness matrix are shown to be of the same order, the off-diagonal terms which would induce whirl are shown to be much larger in the current model. As for the damping matrices, Colding-Jorgensen's predictions are only about one tenth of the magnitude of those predicted by the current model. Unfortunately, test results giving the damping are not available.

5.5 Radial Pressure Forces and Stiffnesses Caused by Fluid on the Front Shroud of the Impeller

Up to this point, the primary focus of this work has been to study the interaction between the impeller and the volute alone. There has been some concern though, that the fluid surrounding the front shroud of the impeller might also contribute to the measured forces. In the previous work by Chamieh [9,10] and Jery [16,17], the alignment flange of the test section extended into the volute and fluid was trapped in the annular gap between the flange and the front shroud of the impeller (see Figure 4.7). This problem was further complicated by the lack of a seal between the annular gap region and the discharge of the impeller. The water in this region will circulate when driven by the shear forces from the spinning impeller and the pressure gradient in the volute. Since the impeller is located eccentrically with respect to the alignment flange, the flow in the gap will be non-uniform and the pressure will therefore vary circumferentially. In the current experimental work, the test section was modified in an effort to minimize these effects by sealing the volute flow from the annular gap and exposing the annular gap region to the reservoir-like conditions of the test chamber (see Figures 4.2 and 4.7).

Pumps that are normally used in industrial applications would more closely resemble the unmodified pump of Chamieh and Jery, although the

annular gap clearances are ordinarily much smaller. To estimate the influence of the flow in the annular gap on the overall hydrodynamic forces, pressure measurements were taken in this region and the results are shown in Figure 5.15. The upper diagram gives the annular gap pressure data when the rings are installed to separate the annular gap flow from the volute flow, and the lower diagram shows the results when no rings were used. For both situations the pressures have been referenced to the upstream total head. What is apparent in examining the two figures is that the annular gap flow and the volute flow have a considerable influence on each other when the rings are not used. Also, by comparing the pressure measurements taken over the impeller inlet seal to those made over the midsection of the impeller shroud, it appears that there is a negligible variation of the pressure in the axial direction.

Just as the volute pressures were integrated around the impeller to estimate the radial forces, the pressures in the annular gap were integrated to obtain the net force acting on the impeller. The geometry used in this calculation is shown in Figure 5.16. By once again neglecting the radial and axial variations in the pressures, the pressure forces are given as,

$$F_{ax}(\zeta) = -\int_0^{2\pi} A_p(\theta,\zeta)[\cos(\theta) + \varepsilon^* \cos(2\theta - \zeta)]d\theta \int_0^T r\, dz \quad , \tag{5.5a}$$

and

$$F_{ay}(\zeta) = -\int_0^{2\pi} A_p(\theta,\zeta)[\sin(\theta) + \varepsilon^* \sin(2\theta - \zeta)]d\theta \int_0^T r\, dz \quad . \tag{5.5b}$$

These forces were then used to estimate the average force on the centered impeller and the stiffness forces caused by the impeller displacement so that,

$$\begin{Bmatrix} F^*_{ax} \\ F^*_{ay} \end{Bmatrix} = \begin{Bmatrix} \bar{F}_{ax} \\ \bar{F}_{ay} \end{Bmatrix} - \begin{bmatrix} K^*_{axx} & K^*_{axy} \\ K^*_{ayx} & K_{ayy} \end{bmatrix} \begin{Bmatrix} \varepsilon^* \cos\zeta \\ \varepsilon^* \sin\zeta \end{Bmatrix} \tag{5.6}$$

where,

$$\bar{F}_{ax} = (F^*_{ax}(0) + F^*_{ax}(90) + F^*_{ax}(180) + F^*_{ax}(270))/4 \quad ,$$

$$\bar{F}_{ay} = (F^*_{ay}(0) + F^*_{ay}(90) + F^*_{ay}(180) + F^*_{ay}(270))/4 \quad ,$$

and,

$$K^*_{axx} = (F^*_{ax}(0) - F^*_{ax}(180))/2\varepsilon^* \quad , \quad K^*_{axy} = (F^*_{ax}(90) - F^*_{ax}(270))/2\varepsilon^*$$

$$K^*_{ayx} = (F^*_{ay}(0) - F^*_{ay}(180))/2\varepsilon^* \quad , \quad K^*_{ayy} = (F^*_{ay}(90) - F^*_{ay}(270))/2\varepsilon^*$$

The results of this linearization are presented in Table 5.1, along with the combined pressure forces from the front shroud and the discharge of the impeller. Also included in this table are the direct force measurements made by Jery [17] and Chamieh [9]. It is evident from the results in Table 5.1 that the fluid trapped in the annular gap contributes significantly to the mean force and stiffness acting upon the impeller. With the rings installed, the mean force on the shroud was found to be near zero, but the hydrodynamic stiffness from the pressures in this region represent from about 50% to 75% of the total stiffness acting on the impeller. When the rings are removed, the mean forces on the shroud are no longer negligible at below design flowrates, and the stiffness is still modified substantially by the annular gap pressures. Table 5.1 also shows that the integrated pressure results are comparable with those obtained by the direct force measurements of Chamieh and Jery. It is believed that some of the differences that do exist can be attributed to the current inability to measure the pressures directly at

the impeller surface.

5.6 Apparent Limitations of the Theoretical Model

5.6.1 Lower limit on the flow coefficient

Up to this point the lowest flow coefficient used in the calculations has been 50% of the design flow rate. This lower limit might actually be considered a bit conservative, since the model does offer solutions all the way down to near shut-off conditions. One must be skeptical about the validity of the results below 30% of the design flow, because it is known that the assumption of no preswirl at the impeller inlet would not be valid. This can be established by simply watching through the lucite window of the test section as small bubbles spiral in towards the impeller inlet when the pump is being operated at low flow rates. Nevertheless, calculations were made at the lower flow rates for Impeller X in Volute A and, provided the results are viewed cautiously, they might prove to yield some insight into the operation of a pump.

When flow coefficients from $\phi = 0.02$ to $\phi = 0.05$ were investigated, it was found that the predicted perturbation in the impeller discharge flow never exceeded 6% of the mean flow and the flow path angle approached 87°. The theoretical and experimental forces that result over the extended range of flow rates are shown in Figure 5.17 and the stiffnesses are shown in Figure 5.18.

5.6.2 Upper limit on the flow coefficient

It was mentioned in Chapter 2 that different closure conditions at the tongue are possible (other than the matching total head condition that was used). When it was found that the total head matching assumption caused the model to fail at the above design flow coefficients, two other conditions were tested. In both attempts, the assumptions were

kept as simple as possible to avoid introducing new parameters into the problem. In the first investigation the velocity was equated from one side of the tongue to the other so that from the continuity equation,

$$\bar{V}(0) = 2\pi\phi/(\bar{A}(2\pi) - \bar{A}(0)) \quad , \tag{5.7}$$

and in the second investigation the pressure was matched across the tongue so that,

$$D_p(2\pi) = D_p(0) \quad . \tag{5.8}$$

Neither of these matching conditions produced results that predicted the pressure distributions as well as the head matching condition. Even at the above design conditions (where the original model failed) the two alternatives produced poor comparisons with the experimental results.

For the above design flow rates, it is possible that the one dimensional treatment of the volute flow fails to adequately model the velocity profile. Some indication of this can be found by comparing the measured pressure at the tongue of the volute to the total head at the discharge of the Volute A/Impeller X pump for $\phi = 0.10$. At this flow rate the pressure is found to be greater than what would be expected from the discharge total head ($P_v(R_t, 2\pi) = 0.77$ compared to $2\psi = 0.70$). Further, for flow rates greater than design, Lazarkiewicz and Troskolanski [20] indicate that eddys form at the tongue of the volute and that this results in a flow reversal through the tongue bypass. If this actually happens, then it is doubtful that any one dimensional model for the volute flow will produce reasonable results.

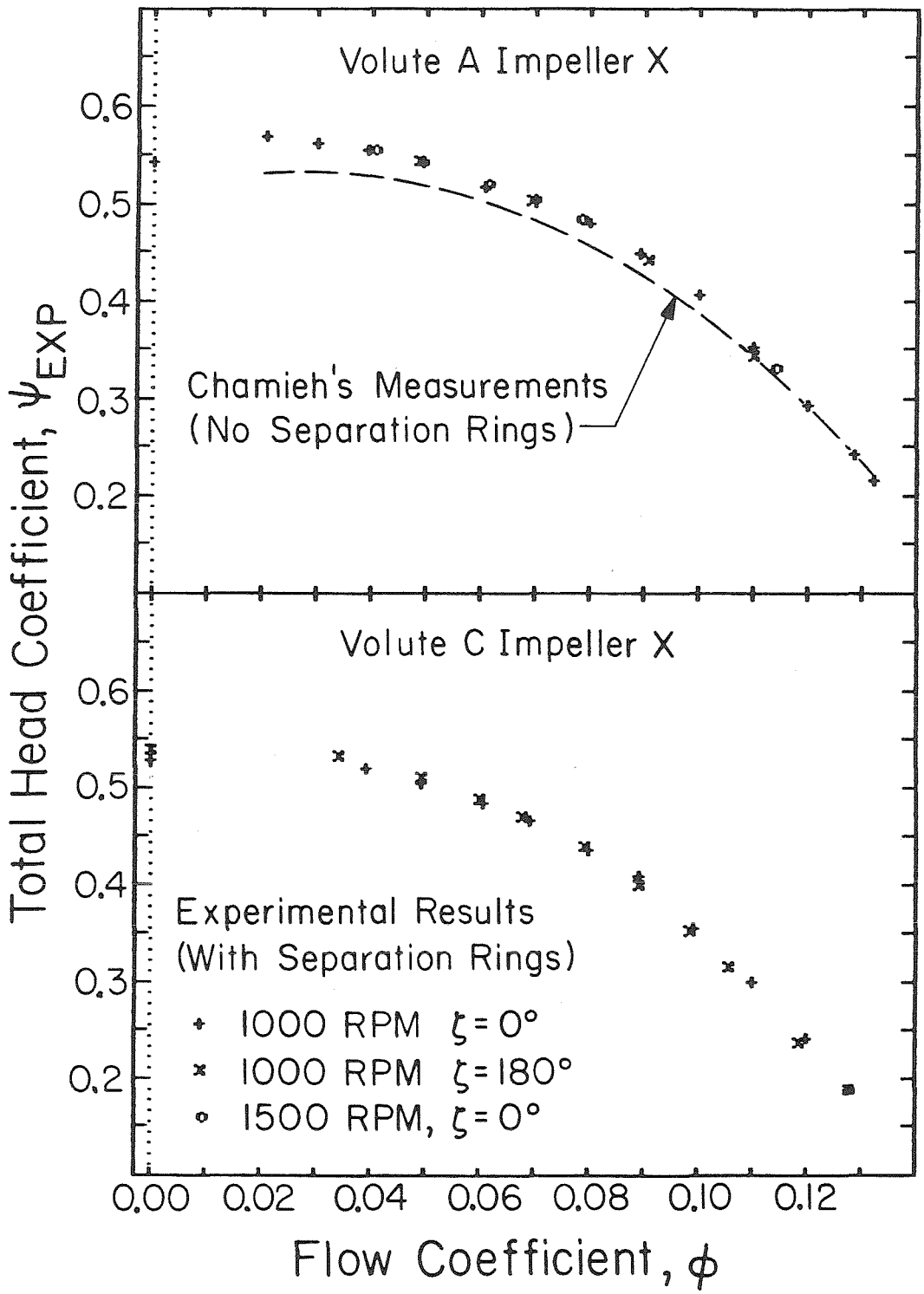

Figure 5.1 Effects of the impeller speed and position on the total head rise for Impeller X in Volute A and Volute C.

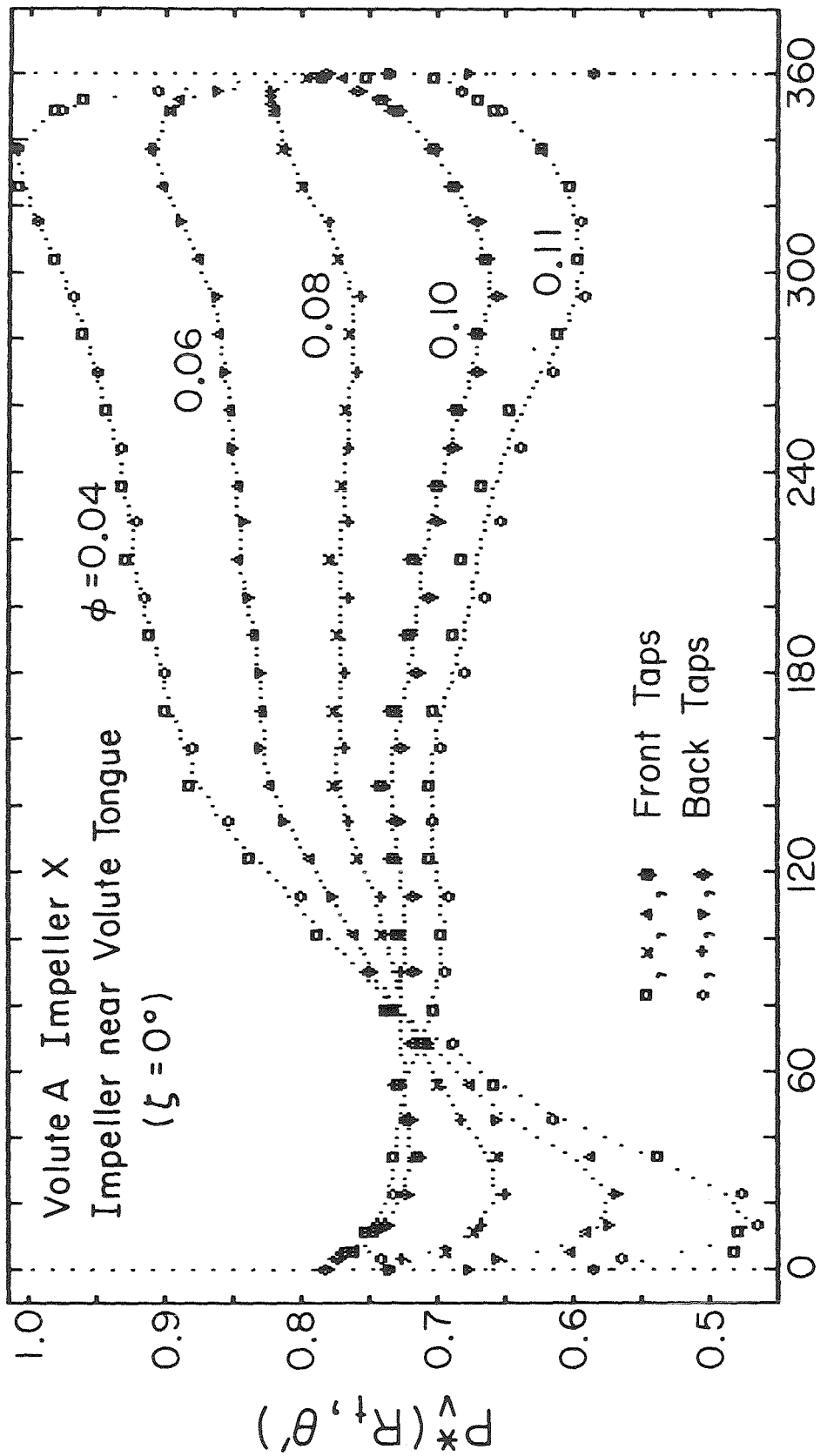

Figure 5.2 Measured pressure distributions around the pressure tap ring of Volute A, for various flow coefficients with Impeller X positioned near the tongue.

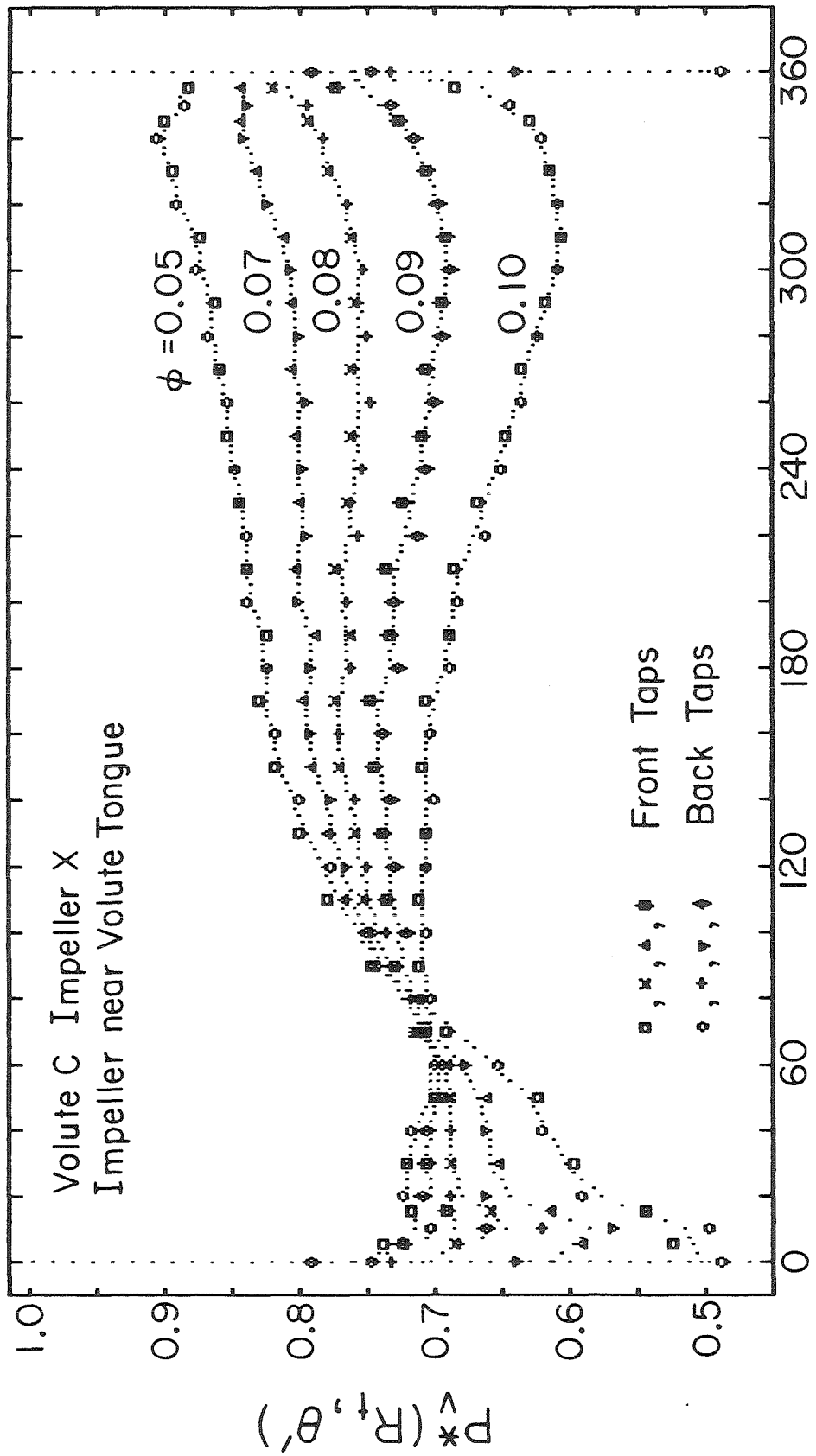

Figure 5.3 Measured pressure distributions around the pressure tap ring of Volute C, for various flow coefficients with Impeller X positioned near the tongue.

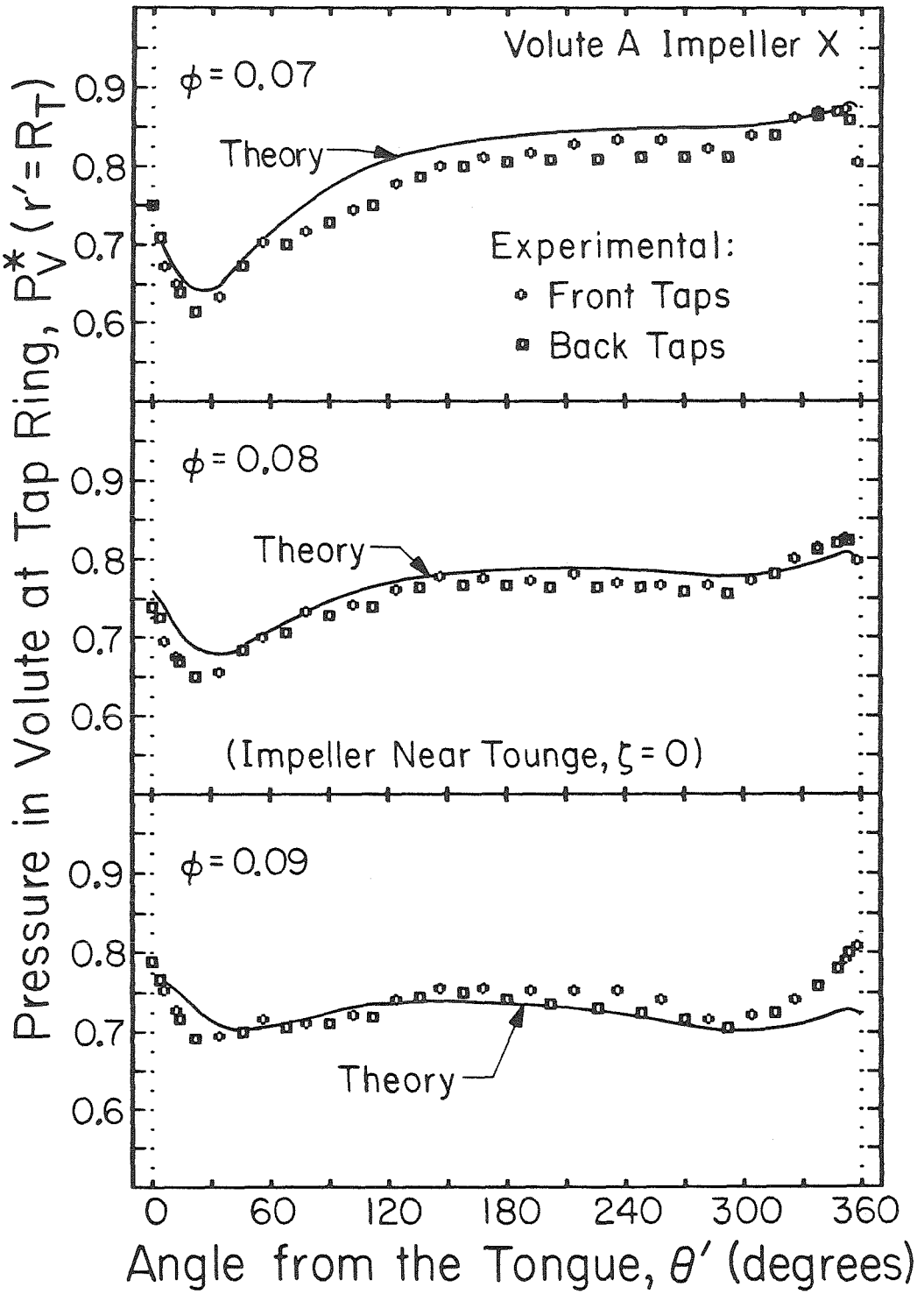

Figure 5.4 Experimental and theoretical pressure distributions around the pressure tap ring of Volute A, for three flow coefficients and Impeller X positioned near the tongue.

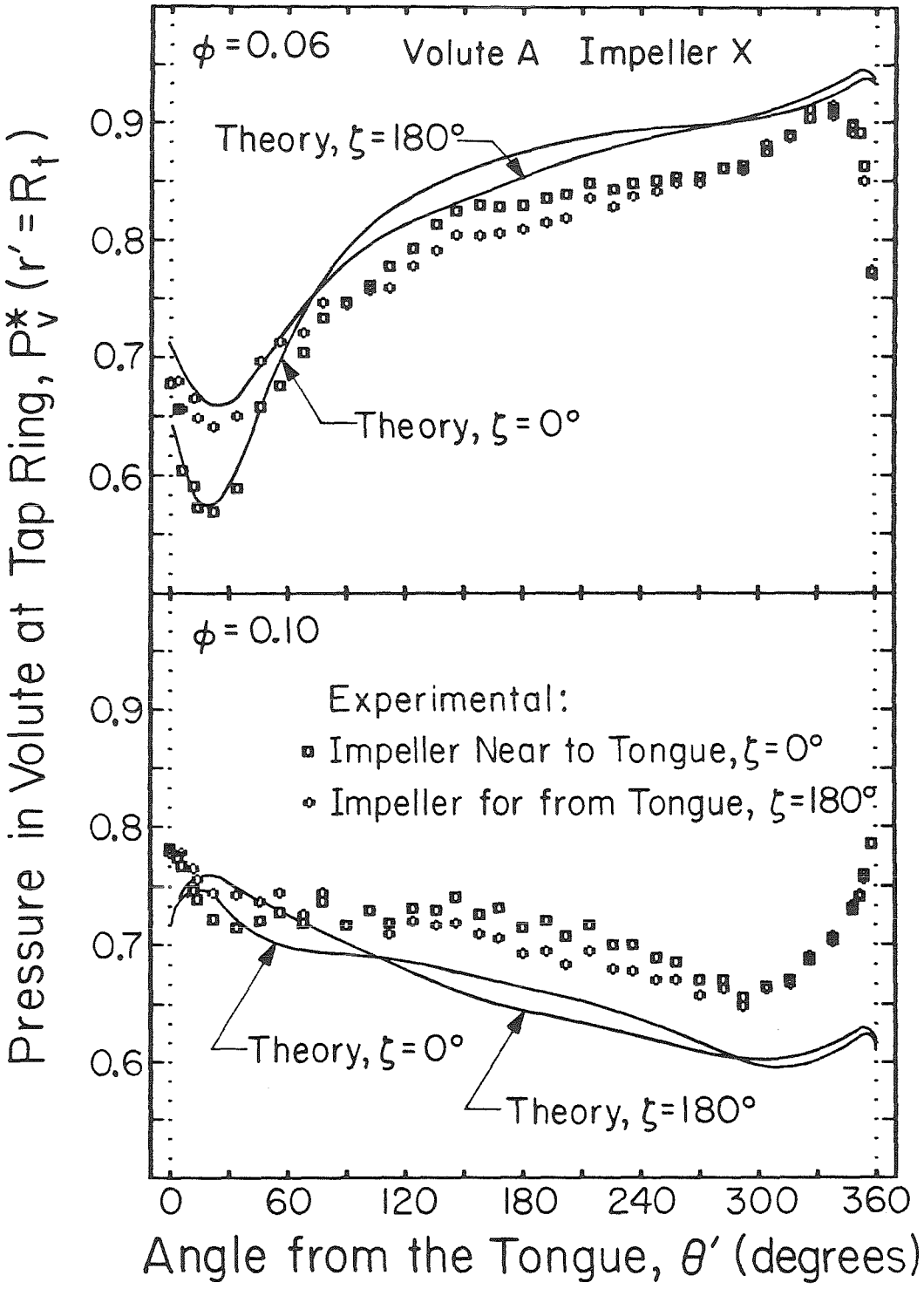

Figure 5.5 Effects of the impeller position on the pressure distributions around Volute A, for two flow rates with Impeller X near to ($\zeta = 0$) and far from ($\zeta = 180$) the tongue.

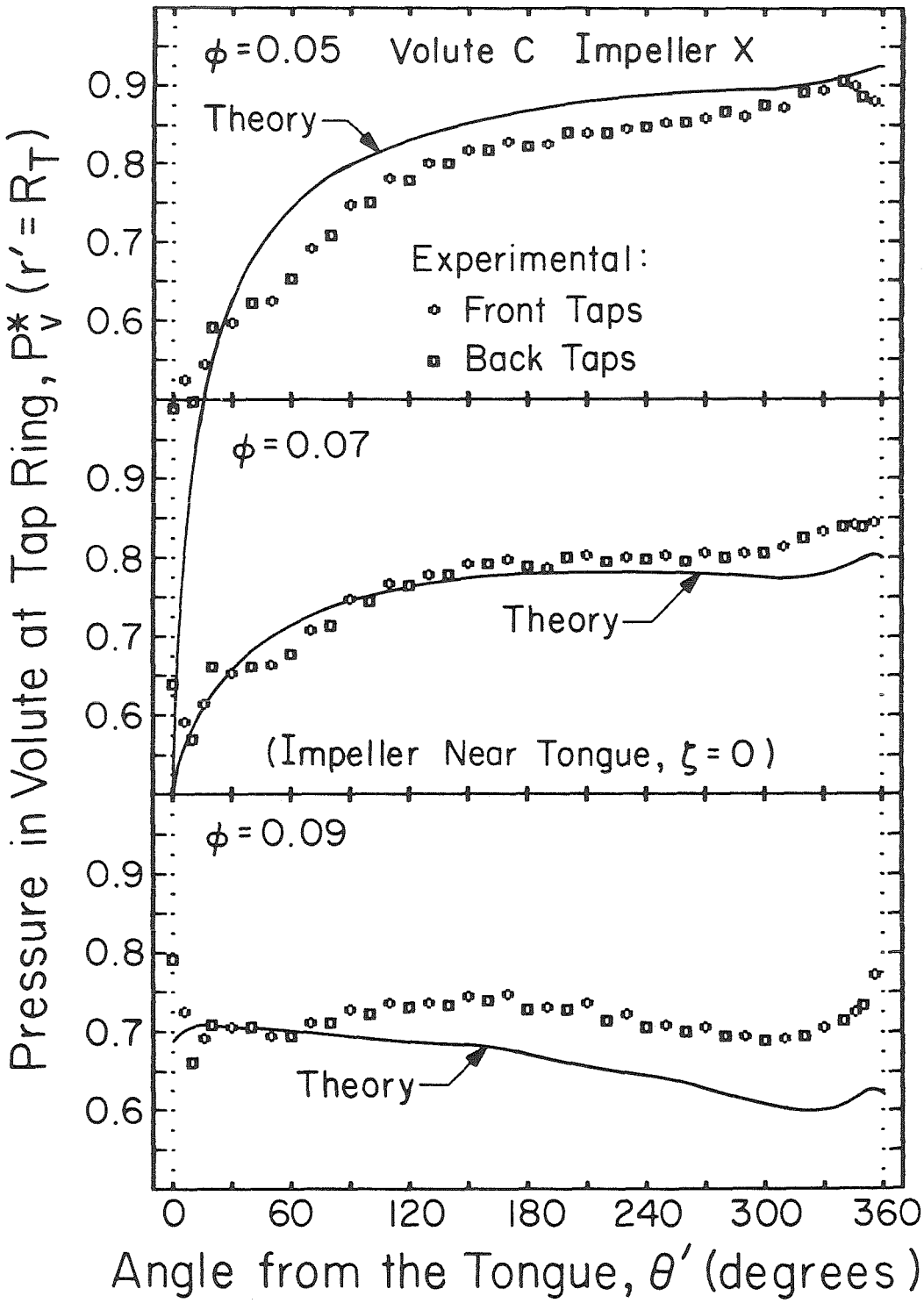

Figure 5.6 Experimental and theoretical pressure distributions around the pressure tap ring of Volute C, for three flow coefficients and Impeller X positioned near the tongue.

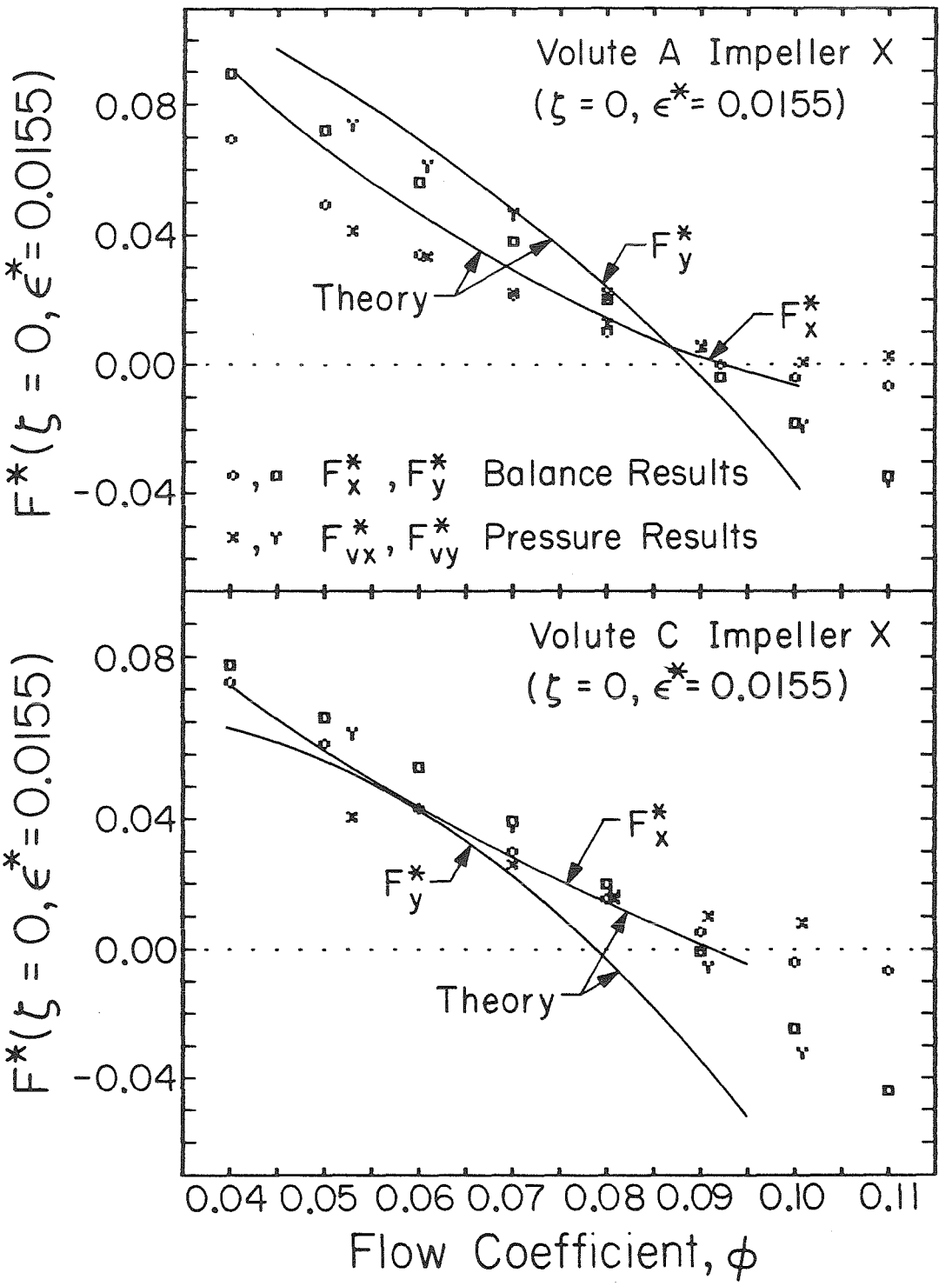

Figure 5.7 Radial forces on Impeller X when located near the tongue of either Volute A or Volute C from current theory, integrated pressures, and internal balance measurements.

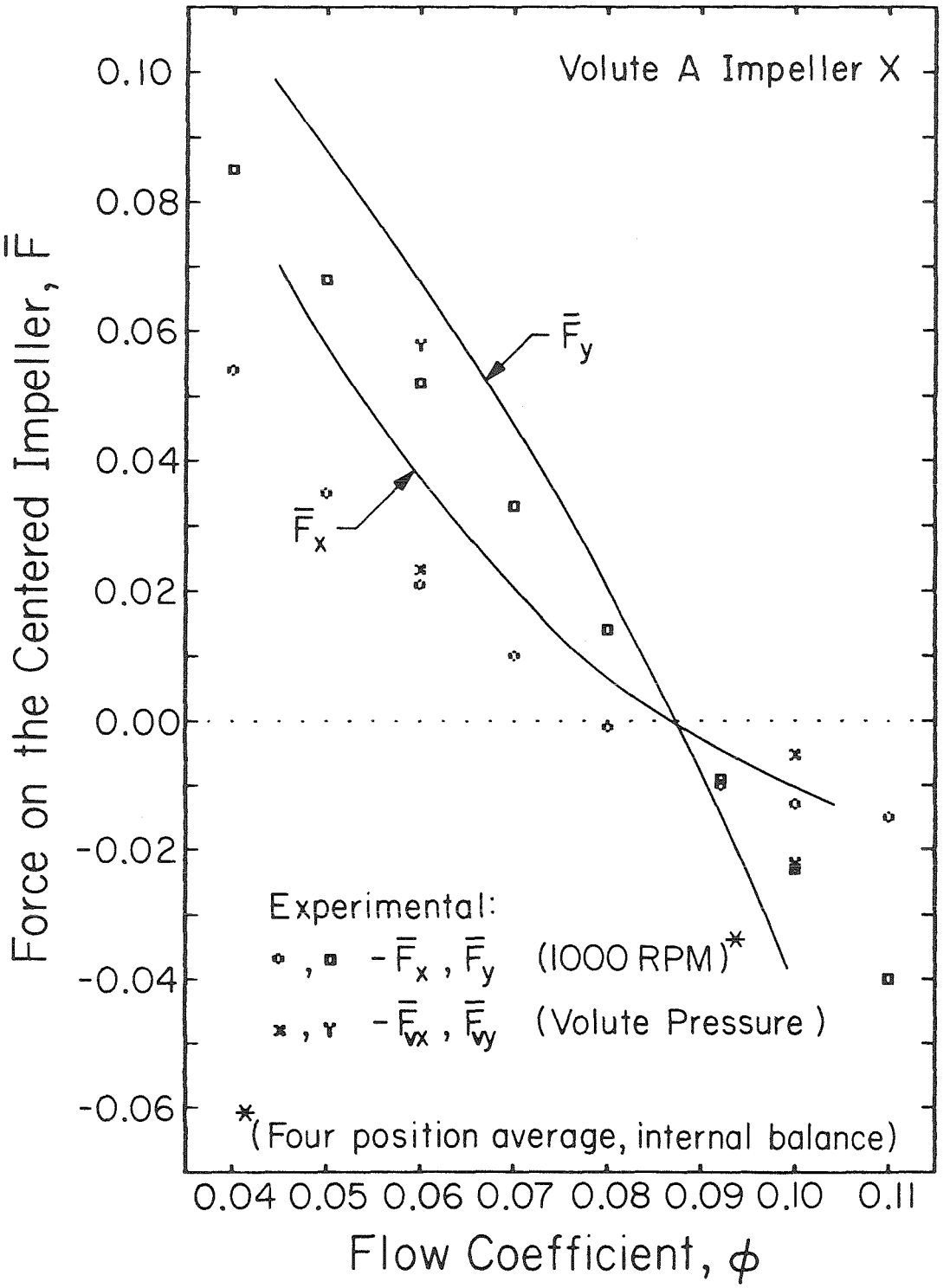

Figure 5.8 Experimental and theoretical radial forces on Impeller X positioned in the center of Volute A. Experimental results are a four position average ($\zeta = 0$, 90, 180, and 270).

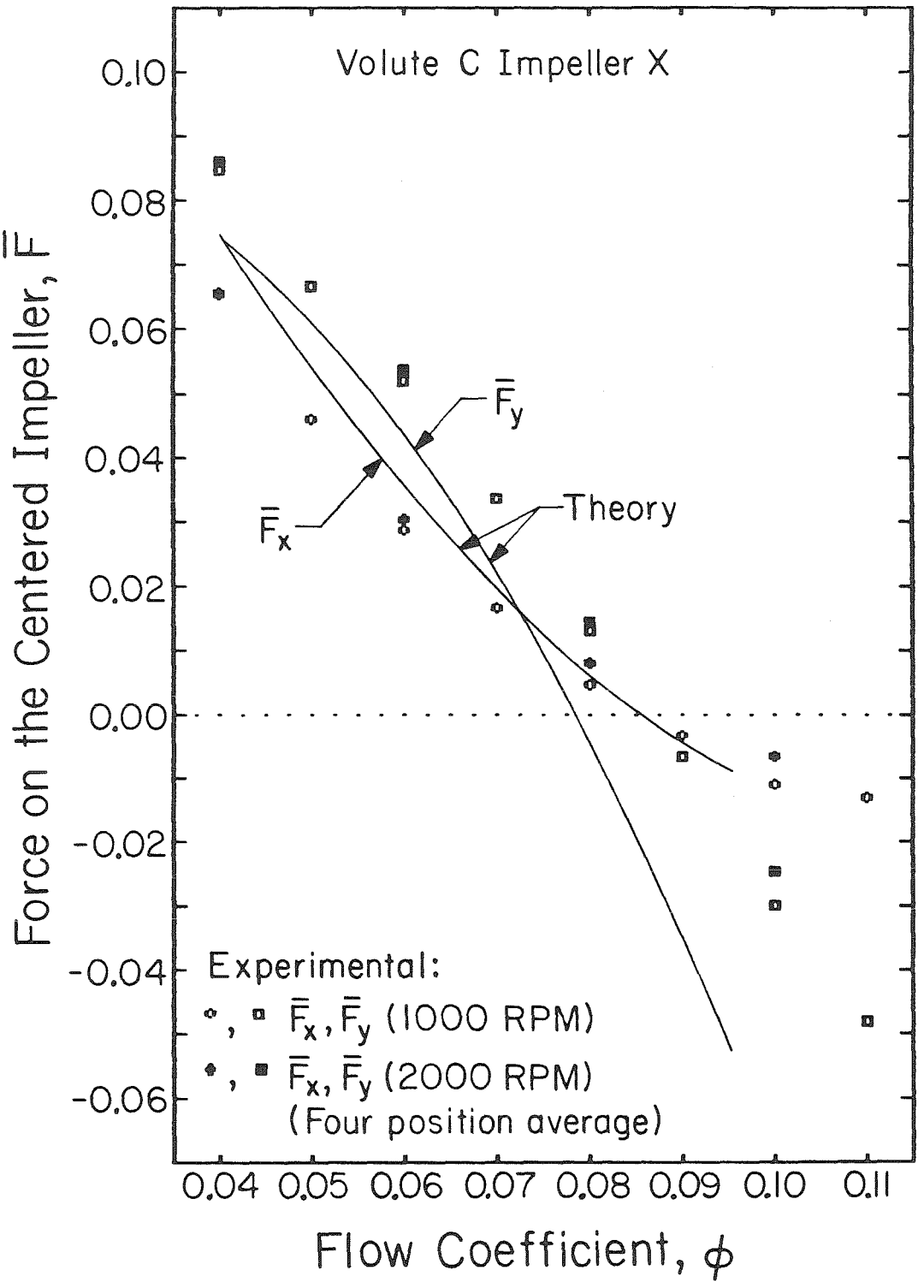

Figure 5.9 Experimental and theoretical radial forces on Impeller X positioned in the center of Volute C. Experimental results are a four position average ($\zeta = 0$, 90, 180, and 270).

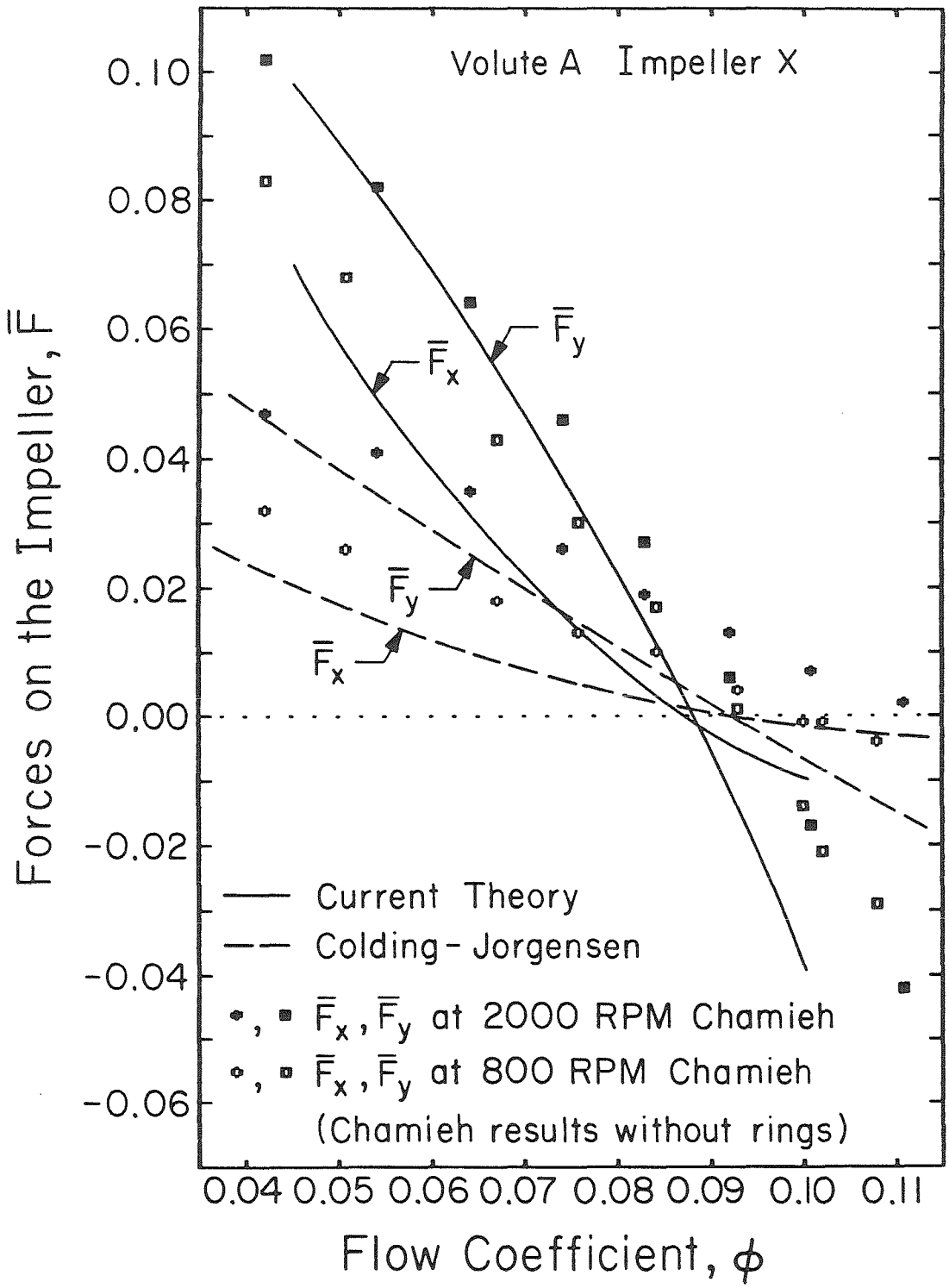

Figure 5.10 Comparison of current theoretical radial force predictions for a centered impeller to previous experiments and models. Chamieh [9] and current model use Volute A and Impeller X, while Colding-Jorgensen [12] results are for a volute angle of 86 .

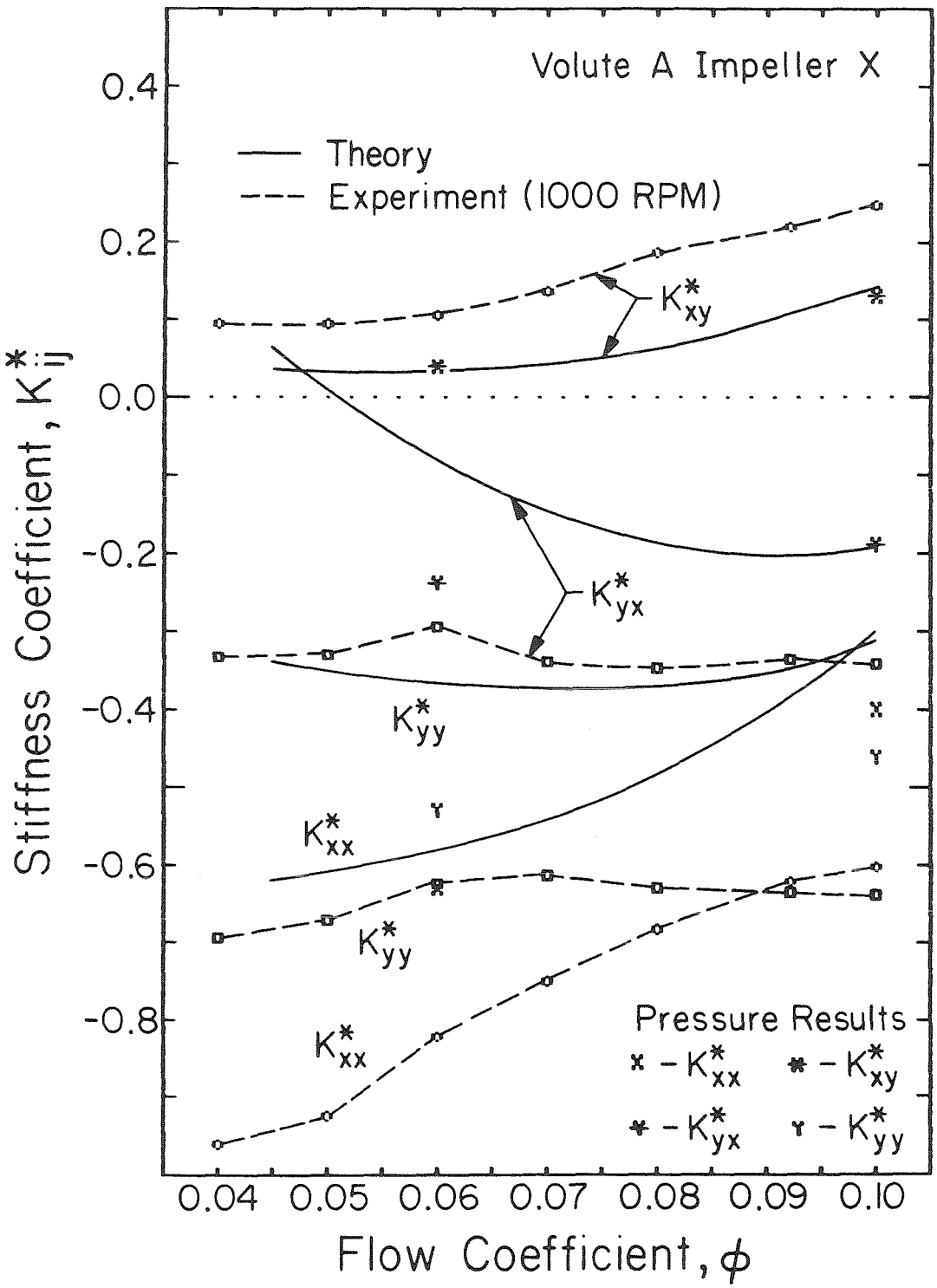

Figure 5.11 Theoretical and experimental stiffness coefficients as functions of flow coefficient for Impeller X in Volute A. Experimental results are based on a four position difference.

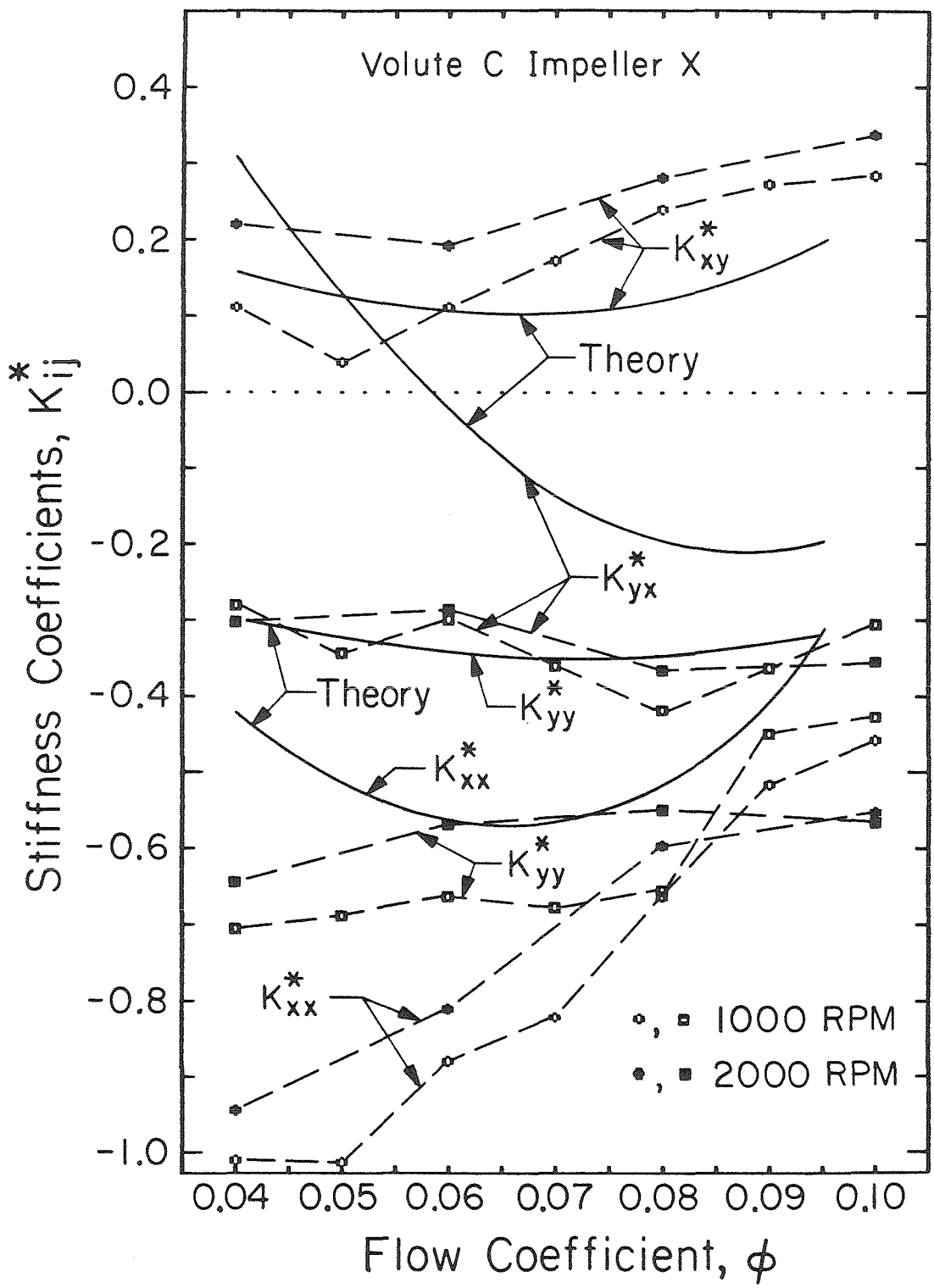

Figure 5.12 Theoretical and experimental stiffness coefficients as functions of flow coefficient for Impeller X in Volute C. Experimental results are based on a four position difference.

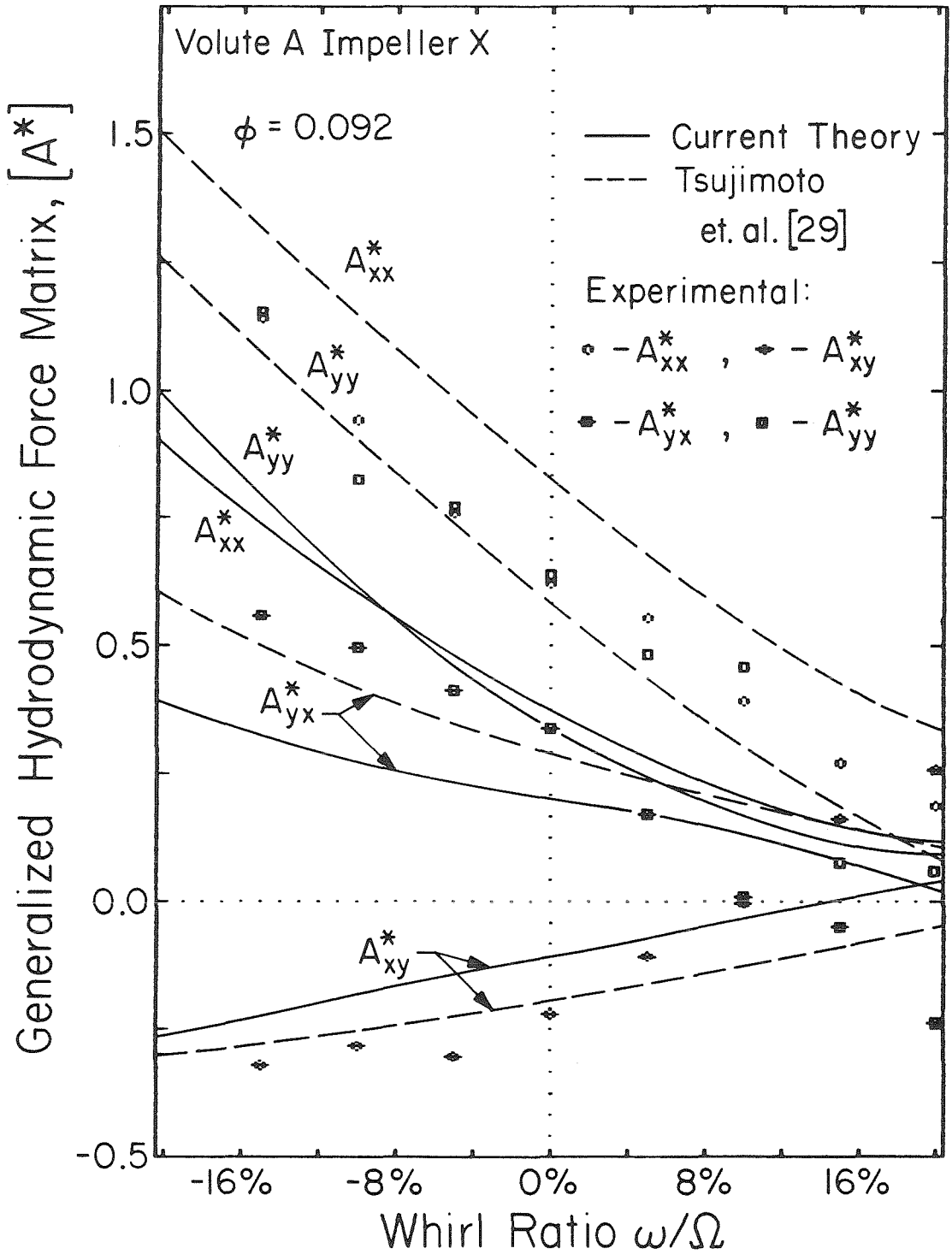

Figure 5.13 Theoretical and experimental coefficents for the generalized hydrodynamic force matrix as functions of whirl ratio for Impeller X in Volute A at the design flow rate.

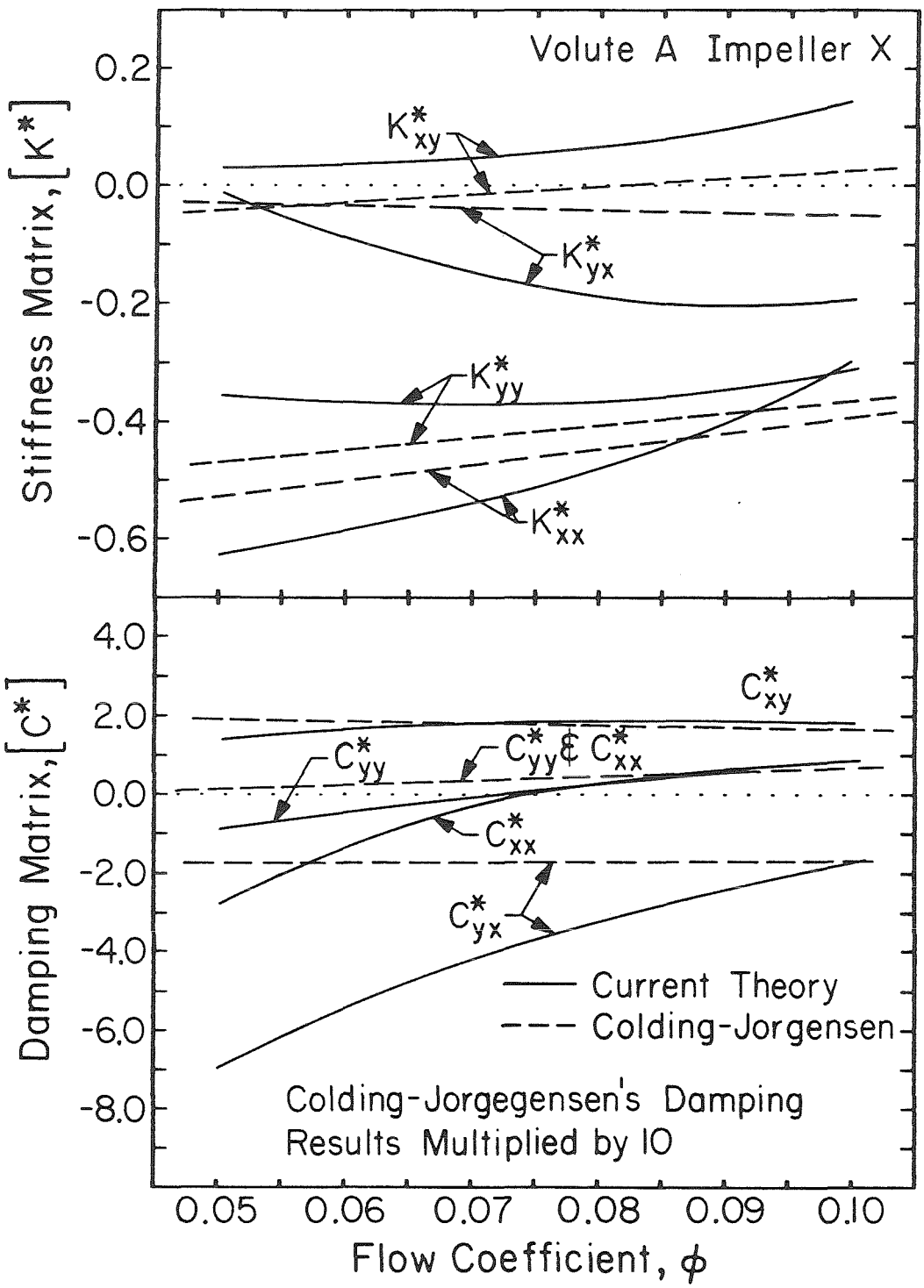

Figure 5.14 Comparison of stiffness and damping matrices predicted by current model for Impeller X in Volute A to those predicted by Colding-Jorgensen [12] for an 86 volute angle.

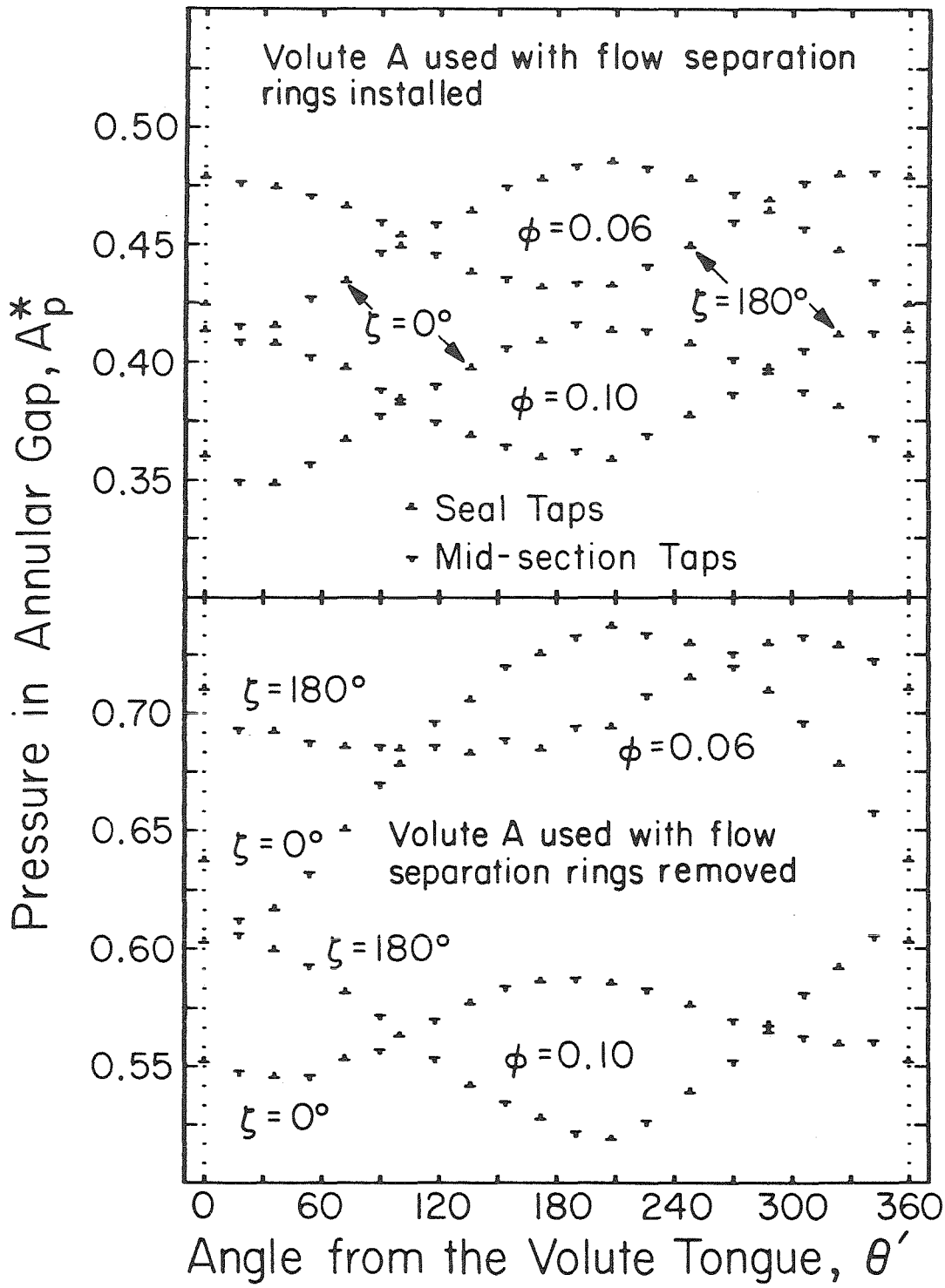

Figure 5.15 Pressure measurements from the annular gap between the front shroud of Impeller X and the original front flange for two impeller positions.

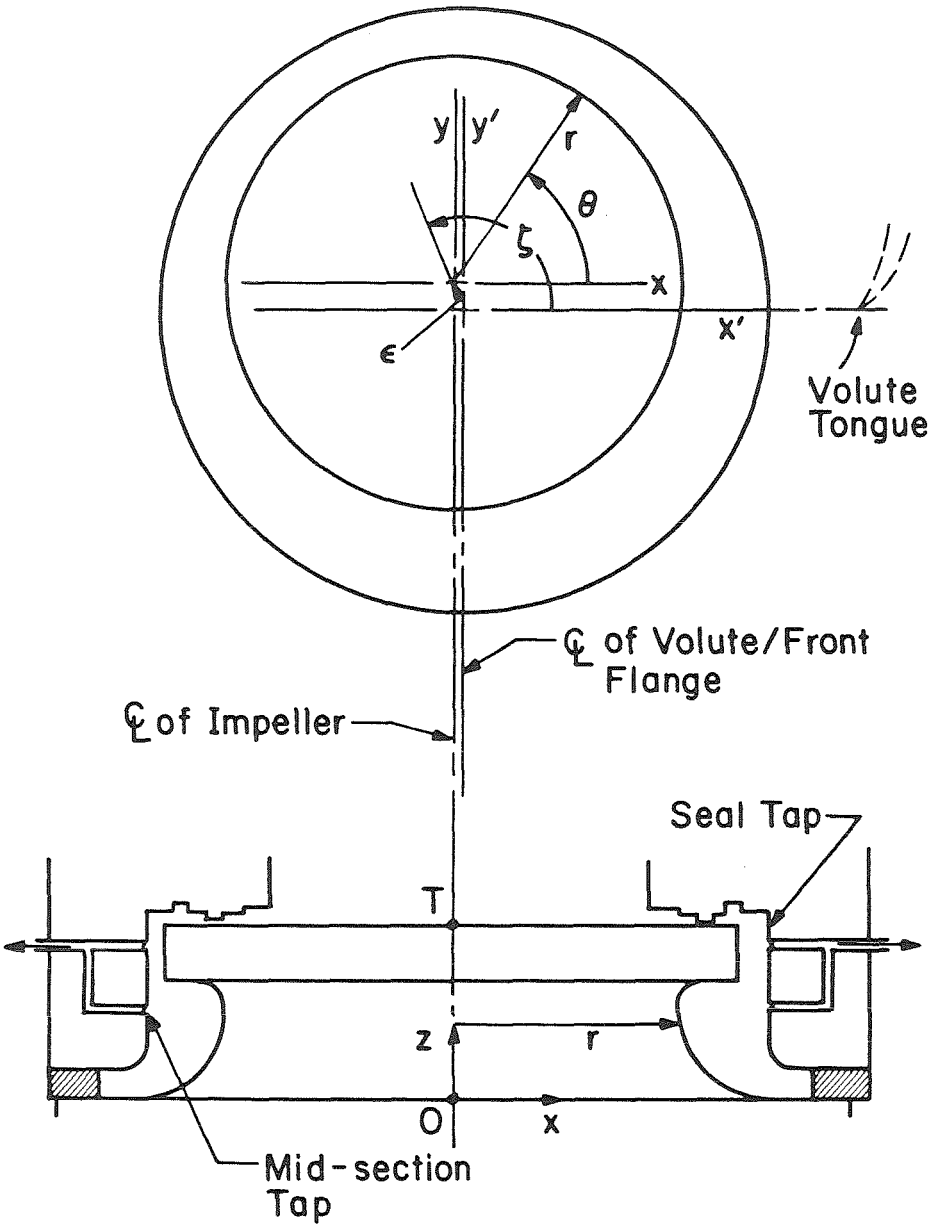

Figure 5.16 Geometry of the annular gap region.

Measurements with flow separation rings installed and unmodified front flange (Volute A, Impeller X)							Measurements with flow separation rings removed and unmodified front flange (Volute A, Impeller X)						
Pressure forces from Annular Gap Alone							Pressure forces from Annular Gap Alone						
ϕ	$\bar{F}_{ax}$	$\bar{F}_{ay}$	K^*_{axx}	K^*_{axy}	K^*_{ayx}	K^*_{ayy}	ϕ	$\bar{F}_{ax}$	$\bar{F}_{ay}$	K^*_{axx}	K^*_{axy}	K^*_{ayx}	K^*_{ayy}
0.06	-0.000	0.006	-1.42	+0.26	-0.35	-1.41	0.06	0.017	0.022	-1.63	0.37	-0.23	-1.54
0.10	-0.001	0.006	-1.41	+0.25	-0.35	-1.43	0.10	-0.009	-0.002	-1.60	0.31	-0.48	-1.62
Pressure forces from Annular Gap + Volute							Pressure forces from Annular Gap + Volute						
ϕ	$\bar{F}_x$	$\bar{F}_y$	K^*_{xx}	K^*_{xy}	K^*_{yx}	K^*_{yy}	ϕ	$\bar{F}_x$	$\bar{F}_y$	K^*_{xx}	K^*_{xy}	K^*_{yx}	K^*_{yy}
0.06	0.024	0.063	-2.05	0.30	-0.59	-1.94	0.06	0.011	0.046	-2.09	0.55	-0.79	-2.03
0.10	-0.006	-0.016	-1.81	0.38	-0.54	-1.89	0.10	0.000	-0.014	-1.98	0.51	-0.66	-2.00
Direct force measurements by Jery [17] (whirling impeller)							Direct force measurements by Chamieh [9]						
ϕ	$\bar{F}_x$	$\bar{F}_y$	K^*_{xx}	K^*_{xy}	K^*_{yx}	K^*_{yy}	ϕ	$\bar{F}_x$	$\bar{F}_y$	K^*_{xx}	K^*_{xy}	K^*_{yx}	K^*_{yy}
0.092	-	-	-1.63	0.86	-0.74	-1.47	0.06	0.027	0.055	-1.75	0.70	-0.75	-1.75
							0.10	0.008	-0.023	-2.05	0.85	-0.95	-2.20

TABLE 5.1 Volute and annular gap contributions to the forces on Impeller X with and without the flow separation rings installed in Volute A. Comparisons are made with the work of Chamieh [9] and Jery [17].

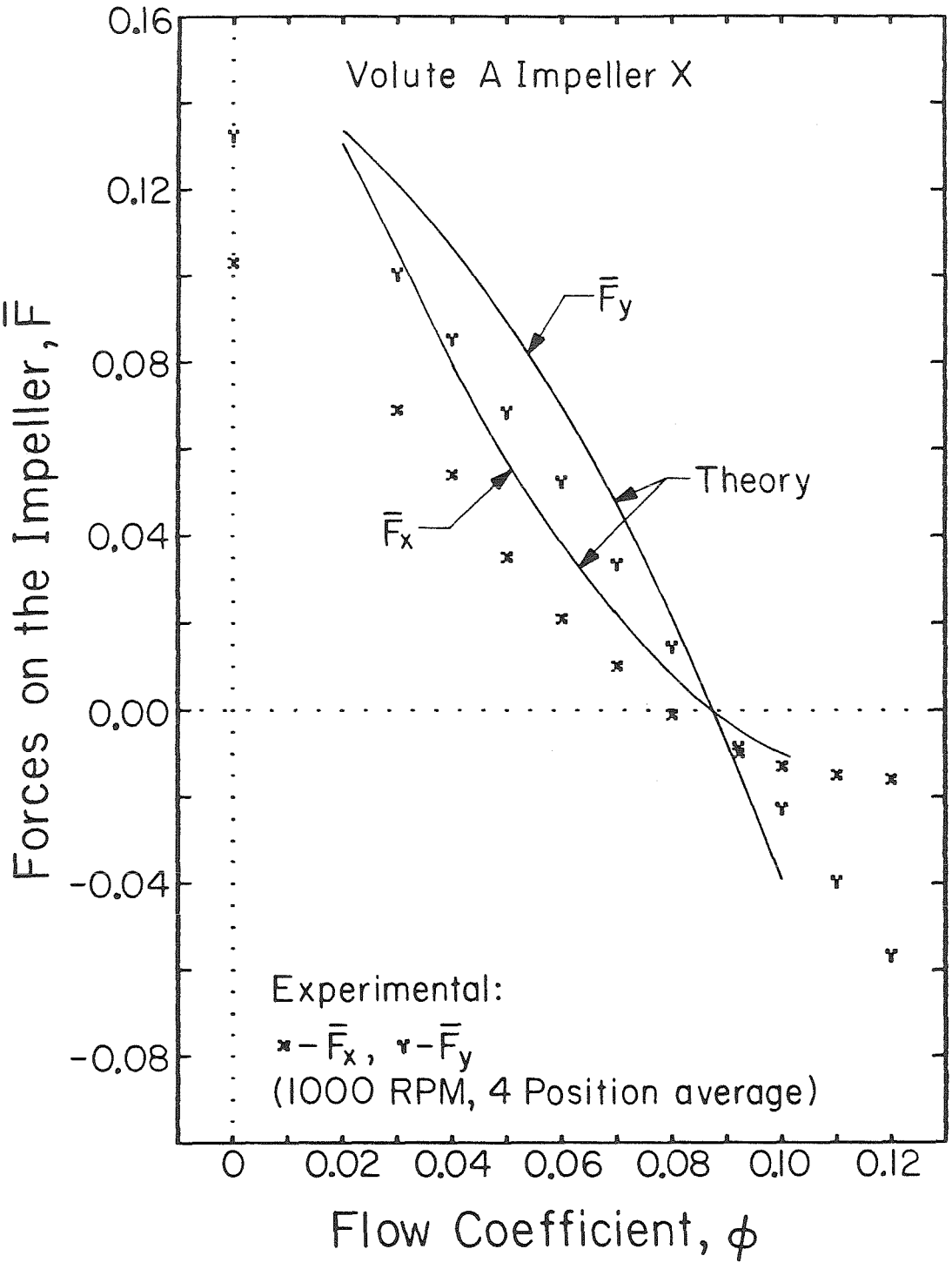

Figure 5.17 Radial forces on Impeller X in Volute A, theoretically calculated over a wide range of flow coefficients, and compared to experimental measurements.

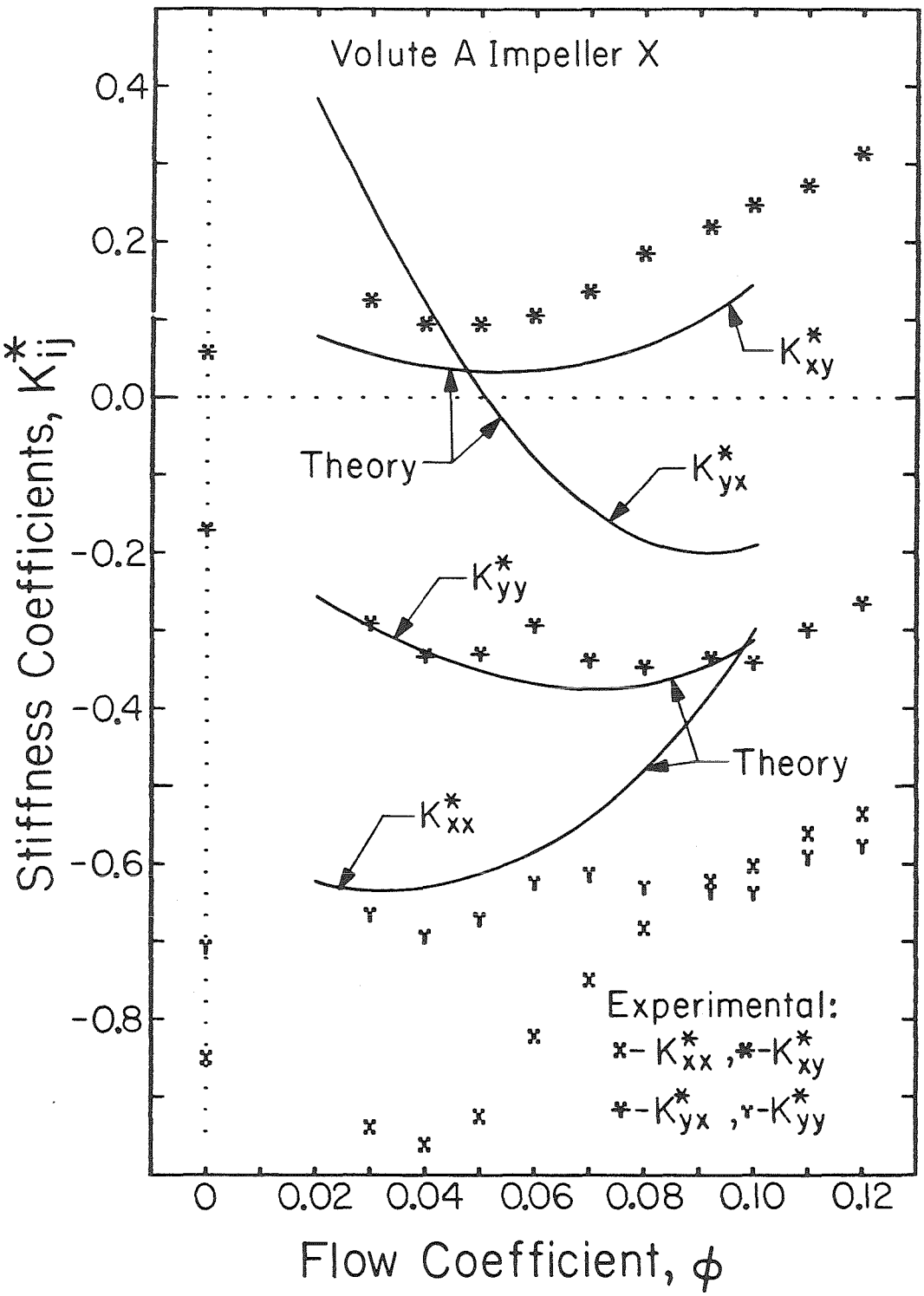

Figure 5.18 Stiffnesses for Impeller X in Volute A, theoretically calculated over a wide range of flow coefficients, and compared to experimental measurements.

Chapter 6

SUMMARY AND CONCLUSIONS

An investigation was undertaken to provide a theoretical understanding of the destablizing hydrodynamic forces that have been observed [10,17] on a whirling centrifugal pump impeller. The analytical model that was developed takes into account the interactions between the impeller and the surrounding volute. The impeller flow was assumed to follow a log spiral path (though not perfectly guided by the impeller blades) and have a periodic perturbation resulting from the discharge conditions imposed by the volute. Flow in the volute was considered to have a flat velocity profile across each cross section and satisfy the continuity and moment of momentum equations. Allowances were made for the radial variation of pressure in the volute and the recirculation of flow at the tongue. The need for empirical judgement was kept to a minimum, so that the model requires only the dimensions of the impeller and the volute and the total head rise across the pump. Calculations were performed for two situations: one with the impeller centrally located in the volute, and the other with the impeller whirling in an eccentric orbit.

What follows are the theoretical observations that were made for the centrally located impeller:

i) The presence of the volute causes at most a 6% circumferential perturbation to the impeller discharge velocity. This perturbation decreases as the flow rate approaches the volute design conditions.

ii) The flow is not perfectly guided through the impeller, but follows a path that varies with both flow rate and volute design.

iii) Flow recirculation at the tongue has a major influence on the pressure discontinuity in this region. For larger by-pass areas the pressure discontinuities are smaller, but this does not necessarily mean that the overall radial forces are smaller.

iv) Radial forces that occur on the impeller are primarily due to the asymmetric pressure distribution at the impeller discharge. Less than 1% of the force is due to asymmetries in the inlet pressure distribution or discharge momentum flux.

v) For flow rates above design, the one-dimensional volute flow model is inadequate in the region near the tongue.

For a small eccentric orbit of the impeller center, it was assumed that the flow properties could be linearized in terms of the steady (centered impeller) distributions and first order effects caused by the whirling motion. The findings of this analytical investigation of the whirling impeller are:

vi) The forces that result from an eccentric displacement of the impeller could induce or perpetuate impeller whirl over a wide range of flow rates.

vii) These forces are functions of the whirl speed of the impeller, but results were obtained only for whirl speeds equal to $\pm$ 15% of the impeller speed.

viii) The current model predicts a larger magnitude for the

hydrodynamic stiffness and damping coefficients than those predicted by Colding-Jorgensen [12].

Experimental tests were done in conjunction with the analytical work. The facility used for these tests have been utilized in previous experimental investigations [10,17], but slight modifications have been made for the current analysis. The following results were obtained from these tests:

ix) The pressure distribution at the impeller discharge is the major cause of the radial forces in the volute/impeller interaction.

x) Agreement with theoretical predictions for the forces on a centered impeller is fair, but the model tends to overpredict the magnitude of the force.

xi) The hydrodynamic forces vary with the square of the impeller speed.

xii) The measured hydrodynamic stiffnesses were only about one fourth the size of those obtained by Chamieh et al.[10] and Jery et al. [17]. This difference is attributed to a modification of the test section that gives a uniform pressure distribution on the front shroud of the impeller in the current experiments. The stiffnesses are still such that they would encourage the impeller to whirl as was previously observed by Chamieh and Jery.

xiii) The theoretical analysis predicts some of the trends demonstrated in the experimental stiffness results, but some questions still remain about the cross coupling effects of the stiffnesses.

xiv) A reasonably good comparison is obtained between the theoretical and experimental forces that result from the impeller whirling in the volute. This observation is, however, based on a limited range of data.

xv) Pressure measurements have shown that hydrodynamic forces on the front shroud of the impeller have a larger contribution to the stiffnesses (50% - 75% of total) than the impeller/volute interaction forces. These forces in combination with the volute pressure forces compare well with the direct measurements of [10] and [17].

A major advantage that this theoretical approach has over other analyses, is that by using the actual geometry of the volute it provides a more physical interpretation of what happens inside of the centrifugal pump. With some modifications, it might be possible in the future to extend the model to include the effects of an inducer at the inlet of the impeller and vanes at the inlet of the volute. This would be an important improvement in the model since many of today's high performance pumps use inducers and diffuser vanes.

The analytical model does give reasonable estimates for the pressure distributions and the hydrodynamic forces, although there are limitations on the range of flow rates and whirling speeds. The present theory could perhaps be extended to higher whirl rates, but it is unlikely that the flow near the volute tongue will ever be adequately described by a simple one dimensional treatment for the above design flow rates. It is possible that an improvement in the model might be achieved by incorporating a two dimensional treatment of the flow near the tongue. Even with no improvement, the predictions of the model could be more crucially tested

by investigating a volute where the tongue bypass area is much larger than those used in this study.

Finally, it should be emphasized that this model alone will not account for all of the hydrodynamic forces that act on the centrifugal pump impeller. It was shown by the experimental analysis in this research that principal influence on the hydrodynamic stiffnesses was contributed by the fluid interactions with the front shroud of the impeller. This is definitely an area that deserves more attention.

REFERENCES

1. Agostinelli, A., Nobles, D., and Mockridge, C.R., "An Experimental Investigation of Radial Thrust in Centrifugal Pumps", Trans. ASME, J. of Engr. for Power, Vol. 82, pp. 120-126, April 1960.

2. Black, H.F., and Jenssen, D.N., "Effects of High-Pressure Ring Seals on Pump Rotor Vibrations", ASME Paper No. 71-WA/FF-38, 1971.

3. Binder, R.C., and Knapp, R.T., "Experimental Determinations of the Flow Characteristics in the Volutes of Centrifugal Pumps", Trans. ASME, Vol. 58, pp. 649-661, 1936.

4. Bolleter, U., and Wyss, A., "Measurement of Hydrodynamic Interaction Matrices of Boiler Feed Pump Impellers", Presented at ASME Design Engineering Divsion Conference and Exhibit on Mechanical Vibration and Noise, Cincinnati OH, Sept. 10-13, 1985.

5. Bowerman, R.D., and Acosta, A.J., "Effect of the Volute on Performance of a Centrifugal Pump Impeller", Trans. ASME, Vol. 79, pp. 1057-1069, July 1957.

6. Braisted, D.M., "Cavitation Induced Instabilities Associated with Turbomachines", Ph.D. Thesis, Division of Engineering and Applied Sciences, California Institute of Technology, 1979.

7. Brennen, C.E., Acosta, A.J., and Caughey, T.K., "A Test Program to Measure Fluid Mechanical Whirl-Excitation Forces in Centrifugal Pumps", First Workshop on Rotordynamic Instability Problems in High Performance Turbomachinery, Texas A&M University, NASA Conf. Pub. 2133, pp. 229-235, 1980.

8. Busemann, A., "Das Forderhohenverhaltniss radialer Kreisel- pumpen mit logarithmischspiraligen Schaufeln", Zeitschrift fur Angewandte Mathematik und Mechanik, Vol. 8, pp. 372-384, 1928.

9. Chamieh, D.S., "Forces On A Whirling Centrifugal Pump-Impeller", Ph.D. Thesis, Division of Engineering and Applied Sciences, California Institute of Technology, 1983.

10. Chamieh, D.S., Acosta, A.J., Brennen, C.E., Caughey, T.K., and Franz, R., "Experimental Measurements of Hydrodynamic Stiffness Matrices for a Centrifugal Pump Impeller", 2nd Workshop on Rotordynamic Instability Problems in High Performance Turbomachinery, Texas A&M University, NASA Conf. Pub. 2250, pp. 382-398, May 10-12, 1982.

11. Childs, D.W., "Finite Length Solutions for Rotordynamic Coefficients of Turbulent Annular Seals", ASME J. of Lubrication Technology, Vol. 105, pp. 437-444, July 1983.

12. Colding-Jorgensen, J., "The Effect of Fluid Forces on Rotor Stability of Centrifugal Compressors and Pumps", First Workshop on Rotordynamic Instability Problems in High Performance Turbomachinery, Texas A&M University, NASA Conf. Pub. 2133, pp. 249- 266, May 12-14, 1980.

13. Csanady, G.T., "Radial Forces in a Pump Caused by Volute Casing", Trans. ASME, J. of Engr. for Power, Vol. 84, pp. 337-340, October 1962.

14. Ehrich, F., and Childs, D., "Self-Excited Vibration in High Performance Turbomachinery", Mech. Engr., Vol. 106, No. 5, pp. 66-79, May 1984.

15. Iversen, H.W., Rolling, R.E., and Carlson, J.J., "Volute Pressure Distribution, Radial Force on the Impeller and Volute Mixing Losses of a Radial Flow Centrifugal Pump", Trans. ASME, J. of Engr. for Power, Vol. 82, pp. 136-144, April 1960.

16. Jery, B. "Experimental Study of Unsteady Hydrodynamic Force Matrices on Whirling Centrifugal Pump-Impellers", Ph.D. Thesis, Division of Engineering and Applied Sciences, California Institute of Technology, 1986.

17. Jery, B., Acosta, A.J., Brennen, C.E., and Caughey, T.K., "Hydrodynamic Impeller Stiffness, Damping and Inertia in the Rotordynamics of Centrifugal Flow Pumps", Rotordynamic Instability Problems in High Performance Turbomachinery, Texas A&M University, NASA Conf. Pub. 2338, pp. 137-160, May 28-30, 1984.

18. Knapp, R.T., "Centrifugal-Pump Performance as Affected by Design Features", Trans. ASME, Vol. 63, pp. 251-260, 1941.

19. Kurokawa, J., "Theoretical Determinations of the Flow Characteristics in Volutes", IAHR/AIRH Symposium, Tokyo, Japan, pp. 623- 634, 1980.

20. Lazarkiewicz, S., and Troskolanski, A.T., "Impeller Pumps", Pergamon Press, Translated by D.K. Rutter (Polish Ed. Title: Pompy Wirowe), 1965.

21. Loret, G., and Gopalakrishnan, S., "Interaction Between Impeller and Volute of Pumps at Off-Design Conditions", Performance of Hydraulic Turbines and Pumps, ASME Winter Annual Meeting, FED, Vol.6, Nov. 1983.

22. Ng, S.L., "Dynamic Response of Cavitating Turbomachines", Ph.D. Thesis, Division of Engineering and Applied Sciences, California Institute of Technology, 1976.

23. Ohashi, H., and Shoji, H., "Lateral Fluid Forces Acting on a Whirling Centrifugal Impeller in Vaneless and Vaned Diffuser", Rotordynamic Instability Problems in High Performance Turbomachinery, Texas A&M University, NASA Conf. Pub. 2338, pp. 109-122, May 28-30, 1984.

24. Shoji, H., and Ohashi, H., "Fluid Forces on Rotating Centrifugal Impeller with Whirling Motion", First Workshop on Rotordynamic Instability Problems in High Performance Turbomachinery, Texas A&M University, NASA Conf. Pub. 2133, pp. 317-328, 1980.

25. Stepanoff, A.J., "Centrifugal and Axial Flow Pumps", 2nd Edition, Wiley, New York, 1957.

26. Streeter, V.L., and Wylie, E.B., "Fluid Mechanics", 6th ed., McGraw-Hill Book Co., New York, 1975.

27. Stodola, A., "Steam and Gas Turbines", McGraw-Hill Book Co., New York, 1927.

28. Tsujimoto, Y., Acosta, A.J., and Brennen, C.E., "Two-Dimensional Unsteady Analysis of Fluid Forces on a Whirling Centrifugal Impeller in a Volute", Rotordynamic Instability Problems in High Performance Turbomachinery, Texas A&M University, NASA Conf. Pub. 2338, pp. 161-171, May 28-30, 1984.

29. Tsujimoto, Y., personal correspondence on future paper-- "Theoretical Study of Fluid Forces on a Centrifugal Impeller Rotating and Whirling in a Volute", July 1985.

30. Weisner, F.J., "A Review of Slip Factors for Centrifugal Impellers", ASME Trans., J. of Engr. for Power, Vol. 89, pp. 558-566, October 1967.

APPENDIX A

DERIVATION OF GOVERNING EQUATIONS FOR A WHIRLING IMPELLER

A.1 Introduction

Bernoulli's equation is used to relate the velocities and pressures between the inlet and the exit of the impeller. A brief derivation of the form of Bernoulli's equation used is presented in this appendix to alleviate any suspicion as to the origin of some of the terms. In addition, the equation used in finding the momentum flux contribution to the forces on the impeller is developed. Frictional forces will be neglected and the flow through the impeller will be considered to be two dimensional. The impeller is both spinning and whirling at constant rotational speeds.

A.2 Bernoulli's Equation

Figure A.1 defines the coordinate systems to be used. With the frictional forces ignored, the equilibrium of forces in the streamwise direction on a differential element ds"dn" requires that,

$$(P_i - \frac{\partial P_i}{\partial s''} ds''/2)dn'' - (P_i + \frac{\partial P_i}{\partial s''} ds''/2)dn'' = \rho\, ds''dn''a_{s''} \quad ,$$

or,

$$a_{s''} = -\frac{1}{\rho} \frac{\partial P_i}{\partial s''} \quad . \tag{A.1}$$

When viewed from the rotating reference frame, the absolute acceleration of the differential fluid element is given by,

$$\underset{\sim}{a} = \frac{D\underset{\sim}{v}_{r''\theta''}}{Dt} + \underset{\sim}{a}_{x''y''} + 2\underset{\sim}{\Omega} \times \underset{\sim}{v}_{r''\theta''} + \underset{\sim}{\Omega} \times (\underset{\sim}{\Omega} \times \underset{\sim}{r}) \quad , \tag{A.2}$$

where,

$$\underset{\sim}{v}_{r''\theta''} = v_{r''}\, \underset{\sim}{e}_{r''} + v_{\theta''}\, \underset{\sim}{e}_{\theta''} = v\, \underset{\sim}{e}_{s''} \quad ,$$

$$\underset{\sim}{a}_{x''y''axis} = -\omega^2 \varepsilon [\cos(\omega t - \Omega t - \theta'')\underset{\sim}{e}_{r''} + \sin(\omega t - \Omega t - \theta'')\underset{\sim}{e}_{\theta''}] \quad ,$$

$$\underset{\sim}{\Omega} = \Omega \underset{\sim}{e}_{z''} \quad ,$$

and,

$$\frac{D\underset{\sim}{v}_{r''\theta''}}{Dt} = \left(\frac{\partial v}{\partial t} + v\,\frac{\partial v}{\partial s''}\right) \underset{\sim}{e}_{s''} + \left(\frac{\partial v_\eta}{\partial t} - \frac{vv}{Cr}\right)\underset{\sim}{e}_{\eta''} \quad .$$

The Cr appearing in the acceleration is the instantaneous radius of curvature of the fluid elements path (notice that it is the streamwise acceleration that is used so the Cr term will present no problem).

To find the acceleration component in the streamwise direction, the following identity relating the r", θ" and the s",n" systems is used,

$$\underset{\sim}{e}_{r''} = \frac{dr''}{ds''}\,\underset{\sim}{e}_{s''} - \frac{r''d\theta''}{ds''}\,\underset{\sim}{e}_{\eta''} = \frac{v_{r''}}{v}\,\underset{\sim}{e}_{s''} - \frac{v_{\theta''}}{v}\,\underset{\sim}{e}_{\eta''} \quad , \tag{A.3a}$$

$$\underset{\sim}{e}_{\theta''} = \frac{r''d\theta''}{ds''}\,\underset{\sim}{e}_{s''} + \frac{dr''}{ds''}\,\underset{\sim}{e}_{\eta''} = \frac{v_{\theta''}}{v}\,\underset{\sim}{e}_{s''} + \frac{v_{r''}}{v}\,\underset{\sim}{e}_{\eta''} \quad , \tag{A.3b}$$

along with the definition of the tangential acceleration,

$$a_{s''} = \underset{\sim}{a} \cdot \underset{\sim}{e}_{s''} \quad .$$

Using these relationships and integrating along a streamline gives the desired form of Bernoulli's equation as,

$$\frac{P_i}{\rho} + \frac{v^2}{2} - \frac{\Omega^2 r''^2}{2} + \int_{s''} \frac{\partial v}{\partial t}\, ds''$$

(continued)

$$-\omega^2\varepsilon\left[\begin{array}{l}\int_{s''}\cos(\omega t-\Omega t-\theta'')dr'' \\ +\int_{s''}\sin(\omega t-\Omega t-\theta'')r''d\theta''\end{array}\right]=F(t)\quad,\qquad(A.5)$$

where F(t) is a function only of time but may vary from one streamline to another.

A.3 Momentum Force Equation

What is referred to here as the momentum force equation is actually an expression which combines the impeller force contributions of the momentum flux terms and the body forces. The momentum force of the fluid acting on the impeller may be written as,

$$\underset{\sim}{F}_m=-\frac{\partial}{\partial t}\int_{cv}\rho\underset{\sim}{V}_{r''\theta''}\,d\forall-\int_{cs}\rho\underset{\sim}{V}_{r''\theta''}\,\underset{\sim}{V}_{r''\theta''}\cdot d\underset{\sim}{A}$$

$$-\int_{cv}\rho[\underset{\sim}{a}_{x''y''axis}+2\underset{\sim}{\Omega}\times\underset{\sim}{V}_{r''\theta''}+\underset{\sim}{\Omega}\times(\underset{\sim}{\Omega}\times\underset{\sim}{r})+\dot{\underset{\sim}{\Omega}}\times\underset{\sim}{r}]d\forall\quad.\qquad(A.6)$$

The control volume in this expression is the fluid in the impeller blade passages between R_1 and R_2 . When the velocities and the accelerations used in the development of Bernoulli's equation are incorporated into this equation, it becomes,

$$\frac{\underset{\sim}{F}_m}{\rho b}=\frac{(F_x+jF_y)}{\rho b}=-e^{j\Omega t}\frac{\partial}{\partial t}\int_0^{2\pi}\int_{R_1}^{R_2}(v_{r''}+jv_{\theta''})e^{j\theta''}r''dr''d\theta''$$

$$-e^{j\Omega t}\left[\int_0^{2\pi}(v_{r''}+jv_{\theta''})v_{r''}e^{j\theta''}r''d\theta''\right]\Big|_{R_1}^{R_2}$$

$$-2\Omega e^{j\Omega t}\int_0^{2\pi}\int_{R_1}^{R_2}(jv_{r''}-v_{\theta''})e^{j\theta''}r''dr''d\theta''$$

$$+\omega^2\varepsilon\pi(R_2^2-R_1^2)e^{j\omega t}\quad,\qquad(A.7)$$

for constant rotational velocity and whirl. Here it was also assumed that the blade passage width, b, is constant and that the blade thickness is negligible. The terms have been written in complex notation to

facilitate in the transformation of coordinate systems.

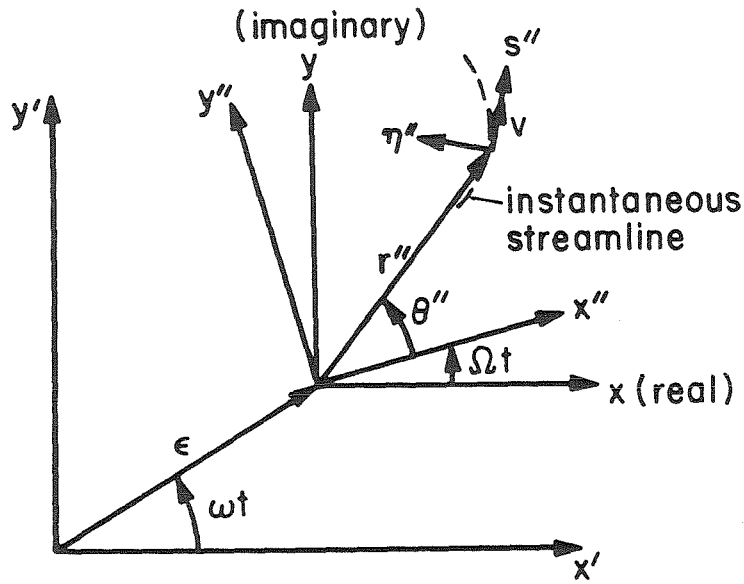

x′y′ - Volute frame
x y - Impeller frame
x″y″ - Axis fixed to impeller

Figure A.1 Description of the coordinate systems used in the derivation of Bernoulli's equation.

APPENDIX B

DERIVATION OF THE GOVERNING EQUATIONS FOR FLOW IN THE VOLUTE

The ultimate goal of this appendix is to develop an expression which relates the pressure distribution in the volute to the geometry and the inlet flow conditions of the volute. Shown in Figure B.1 are the coordinate systems to be used in this derivation. The r', θ', axis is fixed at the center of the volute and the r, θ axis is fixed at the center of the orbiting impeller, as shown. The velocity in the z' direction (normal to the page) and its derivatives will be considered negligible in the derivation of the basic equations.

The moment of momentum equation for a differential element of width, w, may be written as,

$$\rho r' V_\theta, V_\theta, w\Delta r' \Big|_{\theta' - \Delta\theta'/2}^{\theta' + \Delta\theta'/2} + \rho V_\theta, V_r, wr'\Delta\theta' \Big|_{r' - \Delta r'/2}^{r' + \Delta r'/2} + \rho r' V_\theta, V_r, w\Delta r'\Delta\theta'$$

$$+ \rho w r' r' \frac{\partial V_{\theta'}}{\partial t} \Delta r'\Delta\theta' = P_v w r'\Delta r' \Big|_{\theta' + \Delta\theta'/2}^{\theta' - \Delta\theta'/2} + P_v r'\Delta w\Delta r' \quad ,$$

so that in differential form the equation becomes,

$$\frac{\partial (r' w V_\theta, V_\theta,)}{\partial \theta'} + \frac{\partial (r' r' w V_\theta, V_r,)}{\partial r'} + r' w V_\theta, V_r,$$

$$+ r' r' w \frac{\partial V_{\theta'}}{\partial t} = - \frac{w r'}{\rho} \frac{\partial P_v}{\partial \theta'} \quad . \tag{B.1}$$

For the flow in the volute, it will be assumed that the radial velocity is small in comparison to the angular velocity so that the Coriolis term, $r'V_{\theta},V_{r'}$, can be neglected. With this observation the moment of momentum equation becomes,

$$\frac{\partial(wr'V_{\theta},V_{\theta'})}{\partial\theta'} + \frac{\partial(wr'r'V_{\theta},V_{r'})}{\partial r'} + wr'r'\frac{\partial V_{\theta'}}{\partial t} = -\frac{wr'}{\rho}\frac{\partial P_v}{\partial\theta'} \quad . \tag{B.2}$$

Similiarly the continuity equation is given by,

$$\frac{\partial(wV_{\theta},)}{\partial\theta'} + \frac{\partial(wr'V_{r},)}{\partial r'} = 0 \quad , \tag{B.3}$$

and if the radial gradient of V_{r}, is also neglected, then the equation of motion in the radial direction becomes,

$$\frac{\partial P_v}{\partial r'} = \frac{\rho V_{\theta},V_{\theta'}}{r'} \quad . \tag{B.4}$$

With the assumption that V_{θ}, varies only with θ' and t, Equation B.4 may be integrated to give the radial pressure distribution as,

$$P_v(r',\theta') = P_v(R_2',\theta') + \rho V_{\theta}^2,(\theta')\ln(r'/R_2') \quad . \tag{B.5}$$

In order to get equations that are functions of θ' alone, the moment of momentum and continuity equations will be integrated across volute sections of constant θ'. For the continuity equation this gives,

$$\int_{R_2'}^{R_3'} \frac{\partial(wV_{\theta},)}{\partial\theta'}\,dr' + \int_{R_2'}^{R_3'} \frac{\partial(wr'V_{r},)}{\partial r'}\,dr' = 0 \quad .$$

implying that,

$$\frac{\partial[V_\theta, \int_{R_2}^{R_3'} w dr']}{\partial\theta'} - wV_\theta, \Big|_{R_3'} \frac{dR_3'}{d\theta'} + wV_\theta, \Big|_{R_2'} \frac{\partial R_2'}{\partial\theta'} + wV_r, \Big|_{R_3'} R_3' - wV_r, \Big|_{R_2'} R_2' = 0 \quad .$$

But from kinematic constraints at the outer edge of the volute it is known that,

$$V_r,(R_3',\theta') = V_\theta,(R_3',\theta') \frac{dR_3'}{R_3' d\theta'} \quad . \tag{B.6}$$

Therefore, the continuity equation may finally be written as,

$$\frac{\partial[V_\theta, \int_{R_2}^{R_3'} w dr']}{\partial\theta'} = w\Big|_{R_2'} (V_r,\Big|_{R_2'} R_2' - V_\theta,\Big|_{R_2'} \frac{\partial R_2'}{\partial\theta'}) \quad . \tag{B.7}$$

Likewise, integrating the moment of momentum equation across the volute cross-section gives,

$$\frac{\partial[V_\theta^2, \int_{R_2}^{R_3'} wr' dr']}{\partial\theta'} - wV_\theta^2,\Big|_{R_3'} R_3' \frac{dR_3'}{d\theta'} + wV_\theta^2,\Big|_{R_2'} R_2' \frac{\partial R_2'}{\partial\theta'} + wV_\theta, V_r,\Big|_{R_3'} R_3' R_3'$$

$$- wV_\theta, V_r,\Big|_{R_2'} R_2' R_2' + \frac{\partial(V_\theta, \int_{R_2}^{R_3'} wr'r'dr')}{\partial t} + wV_\theta,\Big|_{R_2'} R_2' R_2' \frac{\partial R_2'}{\partial t}$$

$$= -\frac{1}{\rho} \int_{R_2}^{R_3'} wr' \frac{\partial P_v}{\partial\theta'} dr \quad . \tag{B.8}$$

This may be simplified further by again implementing the kinematic constraint at R_3' and also using the radial pressure distribution found

in Equation B.5 . Doing so yields,

$$\frac{\partial\left(V_{\theta}^{2}, \int_{R_2}^{R_3'} wr'dr'\right]}{\partial\theta'} + wV_{\theta}^{2}, \Big|_{R_2'}^{R_2'} \frac{\partial R_2'}{\partial\theta'} - wV_{\theta}, V_r, \Big|_{R_2}^{R_2'R_2'}$$

$$+ \frac{\partial\left(V_{\theta}, \int_{R_2}^{R_3'} wr'r'dr'\right)}{\partial t} + wV_{\theta}, \Big|_{R_2'}^{R_2'R_2'} \frac{\partial R_2'}{\partial t}$$

$$= -\frac{1}{\rho}\frac{\partial P_v(R_2', \theta')}{\partial\theta'} \int_{R_2}^{R_3'} wr'dr' - \frac{\partial V_{\theta'}^{2}}{\partial\theta'} \int_{R_2}^{R_3'} wr'\ln(r'/R_2')dr'$$

$$+ V_{\theta}^{2}, \frac{1}{R_2'}\frac{\partial R_2'}{\partial\theta'} \int_{R_2}^{R_3'} wr'dr' \quad . \qquad \text{(B.9)}$$

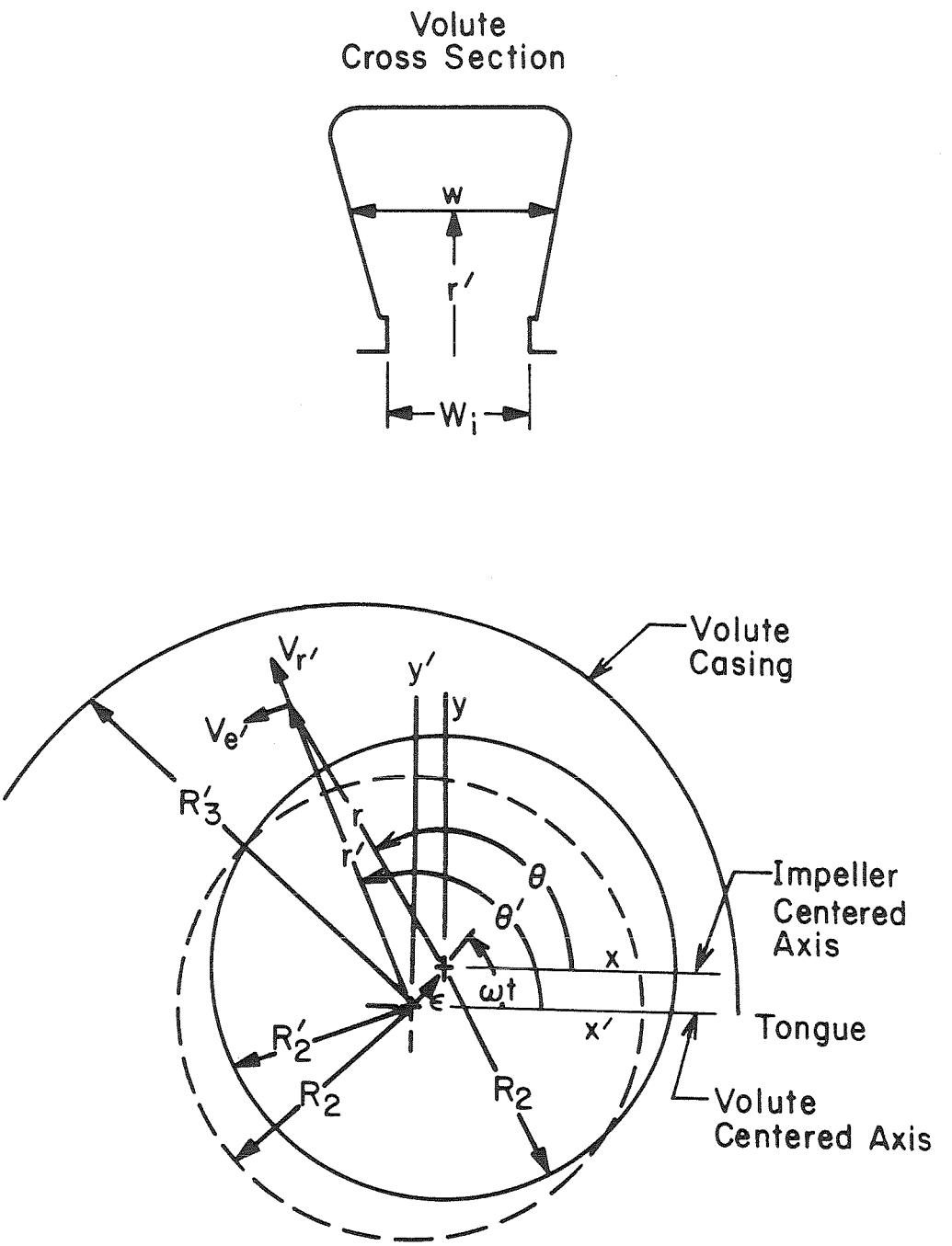

Figure B.1 Geometry used in the volute model.

APPENDIX C

SOLVING THE EQUATIONS OF THE THEORETICAL MODEL

C.1 Obtaining a Numerical Solution

All of the basic equations for a unique solution have been developed, but finding the solution might present some conceptual problems. Solving the equations will consist of finding the impeller flow perturbation, β, and the volute pressure and velocity distributions which will satisfy Equations 2.19, 2.30, and 2.32 while meeting the conditions imposed by Equations 2.36, 2.37, 2.41 and 2.43. The equations for the steady centered impeller are independent of those for the whirling impeller and must be solved first to establish the $\bar{\beta}$, $\overline{D_p}$, and $\bar{V}$ distributions, and the flow path angle, γ. Once these components are known, the distributions resulting from the eccentrically whirling impeller can be found. If the impeller is simply in an off center position but not whirling, the cos ωt and the sin ωt equations are independent of each other and may be solved separately. When the impeller is whirling, however, the in-phase and quadrature equations become coupled and must be solved simultaneously.

To numerically solve the nine total differential Equations of 2.19, 2.30, and 2.32, they were written in finite difference form using centered differencing. The integrals of Equations 2.36 and 2.44 were also calculated numerically, using Simpson's rule. All of the flow quantities of β, D_p, and V were solved for in an iterative manner, and what follows is a brief description of the procedure used in finding these distributions.

Steady Centered Impeller :

(a) Assume $\bar{\beta}(\theta) = 1$ and choose $\overline{D_p}(2\pi) - \overline{D_p}(0)$.

(b) Choose γ.

(c) Calculate $\bar{V}(0)$ with Equation 2.41a and $\bar{V}(\theta')$ from Equation 2.30a .

(d) Calculate $\overline{D_p}(\theta')$ with Equation 2.32a using a value of $\overline{D_p}(0)$ which satisfies condition 2.44a .

(e) See if $\overline{D_p}(2\pi) - \overline{D_p}(0)$ matches the initial estimate. If it does, go to (f), and if not, go to (c) with a new $\overline{D_p}(2\pi) - \overline{D_p}(0)$ estimate.

(f) Using $\overline{D_p}(\theta')$, calculate new $\beta(\theta)$ from Equation 2.19a and march far enough in θ so that $\bar{\beta}(0) = \bar{\beta}(2\pi)$ as required by 2.37 .

(g) Compare new $\bar{\beta}(\theta)$ with previous estimate and go to (i) if it matches. If it does not match go to (h).

(h) Update the guess on $\bar{\beta}(\theta)$ using the new $\bar{\beta}(\theta)$ and the condition imposed by Equation 2.36a .

(i) See if $\bar{\psi} = \psi_{exp}$ as required by condition 2.43a . If it does then go to (j). If it does not then choose a new γ and go to (b).

(j) This completes the solution of the centered impeller problem and gives the $\bar{\beta}, \bar{V}$ and $\overline{D_p}$ distributions as well as the flow path angle, γ.

With the steady distributions established, the calculations for the in-phase and quadrature components can commence. The procedure used is almost identical to that outlined above, except that γ is assumed as fixed by the steady flow calculations and the flow rate perturbations, q_c

and q_s, are unknown. The solution for the whirling impeller components is as follows.

Eccentric Whirling Impeller :

(a) Assume $\beta_c(\theta) = 0$ and $\beta_s(0) = 0$, and choose $D_{pc}(2\pi) - D_{pc}(0)$ and $D_{ps}(2\pi) - D_{ps}(0)$.

(b) Choose q_c and q_s.

(c) Calculate $V_c(0)$ and $V_s(0)$ using Equations 2.41b and c, and find $V_c(\theta')$ and $V_s(\theta')$ from Equations 2.30a and b .

(d) Calculate $D_{pc}(\theta')$ and $D_{ps}(\theta')$ with Equations 2.32b and c using a value of $D_{pc}(0)$ and $D_{ps}(0)$ which satisfies conditions 2.44b and c .

(e) See if $D_{pc}(2\pi) - D_{pc}(0)$ and $D_{ps}(2\pi) - D_{ps}(0)$ match the initial estimates. If they do, go to (f), and if they do not, go to (c) with new estimates of $D_{pc}(2\pi) - D_{pc}(0)$ and $D_{ps}(2\pi) - D_{ps}(0)$

(f) Using $D_{pc}(\theta')$ and $D_{ps}(\theta')$ calculate new $\beta_c(\theta)$ and $\beta_s(\theta)$ distributions using Equations 2.19b and c and marching far enough in θ so that $\beta_c(2\pi) = \beta_c(0)$ and $\beta_s(2\pi) = \beta_s(0)$ as required by Equation 2.37.

(g) Compare the new $\beta_c(\theta)$ and $\beta_s(\theta)$ distributions with the previous estimates and go to (i) if they are the same. If they do not match go to (h)

(h) Update the guess on $\beta_c(\theta)$ and $\beta_s(\theta)$ using the new $\beta_c(\theta)$ and $\beta_s(\theta)$ distributions and the conditions imposed by Equations 2.36 b and c.

(i) Calculate ψ_c and ψ_s using Equations 2.43b and c and see what size of flow rate perturbations, q_c and q_s in the piping attached to the pump, would correspond to these total head perturbations. If the new estimates of q_c and q_s match the previous estimates then go to (j). If they do not match, then go to (b) with an updated guess at the flow rate perturbations.

(j) This completes the solution of the whirling impeller problem and gives the in-phase and quadrature components of the β, V and D_p distributions.

C.2 Program for the Theoretical Solution

```
10 '   WHIRL2.BAS                                    Revised 01-13-86
20 DIM TH(200),B(3,200),P(3,200),V(3,200),AR(200),A(200),AP(1,20)
30 DIM LA(200),RLA(200),ARR(200),BO(200),BO2(200)
40 DIM C0(15),C1(15),C2(15),DBR(7),DBI(7)
50 DIM F0X(1),F0Y(1),FCX(1),FCY(1),FSX(1),FSY(1)
60 DIM CM(200),SM(200),ST(200),CT(200),CLM(200),SLM(200),CTL(200),STL(200)
70 PI2=6.283185
80 INPUT "Volute A or C ";VN$
90 INPUT "How many integration divisions are wanted";ND
100 W=PI2/ND : '   W=Integration step size
110 '   Initialize angles
120 FOR I=0 TO ND : TH(I)=W*I : NEXT I : '   TH(i)=Angle from tongue
130 '
140 N$="SFX"+VN$+".DAT" : '  Volute cross-sectional area  (Equa. 2.23a)
150 GOSUB 2320 : '   Read and interpolate the volute geometry
160 FOR I=0 TO ND+1 : A(I)=AR(I) : NEXT I
170 N$="SFXLM"+VN$+".DAT" : '   Log moment of volute  (Equa. 2.23b)
180 GOSUB 2320 : '   Read and interpolate the volute geometry
190 FOR I=0 TO ND+1 : LA(I)=AR(I) : NEXT I
200 N$="SFXRL"+VN$+".DAT" : '   Radial log moment of volute (Equa. 2.23e)
210 GOSUB 2320 : '   Read and interpolate the volute geometry
220 FOR I=0 TO ND+1 : RLA(I)=AR(I) : NEXT I
230 N$="SFXRR"+VN$+".DAT" : '   Radial moment squared of volute  (Equa. 2.23d)
240 GOSUB 2320 : '   Read and interpolate the volute geometry
250 FOR I=0 TO ND+1 : ARR(I)=AR(I) : NEXT I
260 N$="SFXM"+VN$+".DAT" : '  Moment of volute area  (Equa. 2.23c)
270 GOSUB 2320 : '   Read and interpolate the volute geometry
280 '
290 WB=1.452 : '  WB is the impeller width divided by blade passage width
300 INPUT "What is the outer to inner radius ratio";RR
310 LR=LOG(RR) : '   RR is the outlet to inlet radius ratio
320 DPXL=.3 : CPXL=1 : SPXL=-1 : '  Lower estimates on DELTA P(0)
330 PL=.5 : CPL=-2 : SPL=0 : '      Lower estimates on P(0)  (mean & epsilon)
340 GOSUB 2610 : ' Initialize beta distributions (BETA=1 for mean =0 for rest)
350 '
360 INPUT "What is the flow coefficient";FC
370 INPUT "What is the flow path angle, GAM";GAM
380 INPUT "What is the range & increment of speed ratio";WOW,WOWU,WOWI
390 PRINT "              RUNNING.....
400 GOTO 420
410 INPUT "WHAT IS A NEW INITIAL ESTIMATE OF DELTA P";DPXL
420 GOSUB 2500 : '   Calculate SEC(GAM)^2, TAN(GAM), & SIN & COS Arrays
430 '
440 '  ************** STEADY MEAN TERM ********************
450 EP%=0 : '   Centered Impeller Solution
460 '.....................................................
470 COUNT3%=0 : '   Begin the iteration for BETA, guessing initial distribution
480 '.....................................................
490 COUNT2%=0 : ' COUNT2 gives the number of DELTA P(0) iterations
500 DPX=DPXL : GOTO 530
```

```
510 DPYL=DPY : DPX=DPX+.01 : GOTO 530
520 DPX=((DPXL-DPXU)*DPYL+(DPYU-DPYL)*DPXL)/(DPXL-DPXU+DPYU-DPYL)
530 GOSUB 2650 : '   Find V(0) given DELTA P(0)
540 GOSUB 2760 : '   Find the velocity distribution given V(0).
550 '.....................................................
560 COUNT%=0 : '   COUNT gives number of P(0) iterations for a given DELTA P(0)
570 PU=PL+.2 : P(EP%,0)=PU : GOSUB 2820 : ' Find Pressure Distribution
580 IU=INH : P(EP%,0)=PL : GOSUB 2820 : ' Find Pressure Distribution
590 IL=INH
600 IF IU=IL GOTO 690
610 PM=PL-IL*(PU-PL)/(IU-IL)
620 P(EP%,0)=PM : GOSUB 2820 : ' Find Pressure Distribution
630 COUNT%=COUNT%+1
640 '.....................................................
650 IF COUNT%=2 GOTO 690 ELSE IF INH=0 GOTO 690
660 IF INH)0 GOTO 680
670 PL=PM : IL=INH : GOTO 600
680 PU=PM : IU=INH : GOTO 600
690 PL=PLM-.1 : COUNT2%=COUNT2%+1
700 '.....................................................
710 DPY=P(EP%,ND)-P(EP%,0)
720 IF COUNT2%=1 GOTO 510
730 IF COUNT2%)2 GOTO 750
740 DPXU=DPX : DPYU=DPY : GOTO 520
750 IF COUNT2%=5 GOTO 790 ELSE IF ABS(DPX-DPY)(.00005 GOTO 790
760 IF DPX(DPY GOTO 780
770 DPXU=DPX : DPYU=DPY : GOTO 520
780 DPXL=DPX : DPYL=DPY : GOTO 520
790 FOR I=0 TO ND : BO(I)=B(EP%,I) : NEXT I
800 GOSUB 2990 : '   Calculate BETA and its integral.
810 COUNT3%=COUNT3%+1
820 '.....................................................
830 VAR=0 : FOR I=0 TO ND : VAR=VAR+(BO(I)-B(0,I))^2 : NEXT I
840 FOR I=0 TO ND : B(0,I)=B(0,I)/INB : ' Give BETA a mean of one
850 NEXT I : '                              (as per Equation 2.36a)
860 IF COUNT3%=8 GOTO 910
870 DPXL=DPX
880 IF VAR(.00006 GOTO 920
890 FOR I=0 TO ND : B(0,I)=(3*B(0,I)+BO(I))/4 : NEXT I : ' New guess for BETA
900 GOTO 490
910 LPRINT "Non-convergent in 7 iterations, VAR =";VAR
920 KW%=0 : LPRINT "VARIANCE = ";SQR(VAR/ND) : LPRINT
930 '
940 KW%=KW%+1 : ' * START FREQUENCY RATIO CALCULATIONS **********************
950 '   ****************** COS & SIN EPSILON TERMS ********************
960 ' EP%=2 for Order of cos epsilon term,  EP%=3  sin epsilon term
970 '.....................................................
980 COUNT3%=0 : '   Begin iteration for BETA, guessing initial distribution
990 '.....................................................
1000 COUNT2%=0 : ' COUNT2 gives the number of DELTA P(0) iterations
1010 CPX=CPXL : SPX=SPXL : GOTO 1050
1020 CPYL=CPY : CPX=CPX+.1 : SPYL=SPY : SPX=SPX+.1 : GOTO 1050
1030 CPX=((CPXL-CPXU)*CPYL+(CPYU-CPYL)*CPXL)/(CPXL-CPXU+CPYU-CPYL)
```

```
1040 SPX=((SPXL-SPXU)*SPYL+(SPYU-SPYL)*SPXL)/(SPXL-SPXU+SPYU-SPYL)
1050 GOSUB 3150 : '   Find V(0) given DELTA P(0).
1060 GOSUB 3230 : '   Find the velocity distribution given V(0).
1070 '.....................................................
1080 COUNT%=0 : '   COUNT gives number of P(0) iterations for  DELTA P(0)
1090 CPU=CPL+.2 : SPU=SPL+.2 : '   Upper approximation on P(0)
1100 P(2,0)=CPU : P(3,0)=SPU : GOSUB 3350 : ' Find Pressure Distribution
1110 IUC=INHC : P(2,0)=CPL : IUS=INHS : P(3,0)=SPL : GOSUB 3350 : ' Find Press
1120 ILC=INHC : ILS=INHS
1130 IF IUC=ILC THEN PSTEPC=0 ELSE PSTEPC=-ILC*(CPU-CPL)/(IUC-ILC)
1140 IF IUS=ILS THEN PSTEPS=0 ELSE PSTEPS=-ILS*(SPU-SPL)/(IUS-ILS)
1150 CPM=CPL+PSTEPC : SPM=SPL+PSTEPS
1160 P(2,0)=CPM : P(3,0)=SPM : GOSUB 3350 : ' Find Pressure Distribution
1170 COUNT%=COUNT%+1
1180 '.....................................................
1190 IF COUNT%=2 GOTO 1270 ELSE IF INHC<>0 GOTO 1210
1200 IF INHS=0 GOTO 1270
1210 IF INHC>0 GOTO 1230
1220 CPL=CPM : ILC=INHC : GOTO 1240
1230 CPU=CPM : IUC=INHC
1240 IF INHS>0 GOTO 1260
1250 SPL=SPM : ILS=INHS : GOTO 1130
1260 SPU=SPM : IUS=INHS : GOTO 1130
1270 SPL=SPM-.1 : CPL=CPM-.1 : COUNT2%=COUNT2%+1
1280 '.....................................................
1290 CPY=P(2,ND)-P(2,0) : SPY=P(3,ND)-P(3,0)
1300 IF COUNT2%=1 GOTO 1020
1310 IF COUNT2%>2 GOTO 1330
1320 CPXU=CPX : SPXU=SPX : CPYU=CPY : SPYU=SPY : GOTO 1030
1330 IF COUNT2%=5 GOTO 1440 ELSE IF ABS(CPX-CPY)>.00005 GOTO 1360
1340 IF ABS(SPX-SPY)<.00005 GOTO 1440
1350 IF CPX=CPY GOTO 1400
1360 IF CPX<CPY GOTO 1380
1370 CPXU=CPX : CPYU=CPY : GOTO 1390
1380 CPXL=CPX : CPYL=CPY
1390 CPX=((CPXL-CPXU)*CPYL+(CPYU-CPYL)*CPXL)/(CPXL-CPXU+CPYU-CPYL)
1400 IF SPX=SPY GOTO 1050
1410 IF SPX<SPY GOTO 1430
1420 SPXU=SPX : SPYU=SPY : GOTO 1040
1430 SPXL=SPX : SPYL=SPY : GOTO 1040
1440 FOR I=0 TO ND : B0(I)=B(2,I) : B02(I)=B(3,I) : NEXT I
1450 GOSUB 3680 : '   Find SIN & COS of EPSILON BETA distribution
1460 COUNT3%=COUNT3%+1
1470 '.....................................................
1480 IF COUNT3%=7 GOTO 1630
1490 VARC=0 : FOR I=0 TO ND : VARC=VARC+(B0(I)-B(2,I))^2 : NEXT I
1500 VARS=0 : FOR I=0 TO ND : VARS=VARS+(B02(I)-B(3,I))^2 : NEXT I
1510 LPRINT "Iteration ";COUNT3%-1;"  Var COS =";SQR(VARC/ND);
1520 LPRINT " Var SIN =";SQR(VARS/ND)
1530 LPRINT "      INBC =";INBC;"  INBS =";INBS
1540 '              Satisfy Equations 2.36b & c with qc=0 and qs=0
1550 FOR I=0 TO ND : B(2,I)=(B(2,I)+1)/(INBC+1)-1 : ' Give BETAC a 0 mean
1560 B(3,I)=(B(3,I)+1)/(INBS+1)-1 : '                 Give BETAS a 0 mean
```

```
1570 B(2,I)=(3*B(2,I)+B0(I))/4 : '                    New guess at BETAC
1580 B(3,I)=(3*B(3,I)+B02(I))/4 : NEXT I : '          New guess at BETAS
1590 SPXL=SPX : CPXL=CPX
1600 IF VARC).00007 GOTO 1000
1610 IF VARS).00007 GOTO 1000
1620 GOTO 1650
1630 LPRINT "Non-convergent variance in 6 iterations ";SQR(VARC/ND),SQR(VARS/ND)
1640 '
1650 '  ***************   FORCE CALCULATIONS   ************************
1660 LPRINT
1670 '   Find hydrodynamic forces  acting on a whirling impeller.
1680 GOSUB 3960 : '   Calculate of BETA harmonics
1690 J%=0 : GOSUB 4250 : '   Calculate constants used in TOTAL FORCE
1700 GOTO 1720
1710 J%=1 : GOSUB 4330 : '   Calculate constants used in MOMENTUM FORCE
1720 '  Perform FORCE component  calculations  (see Equations 2.46 and 2.50)
1730 F0X(J%)=T1R*BBR-T1I*BBI-T2*BI : F0Y(J%)=T1R*BBI+T1I*BBR+T2*BR
1740 FCKX=2*(T1R*BCBR-T1I*BCBI)-T2*BCI : FCKY=2*(T1R*BCBI+T1I*BCBR)+T2*BCR
1750 FCCX=-(T3R*BSR-T3I*BSI)+T5R*BKSR+T6 : FCCY=-(T3R*BSI+T3I*BSR)+T5R*BKSI+T7
1760 FCCX=FCCX+T8R*BKCR-T8I*BKCI : FCCY=FCCY+T8R*BKCI+T8I*BKCR
1770 FCMX=T4R : FCMY=T4I
1780 FSKX=2*(T1R*BSBR-T1I*BSBI)-T2*BSI : FSKY=2*(T1R*BSBI+T1I*BSBR)+T2*BSR
1790 FSCX=T3R*BCR-T3I*BCI-T5R*BKCR-T7 : FSCY=T3R*BCI+T3I*BCR-T5R*BKCI+T6
1800 FSCX=FSCX+T8R*BKSR-T8I*BKSI : FSCY=FSCY+T8R*BKSI+T8I*BKSR
1810 FSMX=-T4I : FSMY=T4R
1820 FCX(J%)=FCKX+WOW*FCCX-WOW^2*FCMX : FSX(J%)=FSKX+WOW*FSCX-WOW^2*FSMX
1830 FCY(J%)=FCKY+WOW*FCCY-WOW^2*FCMY : FSY(J%)=FSKY+WOW*FSCY-WOW^2*FSMY
1840 '
1850 IF J%=1 GOTO 2010
1860 '   Print out the results.
1870 LPRINT "WHIRL2.BAS                        Revised 01-13-86
1880 FL$="Flow Coefficient = " : SR$="Speed Ratio, w/W = "
1890 GM$="Flow Path Angle = "
1900 LPRINT USING"&  #.###";FL$,FC
1910 LPRINT USING"&  ##.##";GM$,GAM
1920 LPRINT USING"&  #.###";SR$,WOW
1930 LPRINT
1940 LPRINT "   Writing the force on the impeller as,"
1950 LPRINT
1960 LPRINT "    ( Fx )   ( Fox )     [ Fxx     Fxy ] ( cos(wt))
1970 LPRINT "    (    ) = (     ) +e* [             ] (        )
1980 LPRINT "    ( Fy )   ( Foy )     [ Fyx     Fyy ] ( sin(wt))
1990 LPRINT : LPRINT "Total Force Components" : LPRINT
2000 GOTO 2020
2010 LPRINT : LPRINT "Momentum Force Components" : LPRINT
2020 F0$=" ( Fx )   (" : F1$=")     [" : F3$="] ( cos(wt))
2030 LPRINT USING " & +#.### & ";F0$,F0X(J%),F1$;
2040 LPRINT USING "+#.###  +#.### & ";FCX(J%),FSX(J%),F3$
2050 LPRINT "  (    ) = (        ) +e* [                ] (        )"
2060 F0$=" ( Fy )   (" : F1$=")     [" : F3$="] ( sin(wt))
2070 LPRINT USING " & +#.### & ";F0$,F0Y(J%),F1$;
2080 LPRINT USING "+#.###  +#.### & ";FCY(J%),FSY(J%),F3$
2090 LPRINT : LPRINT
```

```
2100 IF J%=0 GOTO 1710
2110 LPRINT "
2120 LPRINT " THETA     D̄p        Dpc       Dps       B̄         Bc        Bs"
2130 FOR I=0 TO ND STEP 10 : LPRINT USING "  ###";TH(I)*360/PI2;
2140 LPRINT USING "   +#.####";P(0,I);P(2,I);P(3,I);B(0,I);B(2,I);B(3,I)
2150 NEXT I
2160 LPRINT : LPRINT
2170 A123=1+2*(LA(ND)-LA(0))/(A(ND)-A(0)) : THR0=(P(0,ND)+A123*V(0,ND)^2)/2
2180 THR1=P(2,ND)/2+A123*V(0,ND)*V(2,ND)-V(0,ND)^2
2190 THR2=P(3,ND)/2+A123*V(0,ND)*V(3,ND)
2200 LPRINT " total head rise mean, cos, sin = ";
2210 LPRINT USING "    +#.#####";THR0;THR1;THR2
2220 LPRINT : LPRINT
2230 '          Check on condition required by Equation 2.43a
2240 INPUT "Is the Theoretical Total Head = Experimental (Y or N)";AREPLY$
2250 IF AREPLY$="N" GOTO 360
2260 WOW=WOW+WOWI
2270 IF ABS(WOW)<ABS(WOWU+.0001) GOTO 940
2280 GOTO 360
2290 END
2300 '
2310 '-------------------------------------------------------------
2320 '        Subroutine to READ and INTERPOLATE the VOLUTE GEOMETRY
2330 OPEN "I",#1,N$
2340 INPUT#1,K
2350 FOR I=1 TO K : INPUT#1,AP(0,I),AP(1,I) : NEXT I : ' Measured Results
2360 FOR I=1 TO K-1 : INPUT#1,C2(I),C1(I),C0(I) : NEXT I : ' Spline Fit Results
2370 CLOSE #1
2380 '
2390 '  Number of divisions = ND, Width = W, TH(i) = cross-section location,
2400 '  & AR(i) = cross-sectional area. (TH(0) = tongue location)
2410 J=1 : AR(0)=AP(1,1) : AR(ND)=AP(1,K-1) : AR(ND+1)=AP(1,K)
2420 FOR I=1 TO ND-1
2430 THD=TH(I)*360/PI2
2440 IF THD>AP(0,J+1) THEN J=J+1
2450 AR(I)=(C2(J)*THD+C1(J))*THD+C0(J)
2460 NEXT I
2470 FOR I=0 TO ND STEP 20 : PRINT TH(I)*360/PI2,AR(I) : NEXT I
2480 RETURN
2490 '-------------------------------------------------------------
2500 '        Subroutine to CALCULATE SEC(GAM)^2 & TAN(GAM) & SIN(th) & COS(th)
2510 SG2=1/(COS(GAM*PI2/360))^2 : TG=TAN(GAM*PI2/360) : TGLR=TG*LR
2520 CTGLR=COS(TGLR) : STGLR=SIN(TGLR) : CT(ND)=1 : ST(ND)=0
2530 CTL(ND)=CTGLR : STL(ND)=STGLR
2540 FOR I%=0 TO ND-1 : THM=(TH(I%+1)+TH(I%))/2
2550 CT(I%)=COS(TH(I%)) : ST(I%)=SIN(TH(I%)) : CM(I%)=COS(THM)
2560 SM(I%)=SIN(THM) : CLM(I%)=COS(THM+TGLR) : SLM(I%)=SIN(THM+TGLR)
2570 CTL(I%)=COS(TH(I%)+TGLR) : STL(I%)=SIN(TH(I%)+TGLR)
2580 NEXT I%
2590 RETURN
```

```
2600 '-------------------------------------------------------------
2610 '        Subroutine to GIVE FIRST GUESS OF BETA DISTRIBUTION
2620 FOR I=0 TO ND : B(0,I)=1 : B(1,I)=0 : B(2,I)=0 : B(3,I)=0 : NEXT I
2630 RETURN
2640 '-------------------------------------------------------------
2650 '        Subroutine to CALCULATE V(0)   (Equa. 2.41a)
2660 '          this is the closure condition at the tongue
2670 B0=FC*PI2/A(ND)
2680 B1=A(0)/A(ND)
2690 B2=1+2*LA(0)/A(0)
2700 RT=(1-B1^2)*DPX/B2+B0^2
2710 IF RT)0 GOTO 2730
2720 PRINT "Too high of a delta P." : GOTO 410
2730 V(0,0)=(B0*B1+SQR(RT))/(1-B1^2)
2740 RETURN
2750 '-------------------------------------------------------------
2760 '        Subroutine to CALCULATE THE VELOCITY DISTRIBUTION  (Equa 2.30a)
2770 FOR I=0 TO ND-1
2780 V(EP%,I+1)=(V(EP%,I)*A(I)+W*FC*(B(EP%,I+1)+B(EP%,I))/2)/A(I+1)
2790 NEXT I
2800 RETURN
2810 '-------------------------------------------------------------
2820 '        Subroutine PRESSURE AND CLOSURE CONDITION  (Equa. 2.32a)
2830 FOR I=0 TO ND-1
2840 VM=V(0,I)+V(0,I+1) : BM=B(0,I)+B(0,I+1) : AM=A(I)+A(I+1)
2850 ARM=AR(I)+AR(I+1) :  RLAM=RLA(I)+RLA(I+1)
2860 P(0,I+1)=2*(ARM+RLAM)*(V(0,I+1)^2-V(0,I)^2)+(AR(I+1)-AR(I))*VM^2
2870 P(0,I+1)=P(0,I)-(P(0,I+1)-(2-FC*TG*BM)*FC*BM*W)/ARM
2880 NEXT I
2890 '  Impeller Problem Closure Condition   (Equa. 2.44a)
2900 INH=P(EP%,0)-P(EP%,ND) : IND=0
2910 FOR I=1 TO ND-1 STEP 2
2920 INH=INH+4*P(EP%,I)+2*P(EP%,I+1) : IND=IND+2*(2*B(EP%,I)^2+B(EP%,I+1)^2)
2930 NEXT I
2940 '   As required by the impeller problem
2950 '                                the integral of (P+FC^2*SG2*B^2)/PI2=1
2960 INH=(INH+FC*FC*SG2*IND)/(3*ND)-1
2970 RETURN
2980 '-------------------------------------------------------------
2990 '  Subroutine INTEGRATE FOR BETA   (Equa. 2.19a)
3000 D1=4*LR/(FC*W) : D2=FC*FC*SG2/2
3010 FOR J=1 TO 6
3020 FOR I=0 TO ND-1
3030 BB=(P(0,I)+P(0,I+1)-2)/D2
3040 B(0,I+1)=-D1-B(0,I)+SQR(D1*(D1+4*B(0,I))-BB)
3050 NEXT I
3060 INB=B(EP%,0)-B(EP%,ND)
3070 FOR I=1 TO ND-1 STEP 2 : INB=INB+4*B(EP%,I)+2*B(EP%,I+1) : NEXT I
3080 INB=INB/(3*ND)
3090 IF B(EP%,0)=B(EP%,ND) GOTO 3120 : '   (Condition of Equa. 2.37)
3100 B(EP%,0)=B(EP%,ND)
3110 NEXT J
3120 RETURN
```

```
3130 '   ********** EPSILON SIN & COS TERMS ***************************
3140 '-------------------------------------------------------------
3150 ' Subroutine to calculate EPSILON V(0) (COS & SIN)  (Equa. 2.41b & c)
3160 B0=(1+2*LA(0)/A(0))*2 : B1=WB/A(0)
3170 B2=V(0,0)-A(0)*V(0,ND)/A(ND)
3180 V(2,0)=WB*(V(0,ND)-V(0,0))*V(0,ND)/A(ND)
3190 V(2,0)=(V(2,0)-((V(0,ND)^2-V(0,0)^2)*(2+B1)+B1*DPX-CPX)/B0)/B2
3200 V(3,0)=SPX/B0/B2
3210 RETURN
3220 '-------------------------------------------------------------
3230 '   Subroutine to calculate EPSILON V (COS & SIN)   (Equa. 2.30b & c)
3240 FOR I=0 TO ND-1
3250 D1=ST(I+1) : D0=ST(I) : T1=CT(I+1) : T0=CT(I)
3260 V(2,I+1)=WB*(V(0,I+1)*T1-V(0,I)*T0)+FC*(B(0,I+1)*D1-B(0,I)*D0)
3270 V(2,I+1)=V(2,I+1)+W*WOW*SM(I)
3280 V(2,I+1)=(V(2,I+1)+FC*W*(B(2,I+1)+B(2,I))/2+A(I)*V(2,I))/A(I+1)
3290 V(3,I+1)=WB*(V(0,I+1)*D1-V(0,I)*D0)-FC*(B(0,I+1)*T1-B(0,I)*T0)
3300 V(3,I+1)=V(3,I+1)-W*WOW*CM(I)
3310 V(3,I+1)=(V(3,I+1)+FC*W*(B(3,I+1)+B(3,I))/2+A(I)*V(3,I))/A(I+1)
3320 NEXT I
3330 RETURN
3340 '-------------------------------------------------------------
3350 '   Subroutine to calculate EPSILON P (COS & SIN)   (Equa. 2.32b & c)
3360 FOR EP%=2 TO 3
3370 FOR I=0 TO ND-1
3380 VP2=V(0,I+1)^2 : V2=V(0,I)^2 : VM=V(0,I+1)+V(0,I) : BM=B(0,I+1)+B(0,I)
3390 VVP=V(0,I+1)*V(EP%,I+1) : VV=V(0,I)*V(EP%,I) : ARM=AR(I+1)+AR(I)
3400 IF EP%=3 GOTO 3440
3410 D1=CT(I+1) : D0=CT(I) : TM=2*SM(I)
3420 VEM=V(3,I+1)+V(3,I) : DM=2*CM(I) : S=1
3430 GOTO 3460
3440 D1=ST(I+1) : D0=ST(I) : TM=2*CM(I)
3450 VEM=V(2,I+1)+V(2,I) : DM=2*SM(I) : S=-1
3460 H1=S*W*(WOW*(WB*TM*VM-(ARR(I+1)+ARR(I))*VEM)+TM*(FC*BM)^2/2)/4
3470 H1=H1+FC*(1-FC*TG*BM)*(W*(B(EP%,I+1)+B(EP%,I))+S*TM*(B(0,I+1)-B(0,I)))/2
3480 H1=H1+FC*W*DM*(WOW+2-FC*TG*BM)*BM/4-2*(AR(I+1)*VVP- AR(I)*VV)
3490 H1=H1-(RLA(I+1)+RLA(I))*(VVP-VV)+(WB+ARM/2)*(D1*VP2-D0*V2)
3500 P(EP%,I+1)=P(EP%,I)+(4*H1+WB*DM*(P(0,I+1)-P(0,I)))/ARM
3510 NEXT I
3520 NEXT EP%
3530 '   Impeller Problem Closure Condition   (Equa. 2.44b & c)
3540 INHC=P(2,0)-P(2,ND)+P(0,0)-P(0,ND) : INDC=0 : INHS=P(3,0)-P(3,ND) : INDS=0
3550 INWC=0 : INWS=0
3560 FOR I=1 TO ND-1 STEP 2
3570 INHC=INHC+4*(P(2,I)+P(0,I)*COS(TH(I)))+2*(P(2,I+1)+P(0,I+1)*COS(TH(I+1)))
3580 INHS=INHS+4*(P(3,I)+P(0,I)*SIN(TH(I)))+2*(P(3,I+1)+P(0,I+1)*SIN(TH(I+1)))
3590 INDC=INDC+4*B(2,I)*B(0,I)+2*B(2,I+1)*B(0,I+1)
3600 INDS=INDS+4*B(3,I)*B(0,I)+2*B(3,I+1)*B(0,I+1)
3610 INWC=INWC+4*B(0,I)*CTL(I)+2*B(0,I+1)*CTL(I+1)
3620 INWS=INWS+4*B(0,I)*STL(I)+2*B(0,I+1)*STL(I+1)
3630 NEXT I
3640 INHC=(INHC+2*FC*FC*SG2*INDC+2*WOW*FC*RR*INWS)/(3*ND)
3650 INHS=(INHS+2*FC*FC*SG2*INDS-2*WOW*FC*RR*INWC)/(3*ND)+(P(0,ND)-P(0,0))/PI2
```

```
3660 RETURN
3670 '-------------------------------------------------------------
3680 '   Subroutine to find EPSILON BETA     (Equa. 2.19b & c)
3690 C1=FC/(LR*4) : C2=WOW/2 : C3=2*(WOW/T6)^2 : C4=2*FC*SG2*LR
3700 FOR J=1 TO 6
3710 FOR I=0 TO ND-1
3720 BM=B(0,I+1)+B(0,I)
3730 F1=C3*(CM(I)-CLM(I)/RR)+WOW*(-FC*RR*SLM(I)*BM+2*CLM(I)/RR)
3740 F1=(F1-(P(2,I+1)+P(2,I))/2+SM(I)*(P(0,I+1)-P(0,I))/W)/C4
3750 F2=C3*(SM(I)-SLM(I)/RR)+WOW*(FC*RR*CLM(I)*BM+2*SLM(I)/RR)
3760 F2=(F2-(P(3,I+1)+P(3,I))/2-CM(I)*(P(0,I+1)-P(0,I))/W)/C4
3770 A1=1+C1*W*BM : B1=C2*W
3780 D1=W*(F1-C2*B(3,I)-C1*BM*B(2,I))+B(2,I)
3790 D2=W*(F2+C2*B(2,I)-C1*BM*B(3,I))+B(3,I)
3800 DEN=A1*A1+B1*B1
3810 B(2,I+1)=(A1*D1-B1*D2)/DEN
3820 B(3,I+1)=(B1*D1+A1*D2)/DEN
3830 NEXT I
3840 '   Calculate integrals of Epsilon Beta
3850 INBC=B(2,0)-B(2,ND) : INBS=B(3,0)-B(3,ND)
3860 FOR I=1 TO ND-1 STEP 2 : INBC=INBC+4*B(2,I)+2*B(2,I+1) : NEXT I
3870 FOR I=1 TO ND-1 STEP 2 : INBS=INBS+4*B(3,I)+2*B(3,I+1) : NEXT I
3880 INBC=INBC/(3*ND) : INBS=INBS/(3*ND)
3890 IF B(2,0)=B(2,ND) GOTO 3910 : '      (Condition of Equa. 2.37)
3900 B(2,0)=B(2,ND) : GOTO 3920
3910 IF B(3,0)=B(3,ND) GOTO 3940 : '      (Condition of Equa. 2.37)
3920 B(3,0)=B(3,ND)
3930 NEXT J
3940 RETURN
3950 '-------------------------------------------------------------
3960 '   Subroutine to calculate the BETA INTEGRALS (used in Equa. 2.46 & 2.50)
3970 FOR J%=0 TO 7 : DBR(J%)=0 : DBI(J%)=0 : NEXT J%
3980 FOR J%=1 TO ND-1 STEP 2
3990 C=CT(J%) : S=ST(J%)
4000 FOR K%=0 TO 3
4010 IF K%=1 GOTO 4060
4020 DBR(K%)=DBR(K%)+4*B(K%,J%)*C+2*B(K%,J%+1)*CT(J%+1)
4030 DBI(K%)=DBI(K%)+4*B(K%,J%)*S+2*B(K%,J%+1)*ST(J%+1)
4040 DBR(K%+4)=DBR(K%+4)+4*B(0,J%)*B(K%,J%)*C+2*B(0,J%+1)*B(K%,J%+1)*CT(J%+1)
4050 DBI(K%+4)=DBI(K%+4)+4*B(0,J%)*B(K%,J%)*S+2*B(0,J%+1)*B(K%,J%+1)*ST(J%+1)
4060 NEXT K%
4070 NEXT J%
4080 FOR K%=0 TO 7
4090 DBR(K%)=DBR(K%)/(3*ND) : DBI(K%)=DBI(K%)/(3*ND)
4100 NEXT K%
4110 BR=DBR(0) : BI=DBI(0) : BBR=DBR(4) : BBI=DBI(4)
4120 BCR=DBR(2) : BCI=DBI(2) : BSR=DBR(3) : BSI=DBI(3)
4130 BCBR=DBR(6) : BCBI=DBI(6) : BSBR=DBR(7) : BSBI=DBI(7)
4140 BKCR=0 : BKCI=0 : BKSR=0 : BKSI=0
4150 FOR J%=1 TO ND-1 STEP 2
4160 BKCR=BKCR+4*B(0,J%)*CTL(J%)*CT(J%)+2*B(0,J%+1)*CTL(J%+1)*CT(J%+1)
4170 BKCI=BKCI+4*B(0,J%)*CTL(J%)*ST(J%)+2*B(0,J%+1)*CTL(J%+1)*ST(J%+1)
4180 BKSR=BKSR+4*B(0,J%)*STL(J%)*CT(J%)+2*B(0,J%+1)*STL(J%+1)*CT(J%+1)
```

```
4190 BKSI=BKSI+4*B(0,J%)*STL(J%)*ST(J%)+2*B(0,J%+1)*STL(J%+1)*ST(J%+1)
4200 NEXT J%
4210 BKCR=BKCR/(3*ND) : BKCI=BKCI/(3*ND)
4220 BKSR=BKSR/(3*ND) : BKSI=BKSI/(3*ND)
4230 RETURN
4240 ' ---------------------------------------------------------------
4250 '   Subroutine to calculate TOTAL FORCE CONSTANTS  (see Equa. 2.50)
4260 T1R=FC*FC*(WB*SG2-2+RR*CTGLR)
4270 T1I=FC*FC*(2*TG+RR*STGLR) : T2=-2*FC*(WB*SG2*LR+1)
4280 T3R=2*FC*(1-WB*SG2*LR-CTGLR/RR) : T3I=-2*FC*STGLR/RR
4290 T4R=-1+1/RR^2+WB*(1-CTGLR/RR)/TG^2 : T4I=WB*STGLR/(RR*TG^2)
4300 T5R=2*FC*WB*RR : T6=-WB*CTGLR/RR : T7=-2*FC+WB*STGLR/RR : T8R=0 : T8I=0
4310 RETURN
4320 ' ---------------------------------------------------------------
4330 '   Subroutine to calculate MOMENTUM FORCE CONSTANTS (see Equa. 2.46)
4340 T1R=FC*FC*(-1+RR*CTGLR)
4350 T1I=FC*FC*(TG+RR*STGLR) : T2=-2*FC
4360 T3R=2*FC*(1-CTGLR/RR) : T3I=-2*FC*STGLR/RR
4370 T4R=-1+1/RR^2 : T4I=0 : T5R=0 : T6=0 : T7=0
4380 T8R=2*FC*STGLR : T8I=-2*FC*CTGLR
4390 RETURN
```

APPENDIX D

DOCUMENTATION ON FACILITY MODIFICATIONS

	Tap Location *			
No.	Front	Tap Dia.(in.)	Back	Tap Dia.(in.)
1	5:30	1/16	0:00	1/32
2	11:15	1/16	3:30	1/32
3	22:30	1/16	13:00	1/32
4	33:45	1/16	22:30	1/32
5	56:15	1/16	45:00	1/32
6	78:45	1/16	68:30	1/32
7	101:15	1/16	90:00	1/32
8	123:45	1/16	112:30	1/32
9	146:15	1/16	135:00	1/32
10	168:45	1/16	157:30	1/32
11	191:15	1/16	180:00	1/32
12	213:45	1/16	202:30	1/32
13	236:15	1/16	225:00	1/32
14	258:45	1/16	247:30	1/32
15	281:15	1/16	270:00	1/32
16	303:45	1/16	292:30	1/32
17	326:45	1/16	315:00	1/32
18	337:30	1/16	337:30	1/32
19	348:45	1/16	348:45	1/32
20	352:00	1/16	354:30	1/32
21	358:30	1/16		
22	180:00	1/32		

* All locations are measured relative to the tongue in the direction of increasing volute cross-sectional area. Units are degress:minutes.

TABLE D.1 LOCATION OF THE PRESSURE TAPS IN VOLUTE A (see Figure 4.4)

	Tap Location*			
No.	Front	Tap Dia.(in.)	Back	Tap Dia.(in.)
1	5:00	1/16	0:00	1/16
2	15:00	1/16	10:00	1/16
3	30:00	1/16	20:00	1/16
4	50:00	1/16	40:00	1/16
5	70:00	1/16	60:00	1/16
6	90:00	1/16	80:00	1/16
7	110:00	1/16	100:00	1/16
8	130:00	1/16	120:00	1/16
9	150:00	1/16	140:00	1/16
10	170:00	1/16	160:00	1/16
11	190:00	1/16	180:00	1/16
12	220:00	1/16	200:00	1/16
13	230:00	1/16	220:00	1/16
14	250:00	1/16	240:00	1/16
15	270:00	1/16	260:00	1/16
16	290:00	1/16	280:00	1/16
17	310:00	1/16	300:00	1/16
18	330:00	1/16	320:00	1/16
19	345:00	1/16	340:00	1/16
20	355:00	1/16	350:00	1/16

* All locations are measured relative to the tongue in the direction of increasing volute cross-sectional area. Units are degrees:minutes.

TABLE D.2 LOCATION OF THE PRESSURE TAPS IN VOLUTE C (see Figure 4.5)

	Tap Location *	
No.	Angle	Tap Dia.(in.)
1	0:00	1/16
2	18:00	1/16
3	36:00	1/16
4	54:00	1/16
5	72:00	1/16
6	90:00	1/16
7	100:30	1/16
8	118:30	1/16
9	136:30	1/16
10	154:30	1/16
11	172:30	1/16
12	220:00	1/16
13	230:00	1/16
14	250:00	1/16
15	270:00	1/16
16	290:00	1/16
17	310:00	1/16
18	330:00	1/16
19	345:00	1/16
20	355:00	1/16

* All locations are measured relative to the tongue in the direction of increasing cross-sectional area. Units are degrees:minutes.

TABLE D.3 LOCATION OF THE PRESSURE TAPS IN THE ANNULAR GAP (see Figure 4.7)